UNIVERSITA’ DEGLI STUDI DI PADOVA

DIPARTIMENTO DI FISICA E ASTRONOMIA

Corso di Laurea Magistrale in Fisica

EXPERIMENTAL VERIFICATION OF QUANTUM-OPTICAL ANALOGIES BY RECONFIGURABLE WAVEGUIDE STRUCTURES in SBN and Fe:LN

Relatore: Dott. Marco Bazzan
Correlatore: Prof. Germano Montemezzani

Laureanda: Vittadello Laura

Anno Accademico 2013/2014

ACKNOWLEDGEMENTS

This work was realized in collaboration with the LMOPS laboratory (Metz, France), so first of all I thank Jean Paul Salvestrini to have received me in the laboratory.

A special thanks to Germano Montemezzani, to have supervised my work during the permanence in LMOPS laboratory and to have motivated me to let me shine. It was pleasant to work with you.

I thank also Massimo Alonzo, the scientific discussions and your advices have been precious for the success of this work.

The other special thanks is for my director, Marco Bazzan, for the opportunity you have given to me by including me in this project. I found this subject very stimulating and fascinating.

I would have also to thank all the graduate students and non with whom I have enjoyed my time in Metz and who have given a contributions for the success of this work. You made me feel welcome in all the situations.

The last but the most important thanks is to my family which have always encouraged me and supported my choices, even if they have brought me away from home.

INDEX

INTRODUCTION 1

1| THEORY 5

- 1.1 Summary of Quantum Dynamical Coupled State Phenomena 5
  - 1.1.2 Three-State STIRAP, EIT 5
  - 1.1.2 Two-State STIRAP 11
  - 1.1.4 Disorder-Enhanced Transport in Photonic Quasicrystals 15
- 1.2. Coupled Optical Waveguides 16
  - 1.2.1 Optical waveguides 16
  - 1.2.2 Coupled mode theory 19
  - 1.2.3 Resonant case 21
  - 1.2.4 Detuned case 24
  - 1.1.2 Diffusion trough aperiodic coupled waveguides array 25

2| RECONFIGURABLE WAVEGUIDES 27

- 2.1 The Pockels Effect 27
- 2.2 Photorefractive Effect 29
- 2.3 Dynamical Optical structures inStrontium Barium Niobate 30
  - 2.3.1 SBN 31
  - 2.3.2 Sample 32
  - 2.3.3 Waveguide Creation by lateral illumination technique 33
  - 2.3.4 Experimental Setup 35
- 2.4 Photorefractive Direct writing Iron doped Lithium Niobate 37
  - 2.4.1 Fe:LN 37
  - 2.4.3 Waveguide creation 41
  - 2.4.4 Experimental setup 44

3| OPTICAL TWO-STATE STIRAP IN SBN 47

- 3.1 Setup Optimization and Characterization 47
- 3.2 Theoretical Modeling 49
- 3.3 Results and Discussion 51

4 DIRECT WRITING OF FIBONACCI WAVEGUIDES ARRAY IN Ti:Fe:LN 57
  4.1 Waveguide characterization 57
  4.2 Gratings characterization 63
    4.2.1 Description of the setup 63
    4.2.2 Periodic and Fibonacci diffraction gratings 65
CONCLUSIONS 75
ANNEX A 79
BIBLIOGRAPHY 87

INTRODUCTION

Similarities between wave optics and quantum mechanics have been highlighted in many occasions and they can be dated back to the early developments of quantum physics. The analogy between geometric optics and Newtonian particle dynamics was in fact the guiding line to the born of quantum mechanics after the famous publishing of de Broglie in 1923. From the initial development of the quantum mechanics a wide variety of concepts were borrowed from the optic and successfully applied to this new theory in order to demonstrate the wavy behavior of particles such as electrons. In particular the first concepts applied to the quantum dynamic were the ones of interference and diffraction, well known for light waves.

Transfer of ideas and concepts between these two branches of knowledge continuously occurred untill nowadays and in the past decade, experimental and theoretical studies on quantum-optical analogies have seen an important resurgence. It has proven that coupled optically waveguides provide a rich laboratory to investigate the classical analogues of a wide variety of coherent quantum effect encountered in atomic, molecular, or condensed matter physics.

The access of coherent wave phenomena in microscopic quantum systems is often a challenging task because of complications arising from many-body effects, decoherence and the presence of time-dependent or non linear terms in the Schrödinger equation. In this context the study of the wave phenomena in optics has several advantages: (1) the possibility of a direct and easy spatial visualization of typical ultrafast phenomena in time; (2) the possibility to explore coherent dynamical regimes not yet accessible in quantum system; (3) the ability to mimic coherent laser-matter interactions by simple geometric bending of the guiding photonic structures. Due to these advantages the optic permits not only to demonstrate the quantum effects but to go further tanks to the more easy implementation, insomuch as quantum effects can inspire the conception of new optical components [9].

In this work only two types of quantum effects are optically taken into account: the two-state STImulated Raman Adiabatic Passage (STIRAP) belonging to the atomic and molecular physics and the diffusion enhanced in quasicrystal belonging to the solid-state physics. The first one is a quantum phenomenon that permits to achieve an equal coherent superposition of two quantum states. If initially the population is entirely confined in the state of lower energy, at the end of the process an equal distribution of the atoms in the two states is achieved. For the second phenomena recent experiments have highlighted as in quasicrystals the introducing of disorder cannot transform the material in an insulator, as happens for the other materials following the phenomena of Anderson localization. This effect is only briefly described because the aim of this second part is the developing of the setup permitting further future studies of the quantum effect.

Their optical description is developed in the framework of purely classic electromagnetically theory and the experiments are conducted in a regime where the field quantization is not needed.

To optically study these quantum effects it is important to utse techniques permitting a good control on the design and on the physical properties of the structure, as the curvature of the waveguide or the index contrast. The conventional techniques exploiting physical-chemical processes allows to satisfied these requirements but they need a technology not easy to implement and in addition fixed optical structures are create. On the other hand, to test optically the proposed phenomena, a versatile and low – cost approach is needed because a great number of experimental tests will be required before finding the optimum configuration, so that using conventional techniques a great number of sample would be necessary. The same problem arises for the implementation of the setup to the study of transport properties in quasicrystal so it was decided to use two alternative techniques, reconfigurable, based on the photoinscription: the lateral illumination technique and the photo induced direct writing technique.

The first one consists on an illumination of a photorefractive crystal (strontium barium niobate) submitted to an external electric field, with a laser containing the desired waveguides pattern which has to be reproduced in the crystal. The reconfiguration time is in order of minutes, allowing to make a great number of experimental tests even if the sample cannot be moved from the setup, because when the illumination is light-off the structure degraded. Consequently the characterization of the structures must be made in the same setup used for their creation and this technique appeared to be optimal to demonstrate optically the two-state STIRAP, for which a great number of tests are required but not the displacement of the sample.

The second one consists of a scanning with a laser beam on the surface of photorefractive crystal (lithium niobate) in order to create permanent optical structures. The reconfigurable times are in order of hours, but now the sample can be moved from the setup: this is an essential condition for the type of characterizations that has to be made for the study of quasicrystals.

This work is based on a collaboration project between Université de Lorraine (Metz) and Università degli studi di Padova. In particular the study and the optical verification of the two-state STIRAP was made in the foreign university and it is framed in a contest in which the optical effect can be exploited to create new optical components. The optical demonstration of the generalized three-state STIRAP, a quantum phenomena similar to the present one, was in fact the basis to produce a planar achromatic multiple beam splitter. In particular the two-state STIRAP can be the basis phenomena to produce a perfect achromatic 50:50 beam coupler.

The basis study on the system able to reproduce optically the quasicrystals was made in Padova and this work aspires to create a setup with which to study the properties of these materials not yet well understood.

In the initial part of the *first chapter* the quantum theory of the of three-state STIRAP and EIT is discussed, being the basis to understand the two-state STIRAP. Later the two-state STIRAP in its quantum version and the theory of quasicrystals are introduced. In the second part of the chapter the coupling mode theory is explained and the basic principles of the analogies are described. Finally the correspondence between the quantum and optic variables is explained for each quantum phenomena.

The *second chapter* deals with the phorefractive and Pockels effect, the basic phenomena used to create optical structures. The properties of strontium barium niobate and lithium niobate are also described, as functional for the discussion of the two techniques used to create optical structures: the lateral illumination technique and the photoinduced direct writing technique. Their physical principle and advantages are explained and later the correspondingly setup is presented.

The *third chapter* deals with the presentation of the optical demonstration of the two-state STIRAP in strontium barium niobate. The central part of this section is the explanation of the programs written in Matlab languages, used to make both the simulations and the experimentally configurations of the quantum phenomena. They are basis on the resolution of the coupling mode theory and starting from the initial theoretical condition they created a image of the waveguides ready to be tested.

In the *fourth chapter* the analyzes of waveguides and Fibonacci gratings, simulation the quasicrystal behavior, are presented. This structures are made in lithium niobate and characterized respectively in near and far field: this study is the basis to a further develop of the optical system able to reproduce optically the quasicrystals.

1 | THEORY

1.1 Summary of Quantum Dynamical Coupled State Phenomena

There are many types of phenomena that can be discussed in relationship with the analogies between quantum physics and optics. Following the classification proposed by Longhi [1] it is possible to distinguish three principal categories: analogies of optics with fundamental concepts and effects of quantum mechanics, with solid-state physics and with atomic and molecular physics. In this work only the last two categories are discussed, and in particular the first one in relation to the phenomena of the diffusion thought aperiodic quasicrystals, while the second one to the two-state STIRAP.

1.1.2 Three-State STIRAP, EIT

It is important to introduce two effects which will be used in this work: the three-state STImulated Raman Adiabatic Passage (STIRAP) and Electromagnetically Induced Transparency (EIT).

The basis notion to understand the formalism describing this two mechanisms is the one of Rabi oscillation. The excited population P(t) of a two state-system exposed to steady coherent radiation does not follow a monotonically increasing pattern but oscillates sinusoidally. This mechanism is known as *Rabi oscillations* and in particular when the radiation is resonant, i.e. the laser frequency is equal to the Bohr transition, the result is:

$$P(t) = \frac{1}{2}[1 - \cos(\Omega t)] \tag{1.1}$$

where the frequency Ω is known as *Rabi frequency* and it is associated to the strength of the atom-radiation interaction and proportional to the square root of the laser intensity. When the radiation intensity varies the Rabi frequency consequently varies and the cosine argument Ωt is replacing by the so-called *pulse area* A(t), the time integral of the Rabi frequency.

$$\Omega t \rightarrow \int_{-\infty}^{t} \Omega(t')dt' = A(t)$$

so the excited-state population oscillates between 0 and 1.

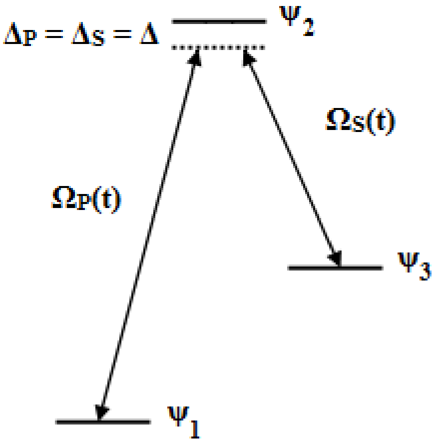

Figure 1.1 : Quantum system with three energy levels in lambda configuration utilized for the STIRAP technique.

The oscillatory Rabi cycling characteristic of the two-state system can also be found in a multistate systems. In the particular case of a three-state system, as the one of Figure 1.1, the transition probabilities P_{12} from the state ψ_1 to the state ψ_2 and P_{23} from the state ψ_2 to state ψ_3 are:

$$P_{12} = \frac{1}{2}(1 - \cos A_{12}) \qquad P_{23} = \frac{1}{2}(1 - \cos A_{23}) \tag{1.2}$$

The three-state STIRAP (STImulated Adiabatic RAman Passage) is a process that, permits to achieve adiabatically a complete population transfer from an initially populated state ψ_1 to a metastable state ψ_3, via an intermediate state ψ_2, named two-photon Raman transition.

The quantum system used to describe this phenomenon is lambda-type, as shown in Figure 1.1, in which the intermediary state is coupled to ψ_1 by a field named *pump field*, and to ψ_3 by the *Stokes field*. In particular the population is transferred by two lasers characterized by two Rabi frequencies named respectively $\Omega_P(t)$ and $\Omega_S(t)$, indicating respectively the pump and Stokes pulse. $\Delta_P = \omega_{1\text{-}2} - \omega_p$ and $\Delta_S = \omega_{2\text{-}3} - \omega_S$ are the respectively the single photon frequency detuning, i.e. the difference between the frequency of the Bohr transition $\omega_{1\text{-}2}$ ($\omega_{2\text{-}3}$) and that one carried by the laser beam ω_p (ω_s).

Mathematically the system is described by the time-dependent Schrödinger equation

$$i\hbar \frac{d}{dt}\mathbf{\Psi}(t) = H(t)\mathbf{\Psi}(t) \tag{1.3}$$

where $\Psi(t)$ is the wave function characterizing the system evolution and defined as:

$$\mathbf{\Psi}(t) = \sum_{n=1}^{N} C_n(t)\psi_n(t). \tag{1.4}$$

$C_n(t)$ is the probability amplitude whose absolute square is the probability $P_n(t)$ that the atom will be found in state $\psi_n(t)$ at the instant t and defined as:

$$P_n(t) = |C_n(t)|^2 = |\langle\psi_n|\mathbf{\Psi}(t)\rangle|^2. \tag{1.5}$$

Using (1.5) the Schrödinger equation (1.3) results as a coupled set of ordinary differential equations assuming the form:

$$i\hbar\frac{d}{dt}\boldsymbol{C}(t) = H(t)\boldsymbol{C}(t) \tag{1.6}$$

where C(t) = $[C_1(t), C_2(t), C_3(t)]$ is a three component column vector of the population probability amplitudes, defined in the base of ψ_1, ψ_2, ψ_3, named *diabatic* states.
The wished initial and final conditions of the equation are $C(-\infty) = [1,0,0]^T$ and $C(+\infty) = [0,0,1]^T$, that means that the entire population resides initially in ψ_1 and at the end in ψ_3.

In the rotating wave approximation (RWA) [7] the Hamiltonian has the form:

$$H(t) = \hbar\begin{pmatrix} 0 & \frac{1}{2}\Omega_\mathrm{P}(\mathrm{t}) & 0 \\ \frac{1}{2}\Omega_\mathrm{P}(\mathrm{t}) & \Delta_\mathrm{P} & \frac{1}{2}\Omega_\mathrm{S}(\mathrm{t}) \\ 0 & \frac{1}{2}\Omega_\mathrm{S}(\mathrm{t}) & \Delta_\mathrm{P}-\Delta_\mathrm{S} \end{pmatrix}. \tag{1.7}$$

In particular in this work only the two-photons resonance between ψ_1 and ψ_3 is described, i.e. the one for which $\Delta_P = \Delta_S$,. If this condition is satisfied, the eigenstates of the Hamiltonian (1.7) are the time-independent states ψ_1, ψ_2, ψ_3 and the eigenvalues, that represent the energies of the three states, are respectively

$$\varepsilon_+(t) = \frac{\Delta+\sqrt{\Delta^2+\Omega^2(t)}}{2} \tag{1.8 a}$$

$$\varepsilon_0(t) = 0 \tag{1.8 b}$$

$$\varepsilon_-(t) = \frac{\Delta-\sqrt{\Delta^2+\Omega^2(\mathrm{t})}}{2} \tag{1.8 c}$$

where $\Omega(\mathrm{t}) = \sqrt{\Omega_\mathrm{P}^2(\mathrm{t}) + \Omega_\mathrm{S}^2(\mathrm{t})}$ is the root-mean-square Rabi frequency.

In this space, in which the quantum system is normally described, the phenomenon has not a direct comprehension. Indeed it is most easily understood in another one, which coordinate vectors are the eigenstates ψ_1, ψ_2, ψ_3.
The new eigenstates, named *adiabatic states*, are related to the diabatic states by the relations

$$\Phi_+(t) = \sin\theta\sin\vartheta\ \psi_1 + \cos\vartheta\,\psi_2 + \cos\theta\sin\vartheta\ \psi_3 \tag{1.9 a}$$

$$\Phi_0(t) = \cos\theta\ \psi_1 - \ \sin\theta\ \psi_3 \tag{1.9 b}$$

$$\Phi_-(t) = \sin\theta\cos\vartheta\ \psi_1 - \sin\vartheta\ \psi_2 + \cos\theta\cos\vartheta\ \psi_3 \tag{1.9 c}$$

where the time-dependent mixing angles $\theta(t)$ and $\vartheta(t)$ are defined as

$$tg\ \theta(t) = \frac{\Omega_P(t)}{\Omega_S(t)}, \qquad tg\ 2\vartheta(t) = \frac{\Omega(t)}{\Delta}. \tag{1.10}$$

The eigenvalue $\Phi_0(t)$ associated with the null eigenvalues has a particular importance because, exploiting this state, it is possible to achieve a complete population transfer between ψ_1 and ψ_3 without populating the state ψ_2. To force the system to follow this eigenstate, named *dark state*,

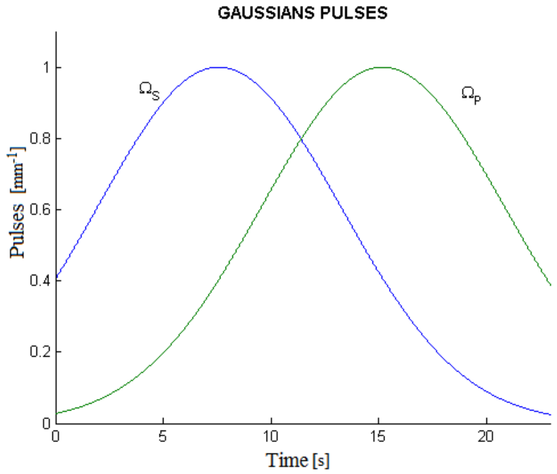

Figure 1.2 : Exemple of gaussians pulses in the conterintuitive sequence leading to the three-state STIRAP.

the key variable to control is the angle $\theta(t)$ because, changing it from 0° to 90°, the system is initially completely aligned with ψ_1 and, at the end, with ψ_3.
To achieve this, at the beginning of the process, the Rabi frequency of the Stokes pulse $\Omega_S(t)$ has to be larger than that one of the pump pulse $\Omega_P(t)$, in this way when $\frac{\Omega_P}{\Omega_S} \xrightarrow[t\to-\infty]{} 0$, from the equation. (1.9a), the angle θ gets zero. On the contrary, at the end, the amplitude of the two pulses has to be in the opposite situations, to obtain $\theta = 90°$.
This type of pulse sequence is called '*counterintuitive*', because the intuition would suggest to act at the beginning with $\Omega_P(t)$ and at the end with $\Omega_S(t)$, to move the population from ψ_1 to ψ_3.

If an *intuitive* sequence of pulses is applied, generalized Rabi oscillation in the three states are produced, and it is impossible to achieve a complete transfer of the population from ψ_1 to ψ_3.

To achieve the population transfer an important constraint has to be taken into account: the pulses have to have an appropriate form to permit an adiabatic evolution of the system.
Mathematically this condition requires that

$$\left|\langle\dot{\Phi}_+|\dot{\Phi}_-\rangle\right| \ll |\varepsilon_+ - \varepsilon_-| \qquad (1.11)$$

This condition reflects the fact that the coupling between the adiabatic states has to be negligible as compared to the difference between their energies.
By developing the equations one realizes that only pulses sufficiently smooth, close in amplitudes, with a large area and exhibiting a sufficient overlap permit to have an adiabatic evolution. In this way $\theta(t)$ change slowly and the system has the possibility to remain aligned with the dark state Φ_0 during the process.
Considering that the variation has to be slow, the exact form of the pulses is not determinant to obtain the population transfer: the Figure 1.2 shows a possible configuration, where the two pulses have been chosen to be gaussian.

Because the state ψ_2 does not participate to the population transfer, as long as the excitation remains adiabatic, its properties, such as radiative decay, do not influence the STIRAP process.

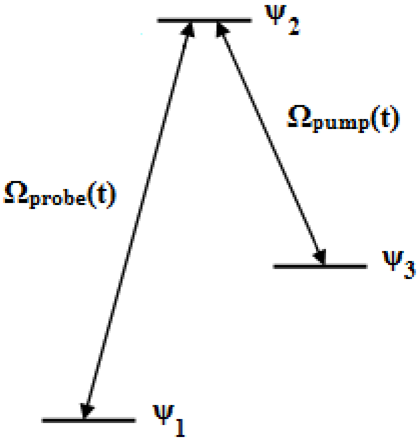

Figure 1.3: Quantum system in lambda configuration utilised to achieve the EIT effect.

The system just described can be generalized to one with N energy levels, visible in the Figure 1.3, and the corresponding phenomenon is called multiple-STIRAP [2].

The Electromagnetically Induced Transparency (EIT) is an optical non-linear coherent modification of the optical properties of a material. It can occur near an atomic resonance, when an electric field of the correct frequency is applied.

This effect has been predicted theoretically in 1990 by Harris et *al*. [3,4] and the first experimentally demonstration has been realized some years later by Boller et *al.* using strontium vapors [5] and by Field et *al.* using lead vapors [6].

The quantum system used to describe this phenomenon is, in its simplest form, a three levels system in lambda configurations, like that one shown in Figure 1.3. The laser pulse that couple the state ψ_1 and ψ_2 is named *probe pulse* whereas that one that couple ψ_2 and ψ_3 *pump pulse*.

The EIT effect can be achieved only if three conditions are respected: (1) the transitions from ψ_1 to ψ_2 and from ψ_2 to ψ_3 are permitted whereas the one from ψ_1 to ψ_3 is dipole forbidden; (2) $\Omega_{pump} >> \Omega_{probe}$ and finally (3) the two lasers pulses have to be in resonance with the dipolar transitions, that means $\Delta_{pump} = \Delta_{probe} = \Delta = 0$.

This configuration is completely equivalent to that one described for the STIRAP mechanism, therefore the Schrödinger equation that describes the time evolution of this system is identical to those previously used:

$$i\hbar \frac{d}{dt}\boldsymbol{C}(t) = H(t)\boldsymbol{C}(t) \tag{1.12}$$

where C(t) = $[C_1(t), C_1(t), C_3(t)]$ is three component column vector of the probability amplitudes, defined in the base of *diabatic* states ψ_1, ψ_2, ψ_3, while, in the RWA approximation, the Hamiltonian has the form

$$H(t) = \frac{\hbar}{2}\begin{pmatrix} 0 & \Omega_{\mathrm{probe}}(\mathrm{t}) & 0 \\ \Omega_{\mathrm{probe}}(\mathrm{t}) & 0 & \Omega_{\mathrm{pump}}(\mathrm{t}) \\ 0 & \Omega_{\mathrm{pump}}(\mathrm{t}) & 0 \end{pmatrix}. \tag{1.13}$$

different from the previous one of equation (1.7) because $\Delta_{pump} = \Delta_{probe} = \Delta = 0$.

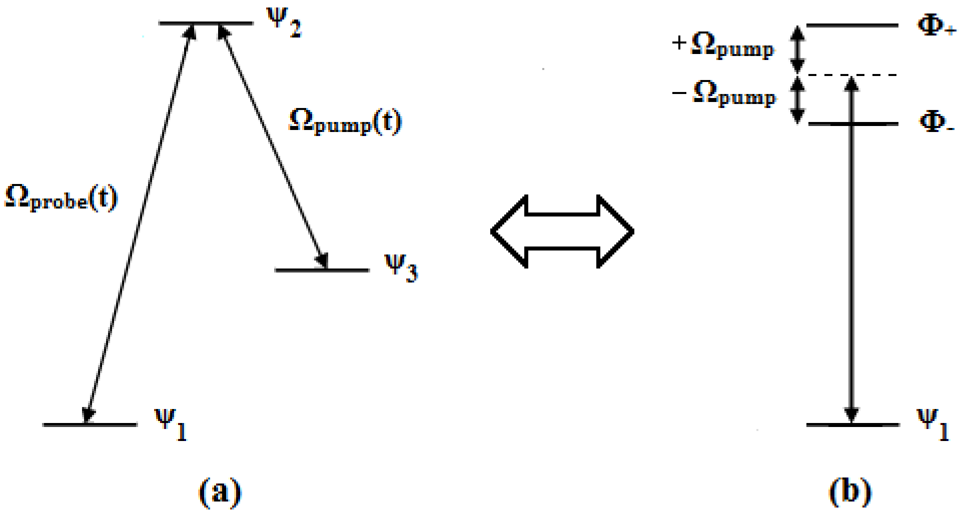

Figure 1.4: Quantum systems associated to EIT phenomenon. (a) in the base of unperturbed states ψ_1 ψ_2 ψ_3. (b) in the new base ψ_1 Φ_- Φ_+.

The EIT can be explained in two different ways: the first using the notion of the quantum interference destruction and the second one using the logic adopted to explain STIRAP mechanism and in particular the dressed states.

Let's consider that all the atoms are initially in the state of lowest energy ψ_1. When the resonant probe pulse is applied, a certain number of atoms have the probability to pass in the level ψ_2 directly ($\psi_1 \rightarrow \psi_2$). When the pump pulse is also applied the atoms have another way to reach ψ_2 following the sequence $\psi_1 \rightarrow \psi_2 \rightarrow \psi_3 \rightarrow \psi_2$. Since we consider $\Omega_{pump} >> \Omega_{probe}$, the two ways to transfer the atoms towards ψ_2 have the same probability to occur. Solving the Schrödinger equation (1.12), the solution highligths that each transition is characterized by a phase shift of the probability amplitude of $\pi/2$. Therefore the two different ways to populate the ψ_2 level have a total phase difference of π between them: the two mechanisms interfere destructively and the total probability to have the atoms in ψ_2 becomes null. In others words the transition between ψ_1 and ψ_2 is no more possible and the material becomes transparent to this transition.

The second point of view utilizes a different mathematical approach. When $\Omega_{pump} >> \Omega_{probe}$, like in the specific case of EIT, it is more convenient to express the equations in the basis where basis vectors are the instantaneous eigenstates of the Hamiltonian (1.13), like it has been done for the STIRAP mechanism. Therefore the eigenstates have the general form expressed in the Equations (1.9) but , since $\Omega_{pump} >> \Omega_{probe}$ and $\Delta = 0$,with fixed values for the angles, $\theta(t) = 0$ and $\vartheta(t) = \pi/4$. The equations (1.9) can be rewritten in the following form:

$$\Phi_+(t) = \frac{\sqrt{2}}{2}(\psi_2 + \psi_3) \qquad (1.14\text{ a})$$

$$\Phi_0(t) = 0 \qquad (1.14\text{ b})$$

$$\Phi_-(t) = \frac{\sqrt{2}}{2}(\psi_2 - \psi_3) \qquad (1.14\text{ c})$$

as can be seen, the two eigenvalues Φ_+ and Φ_- are a linear combination, symmetric and antisymmetric respectively, of the unperturbed states ψ_2 and ψ_3. So, in this new base, the strong coupling between ψ_2 and ψ_3 form a different type of system named *dressed state*, as shown in the Figure 1.4, in which Φ_+ and Φ_- are separated of $2\Omega_{pump}$.

As it can be seen in Figure 1.4, the appearance of the dressed state have as consequence that the Ω_{probe} is no longer resonant with the two photons transition, as it was permitted in the original system.
If initially the population is entirely confined in ψ_1, it is no longer possible to move it toward ψ_2 or ψ_3, and the state becomes transparent to this transition.
This consideration can be deduced also considering directly the equation (1.14b). The state Φ_0 does not have components in the states ψ_2 and ψ_3, therefore if the population is initially entirely in ψ_1, it does not move from this state during the time evolution.

1.1.2 Two-State STIRAP

The two-state STIRAP is a quantum phenomenon that permits to achieve an equal coherent superposition of two quantum states. If initially the population is entirely confined in the state of lower energy, at the end of the process an equal distribution of the atoms in the two states is achieved.

The quantum system that describes this mechanism is shown in the Figure 1.5. The two energy levels ψ_1 and ψ_2, named *diabatic* states, are coupled by a laser characterized by a Rabi frequency $\Omega(t)$, which is not in resonance with the two-photon transition. The offset between the Bohr transition frequency $\omega_0 = (E_2 - E_1)/\hbar$ and the laser carries frequency ω_L is the time dependent detuning $\Delta(t)$.
The evolution of this system is described by the time dependent Schrödinger equation as before

$$i\hbar\frac{d}{dt}C(t) = H(t)C(t) \tag{1.15}$$

where $C(t) = [C_1(t), C_1(t)]$ is a two component column vector of probability amplitude, defined in the base of diabatic states ψ_1, ψ_2 and, in the RWA approximation, the Hamiltonian has the form

$$H(t) = \frac{1}{2}\begin{bmatrix} 0 & \Omega(t) \\ \Omega(t) & 2\Delta(t) \end{bmatrix}. \tag{1.16}$$

The wished initial and final state of the system are $C(-\infty) = [1,0]^T$ and $C(+\infty) = [1,1]^T$, that means that the entire population resides initially in ψ_1 while at the end there is an equal distribution in ψ_1 and ψ_2.
The RWA approximation, used to describe the system, is valid if both the frequency $\Omega(t)$ and $\Delta(t)$ are much smaller than the laser carrier frequency ω_L.

The model presented to describe the two-state system is a useful picture of the real situation but only an idealization. Real atoms have an infinite number of bound states that become important, for example, when the spontaneous emission is included in the description of the system. Indeed when this phenomenon occurs for the exited level, there is a probability that the population lead to levels other than the ground state, so that these atoms are lost from the two-state system previously described. A correct description would have to take into account the presence of additional levels and the probability loss out of the system occurring from ψ_2.

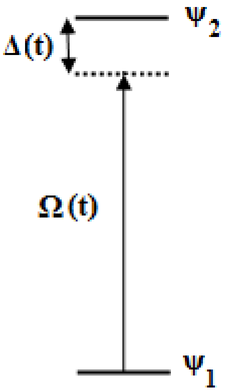

Figure 1.5: Quantum system utilised in the two-state STIRAP phenomenon.

Mathematically this traduces in the using of non-Hermitian Hamiltonian where the probability is not conserved.

As it was seen for the three-state STIRAP, it is more convenient to describe the evolution of the system in a new base, whose coordinate vectors are the instantaneous eigenstates of the Hamiltonian (1.16).
In this new space the corresponding eigenstates, named *adiabatic states*, are related to ψ_1, ψ_2 by the relations

$$\Phi_+(t) = \psi_1 \sin\theta(t) + \psi_2 \cos\theta(t) \tag{1.17 a}$$
$$\Phi_-(t) = \psi_1 \cos\theta(t) + \psi_2 \sin\theta(t) \tag{1.17 b}$$

where the mixing angle θ(t) is defined as

$$\theta(t) = \frac{1}{2} arc \tan\left[\frac{\Omega(t)}{\Delta(t)}\right]. \tag{1.18}$$

The corresponding eigenvalues, that represent the energies of the adiabatic states, are defined by the following equations

$$\varepsilon_+(t) = \frac{1}{2}\left[\Delta(t) + \sqrt{\Delta^2(t) + \Omega^2(t)}\right] \tag{1.19 a}$$
$$\varepsilon_-(t) = \frac{1}{2}\left[\Delta(t) - \sqrt{\Delta^2(t) + \Omega^2(t)}\right] \tag{1.19 b}$$

as it was seen for the EIT, in this base the two eigenvalues form a new type of system named *dressed state*.
To achieve a population transfer θ(t) has to change slowly enough so that the state evolves adiabatically, in others words the Rabi frequency Ω(t) and the detuning Δ(t) have to change slowly, so that the state vector remains fixed in the adiabatic coordinates space. As already seen, mathematically the general adiabatic condition requires that

$$\left|\langle \dot{\Phi}_+ | \dot{\Phi}_- \rangle\right| \ll |\varepsilon_+ - \varepsilon_-|. \tag{1.20}$$

The coupling between the adiabatic state has to be negligible compared to the difference between their energies. For a two-state system the equation (1.20) is converted as follow

$$\frac{1}{2}\left|\dot{\Omega}\Delta - \Omega\dot{\Delta}\right| \ll (\Omega^2 + \Delta^2)^{3/2}. \tag{1.21}$$

This relation means that the adiabatic condition requires first of all smooth pulses and furthermore a large Rabi frequency and/or large detuning.

The system presented in Fig. 1.5 can be used to achieve the STIRAP phenomenon, like described in the Paragraph 1.1.1, but using only two states. The first big difference between the three-state and the two-state STIRAP is that in the last case an equal superposition, and not a completed transfer of population, at the end of the process is obtained. To describe the way in which the phenomenon works it is useful to start showing the topological equivalence between the two-state system and the three-state system [6].

The equation (1.15) can be transformed as three coupled Bloch equations having real-valued variables, using complex values of the probability amplitude, so that in the RWA approximations the transformed Schrödinger equation takes the form [12]:

$$i\frac{d}{dt}\begin{bmatrix} u(t) \\ v(t) \\ w(t) \end{bmatrix} = \begin{bmatrix} 0 & -\Delta(t) & 0 \\ \Delta(t) & 0 & -\Omega(t) \\ 0 & \Omega(t) & 0 \end{bmatrix}\begin{bmatrix} u(t) \\ v(t) \\ w(t) \end{bmatrix}. \tag{1.22}$$

The quantities *u,v,w* are the real-valued time-dependent coordinates of the Bloch vector that moves in an abstract three dimensional space. In particular *u* and *v* are respectively the real and the imaginary part of the *coherence* expressed by the term $2C_1C_2^*$ that is:

$$coherence = u + iv = 2C_1C_2^* \tag{1.23}$$

and *w* is the population inversion. The initial condition is *w*(-∞) = -1

The equations (1.22) are therefore the conversion of the two-level into a three-level system. It should be noted that this is not a time-dependent Schrödinger evolution for a resonantly coupled lambda-system in the usual RWA approximation. The latter would have the following form:

$$i\frac{d}{dt}\begin{bmatrix} C_1(t) \\ C_2(t) \\ C_3(t) \end{bmatrix} = \frac{1}{2}\begin{bmatrix} 0 & \Omega_P(\mathrm{t}) & 0 \\ \Omega_P(\mathrm{t}) & 0 & \Omega_S(\mathrm{t}) \\ 0 & \Omega_S(\mathrm{t}) & 0 \end{bmatrix}\begin{bmatrix} C_1(t) \\ C_2(t) \\ C_3(t) \end{bmatrix} \tag{1.24}$$

where Ω_p(t) and Ω_S(t) are respectively the pump and the Stokes pulses, as already described for the three-state STIRAP.

In order to make the equation (1.24) similar to (1.22) so that the two systems mathematically equivalently, it is sufficient to replace the probability amplitude C_1, C_2, C_3 as follow

$$\tilde{C}_2 = -iC_2 \tag{1.24 a}$$
$$\tilde{C}_3 = -C_3 \tag{1.25 b}$$

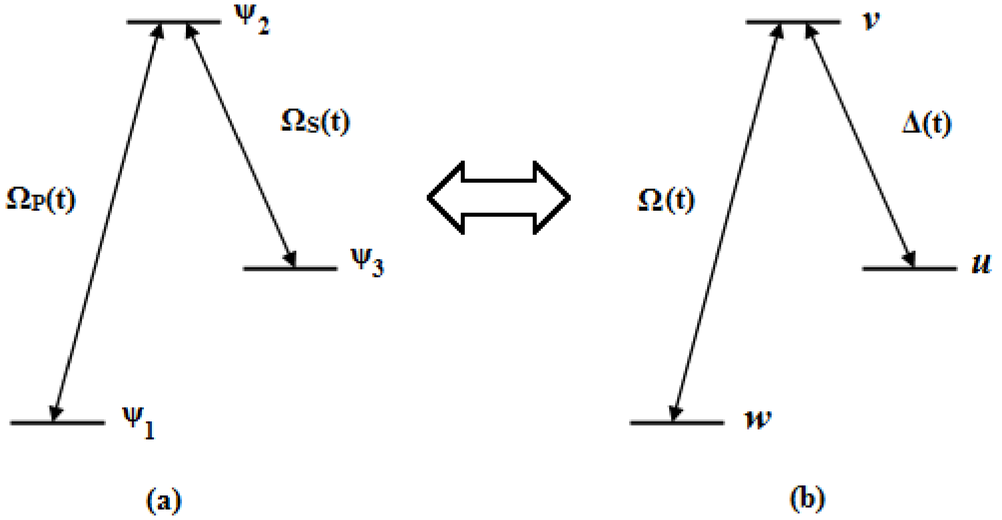

Figure 1.6: (a) Quantum system used to achieve the three-state STIRAP in the base of unperturbed states ψ_1 ψ_2 ψ_3. (b) Two-state system express like a three-state configuration, used to descibe the two-state STIRAP phenomenon.

and to permute C_1 and $\tilde{C}_3$ to obtain the right structure of the desired Schrödinger equation:

$$i\frac{d}{dt}\begin{bmatrix}\tilde{C}_3(t)\\ \tilde{C}_2(t)\\ C_1(t)\end{bmatrix}=\frac{1}{2}\begin{bmatrix}0 & -\Omega_S(t) & 0\\ \Omega_S(t) & 0 & -\Omega_P(t)\\ 0 & \Omega_P(t) & 0\end{bmatrix}\begin{bmatrix}\tilde{C}_3(t)\\ \tilde{C}_2(t)\\ C_1(t)\end{bmatrix}. \tag{1.26}$$

Comparing equation (1.22) with (1.26) it is clear that vector components *u*,*v*,*w* are the analogous of $\tilde{C}_3, \tilde{C}_2, \tilde{C}_1$ respectively. The detuning Δ(t) and the Rabi frequency Ω(t) in (1.22) have the role of the Rabi frequency $\Omega_S(t)$ and $\Omega_P(t)$ in the counterintuitive three-state STIRAP, as shown in Figure 1.6.

This type of formalism is very useful because now, to study the two-state STIRAP, it is possible to use the same mathematical approach already explained for the three-state STIRAP.
The equation (1.22) has three eigenvalues, one of which null. As already seen, the corresponding eigenstate is the only one that permit to achieve an adiabatic transfer of the population from the initial state *w* to *u*, because it is the only one that presents a linear combination of only two states .

$$d(t) = w(t)\cos\theta(t) + u(t)\sin\theta(t) \tag{1.27}$$

where θ(t) as the following form:

$$tg\ \theta(t) = \frac{\Omega(t)}{\Delta(t)}. \tag{1.28}$$

To have the passage of the population from *w* to *u*, initially the detuning Δ(t) has to be larger than Ω(t), so that asymptotically θ(-∞) = 0, hence d(-∞) = *w*(-∞). At the end the opposite situation has to be fulfilled, therefore θ(+∞) = π/2 and d(+∞) = *u*(+∞).

The last condition means that the system achieves a state characterised by the condition $|u|=1$ and $v=w=0$. Knowing that states having $u^2+v^2=1$ and $w=0$ are *states of maximal coherence* in a two-level system, the process that depletes completely the initial energy level in the three-state configurations corresponds to create a maximally coherent superposition of the states in the two-level configuration. Using the same notation already explained for the three-state STIRAP this sequence of pulses is named counterintuitive.

On the contrary, by implementing an intuitive sequence of pulses, the initial state is completely depleted but an oscillating superposition of ψ_2 and ψ_3 is created. In the two-state STIRAP this fact has as consequence that a state characterised by the conditions $w = 0$ and $|u^2|+|v^2|=1$ is created. Also in this case a state of maximal coherence is achieved and it is possible to have in the two levels, at the end of the process, an equal distribution of the initial population.

To maintain the system in the adiabatic condition it is necessary to change slowly the pulses. The other important condition is that the pulses have a large area, as prescribed by the global condition of adiabaticity, already discussed for the three-state STIRAP,

$$\frac{\pi}{2} \ll \int_{+\infty}^{-\infty} \tilde{\Omega}(t)dt \tag{1.29}$$

where $\tilde{\Omega}(t) = \sqrt{\Omega^2(t) + \Delta^2(t)}$.

The adiabatic passage is very robust and depends weakly on the overlap of the two pulses.

Besides, the most energetically efficient choice consists in implementing two pulses with the same maximal amplitude.

1.1.4 Disorder-Enhanced Transport in Photonic Quasicrystals

Usual theory of charge transport in conducting crystals rely on the concept of Bloch Waves, where the quantum state of the charge carriers is described by a Schrödinger equation with a periodic potential. This kind of formalism exploits the perfect periodicity of the crystal medium to find explicit solutions to this problem and lead to well known concepts in solid state physics, such as energy band, effective masses and so on. A fundamental change in this situation occurs when the perfect periodicity of the medium is perturbed. The so-called Anderson localization is a phenomenon in which, introducing disorder, a conducting crystal can transform in an insulator. A more intriguing situation observed in partially ordered media, such as *quasicrystals*.

A quasicrystal is defined as an intermediate phase between an ordered and a disordered structure. It does not have a unit cell and does not exhibit translational symmetries as usually interpreted for a periodic structure, but anyway it possesses a long range order and displays Bragg diffraction [40]. They were discovered by Shechtmann et al.[42] in 1984 and the first theoretical analysis was proposed in the same year by Levine and Steinhardt [43]. These structures are classified using the notion of order, originating from the corresponding periodic structure of a dimension higher than the physical one. For example a 1D quasicrystal it can be seen as the projection of a 2D periodic lattice on a line [42], so in the theoretical model the Bragg diffraction is attributed to the presence of higher dimension.

First experiments in the study of transport properties of these crystals have highlighted that the presence of a disordered structure enhance the transport instead of turning it off .

More deepened experiments have concluded that quasicrystals have counterintuitive transport properties; in this respect, some fundamental questions are still not answered. For example, the mechanism proposed to explain the unusual transport in quasicrystals assumes non-interacting electrons while the conductivity measurements inevitably incorporate electro-electron interactions. . A possible way to investigate experimentally these issues is to mimic the dynamic of electron waves with optical signals and the quasi – periodic atomic potential with suitable waveguiding structures.

In this scenario, it is mandatory to develop some kind of optical system which could be used to reproduce optically these kinds of phenomena in a convenient fashion. This is one of the goals of the present work.

1.2. Coupled Optical Waveguides

The theory of quantum-optical analogies is based on the observation that the fundamental equation describing quantum phenomena, the Schrödinger equation, has the same structure of the one describing the waveguides coupling in optic. Thanks to this analogy coupled optically waveguides provide a laboratory to investigate the classical analogues of coherent quantum effect just described. This approach has several advantages: (1) the possibility of a direct and easy visualization in space of typical ultrafast phenomena in time; (2) the possibility to explore coherent dynamical regimes not yet accessible in quantum system; (3) the ability to mimic coherent laser-matter interactions by simple geometric bending of the guiding

1.2.1 Optical waveguides

A waveguide is an element able to confine an electromagnetic wave and, in particular of optical type if the frequency of the transported wave is in the optic range. They are built using at the least two different dielectrics and the confinement is achieved surrounding the material with the larger refractive index, i.e. the core, with the others ones, i.e. the cladding. The light can be confined in one or more directions but only the first type, named planar, and characterized by only two index refractions, is mathematically studied in this paragraph.

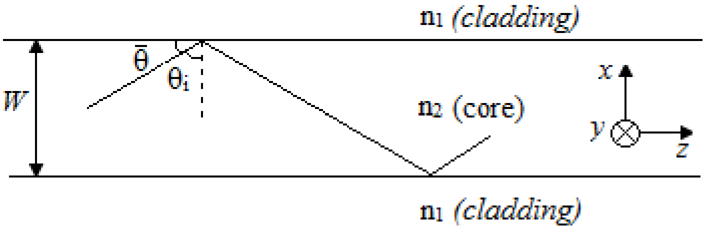

Figure 1.7: Description of a single palanar waveguide of width W, an indice refraction n_2 in the core and n_1 in the cladding. θ_i is the incident angle at the surface separation core-cladding, $\bar{\boldsymbol{\theta}}$ is its complementary angle. The guide is invariant upon y tranlations.

From the point of view of the geometrical optical, it is known that a single waveguide confines the incident light when two conditions are satisfied. The first imposes that the incident angle at the core-cladding surface separation is larger than the critical angle of total internal reflection, so that the optical ray is completely reflected, as shown in Figure 1.7. The second

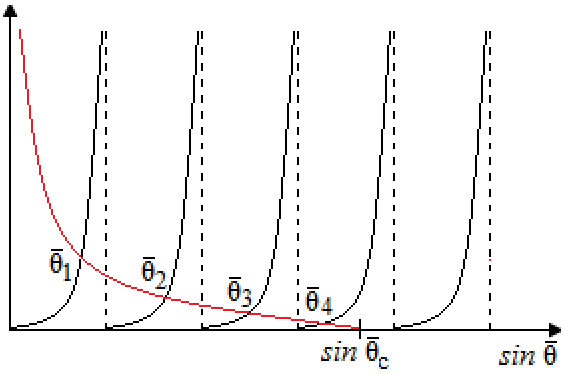

Figure 1.8: Graphic solution of trascendental equation. The red curve is the rigth side of the equation, whereas the black one is the left side. The intersection of two curve permits to find θ_m, and their number indicates how many modes can propagate in the guide.

imposes that the wave satisfies the condition of auto-coherence, so that after two total reflections at the interface core-cladding the resultant wave has to be equal to the incident one. This condition is mathematically translated into the equation:

$$2k_0 W n_2 \sin\bar{\theta} - 2\varphi = 2\pi m \tag{1.30}$$

where $k_0=2\pi/\lambda$ is the module of the wave vector in the vacuum, *W* is the waveguide width, φ is the variation of the phase caused by the total reflection and *m* is the order of the mode propagation. The variation of the phase is calculated using the Fresnel equations and for transvers electric (TE) modes, the only realized in our experiments of light induced waveguides, it has the form:

$$\tan\frac{\varphi}{2} = \sqrt{\frac{\sin^2\bar{\theta}_c}{\sin^2\bar{\theta}} - 1} \tag{1.31}$$

The presence of the parameter *m* in the equation (1.30) implies a discretisation of $\bar{\theta}$, where each value corresponds to a different guided mode. As consequence, also the longitudinal constant of propagation β(z) becomes discretized in function of the mode *m* considered:

$$\beta_m = k_0 n_2 \cos\bar{\theta}_m = k_0 n_{eff_m} \tag{1.32}$$

where $n_{eff\ m}$ is the refractive effective index seen along the propagation by the specific mode *m* and which satisfies the condition $n_2 < n_{eff\ m} < n_1$.

By substituting equation (1.31) in (1.30) the latter can be rewritten as follows:

$$\tan\left(\frac{\pi W n_2}{\lambda_0}\sin\bar{\theta} - \frac{m\pi}{2}\right) = \sqrt{\frac{\sin^2\bar{\theta}_c}{\sin^2\bar{\theta}} - 1} \tag{1.33}$$

This is the *transcendental equation* and it permits to calculate the different values of $\bar{\theta}_m$. As it is not resolvable analytically, it is possible to resolve it only numerically or graphically, as shown in the Figure 1.8.

With the wave optic approach, on the other hand, it is possible to calculate the electric field, and therefore the shape of the modes, associated with the propagation in a single waveguide. A monochromatic wave of this type is a solution of the Helmholtz equation:

$$\left(\nabla^2 + k_0^2 n^2(\boldsymbol{r})\right) \boldsymbol{E}(\boldsymbol{r}) = 0 \tag{1.34}$$

And the resulting propagation modes form a complete base.

For the particular geometry used, invariant for translations along the axis *y*, and for the mode TE, a possible solution of (1.34) as the form:

$$\boldsymbol{E}(\boldsymbol{r}, t) = E_y(x) exp[i(\omega t - \beta_m z)] \tag{1.35}$$

Substituting this in the Helmholtz equation (1.34) one gets:

$$\frac{\partial^2}{\partial x^2} E_y(x) + [n^2(x) k_0^2 - \beta_m^2] E_y(x) = 0 \tag{1.36}$$

where n(x) is the profile of index refraction and, as shown in Figure 1.7, it is n_2 in the core and n_1 in the cladding.
The equation (1.36) has to be solved separately in the core and in the cladding, because the dynamic of the electric field is completely different in these two regions.

In the core $n_2^2 k_0^2 - \beta_m^2 > 0$, which can be seen from equation (1.32), by knowing that $n_2 < n_{eff\,m} < n_1$. Therefore the solution has an oscillatory form and equations are easier understandable if the electric field is expressed under the form $E_y^m(x) = a_m u_m$, where a_m is the amplitude and u_m the field distribution:

$$u_m(x) \propto \begin{cases} \cos\,(h_m x) & m = 0,2,4 \\ \sin\,(h_m x) & m = 1,3,5 \end{cases} \qquad - W/2 \leq x \leq W/2 \tag{1.37}$$

where h_m is the transverse propagation constant, defined as $h_m = \sqrt{n_2^2 k_0^2 - \beta_m^2} = \frac{2\pi n_1 \sin \bar{\theta}_m}{2}$.

In the cladding, on the contrary, $n_2^2 k_0^2 - \beta_m^2 < 0$, therefore the solution is exponential, and after re-expressing $E_y^m(x)$ as done in the core, the field distribution u_m has the form:

$$u_m(x) \propto \begin{cases} \exp(-\gamma_m x) & x > W/2 \\ \exp\,(\gamma_m x) & x < W/2 \end{cases} \tag{1.38}$$

where γ_m is the wave extinction coefficient, defined as $\gamma_m = \sqrt{\beta_m^2 - n_1^2 k_0^2} = n_1 k_0 \sqrt{\frac{\cos^2 \bar{\theta}_m}{\cos^2 \theta_c} - 1}$. This part of the wave is named *evanescent*, ad it is the base for treating the coupling mode theory, as discussed in the following paragraph.

To determine the complete form of the electric field it is necessary to know also the amplitude a_m. To achieve this it is sufficient to impose the continuity of the electric field at the surface of separation core-cladding $E_{core}\,(x = \pm W/2) = E_{cladding}\,(x = \pm W/2)$ and to normalize the distribution of the mode: $\int_{-\infty}^{+\infty} u_m^2(x) dx = 1$.

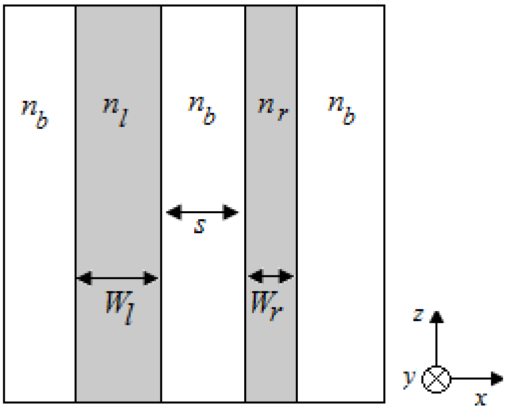

Figura 1.9: Structure composed with two different waveguides. W_l, n_l are the width and the index refraction of the left one; W_r, n_r of the right one; s is the inter-guide distance; n_b is the bulk index refraction.

This description can be generalized for waveguides confines in two dimensions or with an arbitrary index profile along x . In this case the solution of the problem has to be found numerically.

1.2.2 Coupled mode theory

The optical coupling is a phenomenon that occurs when multiples waveguides are placed sufficiently near to each other, so that the light injected in one guide can transfer to a near one. More precisely the modes of propagations of the light confined in a guide are coupled with those in a near guide.

Different types of formalisms were been developed to study theoretically this mechanism, but in this work only the coupled mode theory (CMT) is briefly described.
This theory was developed by Yariv in 1973 and it is based on the coupling by evanescent waves, that occurs when a second waveguide is placed sufficiently near the first one, so that the two evanescent waves can superimpose each other. This formalism was created to study the coupling of two guides, where the equations can be completely resolved, but it can also be used to describe more complex and extended structures: it is sufficient to generalize the theory using a “tight-binding” type approximation.

The base of the theory is to treat the presence of the second waveguide as a perturbation of the problem that involves the single guide

When a second waveguide is taken into account, as shown in Figura 1.9, the propagating wave is not longer a solution of the Helmholtz equation but, in the approximation of coupled mode theory, of:

$$\nabla^2 \boldsymbol{E}(\boldsymbol{r}) - \mu_0 \varepsilon_0 \varepsilon(r) \frac{\partial^2}{\partial t^2} \boldsymbol{E}(\boldsymbol{r}) = \mu_0 \frac{\partial^2}{\partial t^2} \boldsymbol{P}_{pert}(\boldsymbol{r}, t) \tag{1.39}$$

where ε(**r**) = n^2(**r**) is the space-dependent dielectric constant describing the waveguide, and $\mathbf{P}_{pert}$ is the perturbation polarization defined as:

$$\boldsymbol{P}_{pert}(\boldsymbol{r},t) = \varepsilon_0 \Delta\varepsilon(\boldsymbol{r})\boldsymbol{E}(\boldsymbol{r},t) = \varepsilon_0 \Delta n^2(\boldsymbol{r})\boldsymbol{E}(\boldsymbol{r},t) \tag{1.40}$$

To solve this equation the same geometry already used for the single guide is adopted, and as unperturbed base, its eigenstates are used. With this formalism, and for TE modes, the electric field can be rewritten as follows:

$$E(x,z,t) = \frac{1}{2}\sum_m a_m(z)\, u_m e^{i(\omega t-\beta_m z)} + c.c. \tag{1.41}$$

It is important to note that, in this case, the amplitude a_m is dependent upon *z,* in contrast to the case of a single guide, and that *E(x,z,t)* is actually the sum of the two electric fields which propagate separately in the two guides. Therefore the equation (1.41) can be rewritten as follows:

$$\begin{aligned} E(x,z,t) &= E_r(x,z,t) + E_l(x,z,t) \\ &= \frac{1}{2}\left(a_r(z)u_r(x)e^{i(\omega t-\beta_r z)} + a_l(z)u_l(x)e^{i(\omega t-\beta_l z)} + c.c.\right) \end{aligned} \tag{1.42}$$

where E_r represents the electric field propagating in the right guide and E_l in the left one. Indeed only the fundamental mode *m=0* is considered because experimentally the setup is adjusted only for this one. The variation of the amplitude of $a_r(z)$ and $a_l(z)$ include the information on the transfer of energy, that is obtained if waveguides are sufficiently close to each other.
Substituting (1.42) and (1.40) in (1.39), due of the approximation of slowly varying amplitude $\left|\frac{\partial^2}{\partial z^2} a_m(z)\right| \ll \left|\frac{\partial}{\partial z} a_m(z)\right|$, separating the contribution for the left and right guides and considering only one direction of propagation for the light, the coupling equations can be rewritten in the form [47]:

$$\frac{\partial}{\partial z} a_r(z) = -iC_{lr} a_l(z) e^{-i\Delta\beta z} - iC_{rr} a_r(z) \tag{1.43 a}$$

$$\frac{\partial}{\partial z} a_l(z) = -iC_{rl} a_r(z) e^{-i\Delta\beta z} - iC_{ll} a_{ll}(z) \tag{1.43 b}$$

Where Δβ is the phase mismatch within the two guides, defined as $\Delta\beta=\beta_l-\beta_r$ and C, for the right guide, is defined as:

$$C_{lr} = \frac{\omega\varepsilon_0}{4}\int_{left\ guide}\left[n_l^2(x) - n_b^2(x)\right]u_l(x)u_r(x)dx \tag{1.44 a}$$

$$C_{rr} = \frac{\omega\varepsilon_0}{4}\int_{left\ guide}\left[n_l^2(x) - n_b^2(x)\right]u_r^2(x)dx \tag{1.44 b}$$

where the influence extends on the left guide. These equation admit an analytic solution only if the two guides are identical. Equation (1.44) describes the *coupling constant* between the left and the right waveguides, while the second one represents only a small correction that can be normally neglected.

Finally, equations that are solved to study the light propagation in two waveguides are:

$$\frac{\partial}{\partial z} a_r(z) = -iC_{lr} a_l(z) e^{-i\Delta\beta z} \tag{1.45 a}$$

$$\frac{\partial}{\partial z} a_l(z) = -iC_{rl} a_r(z) e^{-i\Delta\beta z} \tag{1.44 b}$$

With initial conditions $a_l(0) = a_0$ and $a_r(0) = 0$, that correspond to consider the wave entirely coupled in the left waveguide.

In the case of identical guides the phase mismatch $\Delta\beta_z$ in null and coupling constants are all equal, so equations (1.43) can be further simplified:

$$\frac{\partial}{\partial z} a_r(z) = -iC a_l(z) \tag{1.46 a}$$

$$\frac{\partial}{\partial z} a_l(z) = -iC a_r(z) \tag{1.46 b}$$

In this way C admits the analytic solution:

$$C(z) = \frac{2h_m^2 \gamma_m e^{-\gamma_m s}}{\beta_m (W + 2/\gamma_m)(h_m^2 + \gamma_m^2)} \tag{1.47}$$

where γ_m is the wave extinction coefficient, h_m the transverse propagation constant, W the width of the guide and *s* the inter-guide distance, calculated between the two boundaries of the guides (Figure 1.9).

Finally, if more than two waveguides exist the equations (1.46) can be rewritten in a single expression:

$$\frac{d}{dz} a_n(z) = -iC[a_{n-1}(z) + a_{n+1}(z)] \tag{1.48}$$

This is the fundamental equation of the CMT, which is also the generalization for a larger number of identical waveguides equally spaced, in which only the fundamental mode TE_{00} propagates and where each guide is influenced only by its first neighbors.

1.2.3 Resonant case

In this paragraph the analogy between quantum and optical quantities is explained for the three-state STIRAP and EIT. We consider the resonant case, where the detuning Δ between the Bohr frequency and that of the exciting laser is null.

The quantum effect, as already explained, is governed by the Schrödinger equation:

$$\hbar \frac{d}{dt} \boldsymbol{A}(t) = -iH(t)\boldsymbol{A}(t) \tag{1.49}$$

Where $A(t) = [A_1(t), A_2(t), A_3(t)]$ is a three-component column vector of the population probability amplitudes defined in the base of unperturbed states ψ_1, ψ_2, ψ_3, and the Hamiltonian has the form:

$$H(t) = \frac{1}{2}\begin{pmatrix} 0 & \Omega_1(t) & 0 \\ \Omega_1(t) & 0 & \Omega_2(t) \\ 0 & \Omega_2(t) & 0 \end{pmatrix} \tag{1.50}$$

The equation describing the wave coupling reported (1.48) and in a more general presentation can be rewritten as:

$$\frac{\boldsymbol{d}}{\boldsymbol{dz}}\boldsymbol{A}(z) = -iH(z)\boldsymbol{A}(z) \tag{1.51}$$

Where $A(z) = [A_1(z), A_2(z), A_3(z)]$ is a three-component column vector of the electric field amplitudes propagating in each guide, and $H(t)$ is a matrix containing the coupling constants between the waveguides:

$$H(z) = \frac{1}{2}\begin{pmatrix} 0 & \mathrm{C}_{12}(\mathrm{z}) & 0 \\ \mathrm{C}_{21}(\mathrm{z}) & 0 & \mathrm{C}_{23}(\mathrm{z}) \\ 0 & \mathrm{C}_{32}(\mathrm{z}) & 0 \end{pmatrix} \tag{1.52}$$

In the Hamiltonian coupling constants are all different and z-dependents because the general case of guides not equally spaced has to be taken into account. This description indicates that it is possible to reproduce optically the two quantum phenomena of STIRAP and EIT..

The analogy between the quantum mechanics and the optic is linked to the observation that equations (1.48) and (1.50) have the same structure and, in particular, they are equivalent if a correspondence between temporal and z coordinate is established. In this way coupling constants $C_n(z)$ of the Hamiltonian (1.52) correspond to Rabi frequencies $\Omega_n(t)$ in (1.50) and the nth energy levels ψ_n to the nth waveguide.

The quantum resonance condition $\Delta_k = 0$ is optically reproduced using identical waveguides, having the same width and the same effective index.

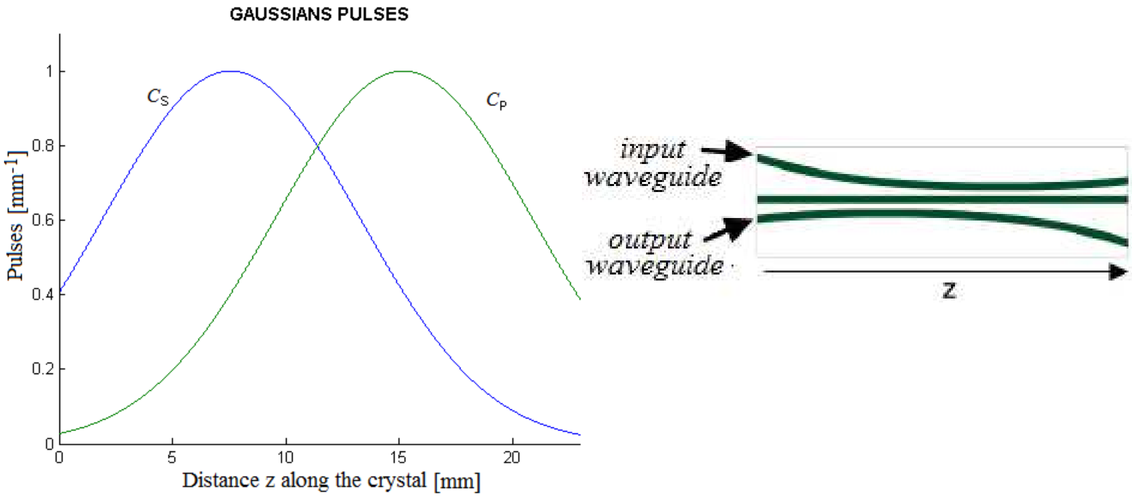

Figure 1.10: a) Exemple of gaussians pulses in the spatial conterintuitive sequence leading to the three-state STIRAP. C_P is coupling constant between the input waveguide and central one and Cs between the last and the cental one. b) Waveguide structure providing an optical analogies to the counterintuitive three state STIRAP process.

For the STIRAP mechanism three waveguides are necessaries to simulate the three energy levels and, as it was already seen in paragraph 0.01.1.2, it is important to implement the temporal counter-intuitive sequence of the pulses Ω_P and Ω_S. Knowing that the temporal coordinate is equivalent to a spatial one, this condition is optically translated in a spatial counter-intuitive sequence, so the Figure 1.2 becomes the Figure 1.19a, where pulses have the same shape but, now, a longitudinal dependence with the crystal length. This sequence is experimentally reproduced observing in equation (1.47) that the coupling constant has an exponential dependence on the inter-guide distance *s*, so a larger coupling constant implies a small distance between two waveguides and vice versa a small coupling constant a larger distance between them. In this way the variations of C_S or C_P are reproduced modulating *s* along the crystal, as shown in Figure 1.10b. In $z = 0$, as example, the input waveguide has a larger distance relative to the central one, to model a small C_P, The same logic was applied for the creation of the output waveguide.

The intuitive case is reproduced simply permuting the order of the gaussians pulses in Figure 1.10a, the waveguides take on the new structure presented in Figure 1.11

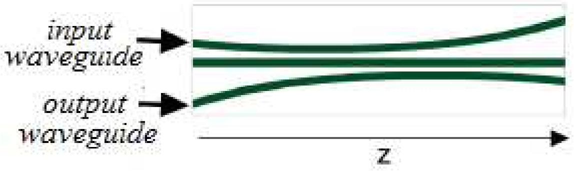

Figure 1.11: Waveguide structure providing an optical analogies to the intuitive three state STIRAP process.

For the EIT the fundamental condition is to have $\Omega_{pump} >> \Omega_{probe}$, and this is traduced by using linear waveguides, separated by a small inter-guide distance between waveguide 2 and 3, compared with the one between 1 and 2, as shown in Figure 1.12.

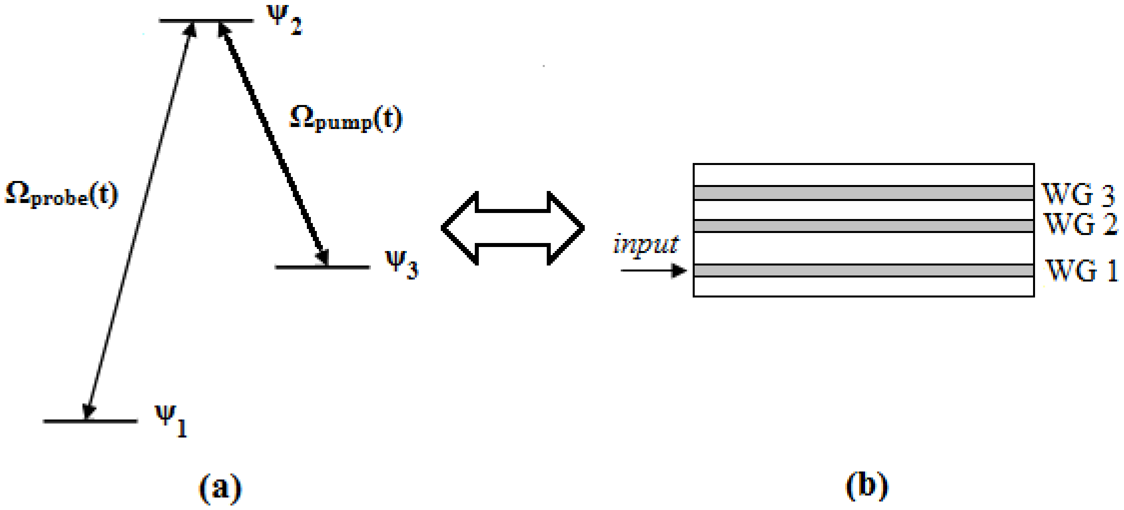

Figure 1.12: a)**:** Quantum system describing EIT effect. b)Waveguide structure providing an optical analogies to the EIT process.

1.2.4 Detuned case

The detuned case describes the optical analogy with the two-state STIRAP, where a detuning Δ is present. The analogy is based on the same consideration explained for the resonant case: the Schrödinger equation and the basic equations of the coupled mode theory have the same structure, so it possible to demonstrate quantum phenomena using optic experiments. The difference is in the Hamiltonian matrix. In quantum description, as explained in paragraph 1.1.2, the latter has the form:

$$H(t) = \frac{1}{2}\begin{bmatrix} 0 & \Omega(t) \\ \Omega(t) & 2\Delta(t) \end{bmatrix} \tag{1.53}$$

While the matrix for the optical analogue, containing the coupling constant can be written as follows [13]:

$$H(z) = \begin{bmatrix} 0 & C_{1,2}e^{i\Delta\beta_z} \\ C_{2,1}e^{-i\Delta\beta_z} & 0 \end{bmatrix} \tag{1.54}$$

Comparing these two matrixes, it can be noticed that the role of the detuning Δ in the CMT is played by a phase mismatch $\Delta\beta_z$ in equations (1.54) while C(z) is again the analogue of the Rabi frequency Ω(t). The two coupling constants $C_{1,2}$ and $C_{2,1}$ are not equals, because of the presence of $\Delta\beta_z$.

Usually the matrix (1.54) is rewritten in a different way to have a structure more similar to the Hamiltonian (1.53). This is realized using transformations:

$$A_1'(z) = A_1\sqrt{\frac{C_{1,2}}{C_{2,1}}}e^{-i\Delta\beta_z} \tag{1.50 a}$$

$$A_2'(z) = A_2(z) \tag{1.55 b}$$

In this new basis the Hamiltonian takes the form:

$$H = \begin{bmatrix} \Delta\beta & C \\ C & 0 \end{bmatrix} \tag{1.56}$$

where $C = \sqrt{C_{1,2}C_{2,1}}$ is the geometric mean of coupling constants between the guide 1 and 2 and Δβ becomes the equivalent of the detuning Δ.

To realize experimentally the optical analogy, two waveguides are necessary to simulate the two energy levels and the presence of a phase mismatch implies the use of waveguides with the same width but different effective refractive index, given that the latter is directly related to Δβ by the formula:

$$\Delta\beta = k_0\Delta n = \frac{2\pi}{\lambda}\Delta n \tag{1.57}$$

As it was seen for the three-state STIRAP, also in this case it is important to pass from a temporalcounterintuitive or intuitive sequence of pulses to a spatial one, but this time the gaussian variation is on Δβ and C. Experimentally the first one is realized with a gaussian variation of the index of refraction contrast, since they are connected as shown in equation (1.57), and the second

Figure 1.13: Waveguide structure providing an optical analogies to the counteintuitive two-state STIRAP process. The gaussian variation of Δβ is obtained a gaussian modulation of the refractive index, visible in the superior guide on a grey-scale color code,, while the variation of C obtained modulating the inter-guide distance.

one exploiting the exponential dependence of inter-guide distance, as already seen for the tree-state STIRAP. Following this schema, a structure as the one shown in Figure 1.13 is used to demonstrate optically the two-state STIRAP effect.

1.1.2 Diffusion trough aperiodic coupled waveguides array

The first example in photonics describing an aperiodic structure with a long-range order was described by Kohomoto et al.[44]. This approach is based on the fact that the Schrödinger equation describing the quantum system is analogue to the equation of the CMT theory. Kohomoto et al. proposed a 1D photonic quasicrystals structure using dielectric multilayers arranged in the so-called Fibonacci sequence. It was defined using a substitutional rule where the base blocks are two layers of two different thickness named long (L) and short (S), characterized by the fact that their rapport L/S is an irrational number. In this way the sequence cannot be retraced to a repetitive sequence of a highest common divisor and the behaviour of a quasicrystal is reproduced.

The order of L and S is decided following the iterative rules $L \rightarrow S$ and $S \rightarrow SL$, so starting with L the sequence is composed by elements : L, S, SL, SLS, SLSSL, etc..

In this work we have used the rule just explained to create an aperiodic 1D structure, as described in paragraph 2.4.3.

2 | RECONFIGURABLE WAVEGUIDES

In order to realize experimentally the schemes depicted in the preceding paragraph, it is convenient to use a flexible approach for rapid prototyping of complex optical structures without need for complicated technological steps. Commonly in the opto-electronic or telecommunications domains waveguides are realized using physical-chemical steps, but this approach requires a complex technology to be implemented. Moreover all these techniques have the disadvantage to create not alterable static structures, so each experimental configuration which can be tested requires a new sample, limiting the study of new phenomena.

In recent times [8,9] it has been shown that light – induced techniques can provide and efficient way to solve these issues. In particular, photorefractive materials, i.e. materials whose refractive index can be modified dynamically or semi – permanently by a light pattern, offer a convenient way to produce in short times and at low cost the complicated optical structures needed to verify the quantum – optical analogies described in the previous chapter

Above all this approach is particularly convenient because of its reconfigurability: each optical structure can be easily canceled and in this way only one sample is necessary.

Different techniques can be implemented to create reconfigurable photorefractive waveguides. In this work, two approaches were used: the lateral illumination technique in SBN and the photorefractive direct writing in Fe:LN. The first approach was already demonstrated, and used to test the optical analogue of STIRAP and EIT effect [8]. In this work we use it to demonstrate experimentally, to our knowledge for the first time, the optical two – state STIRAP phenomenon.

The second method was originally developed in the course of this thesis; it is meant to be a complementary approach with respect to the lateral illumination technique, because in this way semi – permanent structures are created, as opposite to the first technique which is fully dynamical. This offers some advantages when the produced structures have to be handled and moved for other applications. The effectiveness of this approach is proved by realizing and characterizing quasi – periodical optical structures.

In the following, the basic characteristics of photorefractive effect and of the materials used are reviewed and a description of the employed experimental setups is given.

2.1 The Pockels Effect

The Pockels effect, named also linear electro-optic effect, is a second order process, discovered in 1899 by Friedrich Pockels. It consists in a linear modification of the refractive index when the material is exposed to an electric field. Due to its linear nature in the electric field, this effect can occur only in non centro-symmetric materials.

This effect is described using the optical indicatrix, i.e. an ellipsoid whose central section, perpendicular to the direction of propagation of the incident beam, identify with its principal axes, the index of refraction of the material, according to the polarization of the propagating beam. It can be written in the following implicit form:

$$\frac{x^2}{n_x}+\frac{y^2}{n_y}+\frac{z^2}{n_z}=1 \tag{2.1}$$

where n_x, n_y, and n_z are the principal values of the refractive index along the three directions of an orthogonal reference system xyz, indicating the principals dielectric axes. In its general formulation, developed by Nye, equation (2.1) can be rewritten as:

$$B_{ij}x_ix_j=1 \qquad \text{with} \qquad B_{ij}=\frac{1}{\varepsilon_{ij}} \tag{2.2}$$

remembering that $n_{ij}=\sqrt{\varepsilon_{ij}}$.

When an arbitrary electric field **E**(x,y,z) is applied to the crystal, the refractive index ellipsoid can change its shape and orientation and this variation is described by the third rank electro-optical tensor r_{ijk} through the relation:

$$\Delta B_{ij}=r_{ijk}E_k \tag{2.3}$$

from the condition $B_{ij} = B_{ji}$ also the electro-optic tensor has to be invariant under permutation of indices i,j so $r_{ijk} = r_{jik}$. The tensor B, using the Voigt notation, can be rewritten as:

$$\begin{bmatrix} B_{11} & B_{12} & B_{13} \\ B_{21} & B_{22} & B_{23} \\ B_{31} & B_{32} & B_{33} \end{bmatrix}=\begin{bmatrix} B_1 & B_6 & B_5 \\ B_6 & B_2 & B_4 \\ B_5 & B_4 & B_3 \end{bmatrix}. \tag{2.4}$$

The electro-optic relation (2.3) can be rewritten as:

$$\Delta\left(\frac{1}{n^2}\right)_i=\sum_j r_{ij}E_j \tag{2.5}$$

or in its explicit form:

$$\begin{bmatrix} \Delta B_1 \\ \Delta B_2 \\ \vdots \\ \Delta B_6 \end{bmatrix}=\begin{bmatrix} r_{11} & r_{12} & r_{13} \\ r_{21} & r_{22} & r_{23} \\ \cdots & \cdots & \cdots \\ r_{61} & r_{62} & r_{63} \end{bmatrix}\begin{bmatrix} E_1 \\ E_2 \\ E_3 \end{bmatrix} \tag{2.6}$$

As the index variation is much smaller than 1 the equation (2.5) can be rewritten as follows:

$$\Delta n=-\frac{n^3}{2}r_{ij}E_j \tag{2.7}$$

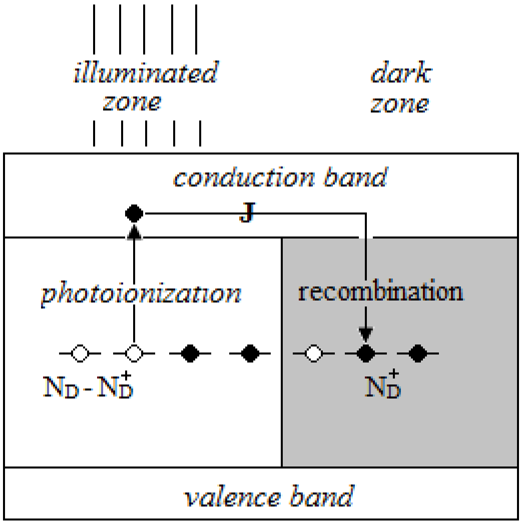

Figure 2.1: Description of the photorefractive effect following the band transport model.

2.2 Photorefractive Effect

The photorefractive effect is the refractive index variation of a material exposed to a non homogenous light pattern. This variation is realized as a result of two processes. The first one is the photo-excitation, and the resulting redistribution of electric charges inside the material due the external non uniform illumination; the final result of this charge unbalance is the creation of a strong space charge field in the material. The second one is due to the Pockels effect, as the internal field in turn modifies the refractive index .

This effect was observed for the first time in 1966 by Ashkin at al. [28] in $LiNbO_3$ and $LiTaO_3$. The refractive index variation is the origin of a wave front distortion of any beam propagating in the crystal. Because of this behavior initially the effect was regarded as a problem for the opto-electronic performances. Indeed initially this effect was classified as “optical damage”, and all initial studies had the purpose to decrease it.

The first model of the photorefractive effect was proposed by Chen in 1968 [29], where he highlights that the index variation in a material submitted to radiation can be exploited to record information carried by the light signal. He proposed a model based on the band transport, where the photo-induction mechanism is explained. This model considers a photorefractive material presenting donor impurities sufficiently far away from the conduction band, so that the thermal excitation can be neglected. The concentration of those donors is indicated as N_D.

A part of these impurities, having a density N_D^+, is ionized, so that they are apt to accept a moving charge. The energy transported by the incident beam permits to ionize filled impurities, so that they emit a charge (in this case we will consider only electron – type carriers). The generated electrons moves in the conduction band, until they are trapped at another ionized impurity elsewhere in the crystal. The generation rate of the moving electrons is the same of the ionized impurity, with the difference that the first ones are mobiles while the second ones are fixed. This schema is represented in Figure 2.1. If the electron is trapped in an illuminated zone it can be again photo-excited and the mechanism continues as long as it is trapped in a dark zone. In this way an electronic transfer from illuminated to dark zone is realized and this new charge distribution generates an internal static electric field named *space charge field* E_{SC}, in turn modifying the index refraction via the electro-optic effect.

This first model was later completed by Kukhtarev et al [30,31] in1978, developing a system of equation describing completely the effect just described.

$$\frac{\partial N_D^+}{\partial t} = (sI + \beta)(N_D - N_D^+) - \gamma_R n_e N_D^+ \tag{2.8}$$

$$\boldsymbol{j} = q\mu n_e \boldsymbol{E} + \mu k_B T\, \nabla \mathrm{n_e} + \mathrm{qsI}(N_D - N_D^+)\mathbf{L_{ph}} \tag{2.9}$$

$$\varepsilon_0 \varepsilon \nabla \boldsymbol{E_{sc}} = -q(n_e + N_A - N_D^+) \tag{2.10}$$

$$\frac{\partial \rho}{\partial t} + \nabla \boldsymbol{j} = 0 \tag{2.11}$$

The equation (2.8) is the trap generation rate where *s* is the cross section coefficient for excitation, *I* the incident light intensity, β the thermal excitation coefficient, γ_R the electron recombination constant and n_e the free electrons density. The first term of equation (2.8) takes into account that ionized donors are generated either by photo-ionization or by thermal excitation while the last term considers that the number N_D^+ decreases because of the electron recombination in a dark zone of the crystal.

The equation (2.9) is the current density which is due to the contribution of three terms. The first one is connected to the presence of an electric field, which can be either internal or externally applied, where μ is the electronic mobility and q the electronic charge. The second one the contribution due to the electronic diffusion which is connected to the gradient of the electron density, where k_B is the Boltzmann constant and T the absolute temperature. The third term is the photo-galvanic current describing the current generated in absence of electric field due uniquely to the photo-excitation. L_{ph} is the photo-galvanic drift vector.

Equation (2.10) is the Poisson equation describing the space charge field, where ε is the permittivity dielectric tensor and N_A is a background charge necessary to ensure the charge equilibrium.

Equation (2.11) is the continuity equation, where ρ is the charge density.

As we explain in the paragraph 2.3.4 and 2.4.4 ours structures are created submitting a photorefractive crystal to a localized illumination, so equation (2.8) to (2.11) has to be solved for this particular condition and not as it is usually made for the case of a periodic illumination. Normally the solution for our particular problem is found only numerically, but using suitable hypothesis analytic solutions can be found separately for the lateral illumination technique and the photorefractive direct writing.

2.3 Dynamical Optical structures inStrontium Barium Niobate

Strontium barium niobate (SBN) presents many properties that makes it a suitable candidate for many non-linear applications. This crystal is used to make both fundamental and applied studies thanks to its electro-optic, piezo-electric, pyro-electric and photorefractives properties [14, 15]. Actually it is already utilized for electro-optic modulator [16], phase conjugation [17], holographic storage [18], generation of spatial solitons [19, 20] and second harmonic generation [21].

2.3.1 SBN

The chemical formula of strontium barium niobate is $Sr_XBa_{1-X}Nb_2O_6$, usually abbreviated by the name SBN: x% ,where x is the strontium fraction present in the material. The most used composition for optical applications are $x = 61\%$ or $x = 75\%$.
SBN is obtained starting with a chemical compound made of a mixing of powders of $BaCO_3$, $SrCO_3$ and Nb_2O_6, and it is produced using different growing methods such as Bridgman [22], Stepanov [23, 24] or Czochralski [25] process, and the last one is the most often used.

SBN is a negative uniaxial crystal having the optical axis corresponding to the c-axis. In such anisotropic crystal the optical response of the material is described by its dielectric tensor $\hat{\varepsilon}$, which, due to symmetry properties, can be written, as a diagonal matrix:

$$\hat{\varepsilon} = \varepsilon_0 \begin{pmatrix} \varepsilon_{11} & 0 & 0 \\ 0 & \varepsilon_{11} & 0 \\ 0 & 0 & \varepsilon_{33} \end{pmatrix}. \tag{2.12}$$

At optical frequencies the permittivity of the material is usually described in terms of its refractive index and according to the polarization of the incident radiation, the crystal has two refractive indices, one ordinary $n_o = \sqrt{\frac{\varepsilon_{11}}{\varepsilon_0}}$ and the other one extraordinary $n_e = \sqrt{\frac{\varepsilon_{33}}{\varepsilon_0}}$. The presence of two different coefficients in matrix (2.12) determines the birefringent nature of the material, which is negative because the corresponding indices respect the relation $n_e < n_o$.

The refractive indices also depend on the value of the strontium fraction x and on the wavelength used. For the value of 633nm, the one used to explore the created structures, the corresponding values are:

	$x = 61\%$	$x = 75\%$,
n_e	2.2953	2.2987
n_0	2.3116	2.3117

SBNt is transparent in the range 0,3 – 6,0 µm, at room temperature it is ferroelectric and belongs to the crystallographic point group 4*mm*, therefore its electro-optic tensor has the form:

$$r = \begin{pmatrix} 0 & 0 & r_{13} \\ 0 & 0 & r_{13} \\ 0 & 0 & r_{33} \\ 0 & r_{51} & 0 \\ r_{51} & 0 & 0 \\ 0 & 0 & 0 \end{pmatrix} \tag{2.13}$$

The exact value of the coefficients depends strongly on the fraction x of strontium and on the wavelength. For SBN:61% and SBN:75% at 633nm, the coefficients r_{13} and r_{33} have respectively the values:

	$x = 61\%$	$x = 75\%$,
r_{13}	47 pm/V	67 pm/V
r_{33}	235 pm/V	1340 pmV

It is important to understand the defect structure of SBN, because it plays a roles for several optical properties, among which the photorefractive effect. In particular we focus the attention toward extrinsic and rather than intrinsic defects, because the first ones are important in the description of this effect.

Extrinsic defects consist in any other elements out of *Sr*, *Nb* and *O* that can enter in the crystal during the growth or subsequent treatments. In the specific case of photorefraction, dopants like chrome or cerium are intentionally added to increase the photorefractive sensitivity.
The most common dopant used is Cerium and, its introduction in the crystal leads to a photorefractive process dominatted by electrons rather than hole transport. It was highlighted [46] that for cerium concentration larger than 0.15mol% the photoconductivity becomes independent of the dopant concentration, indicating that the ratio between filled and empty traps is constant. The absorption is proportional to the total concentration of filled and empty traps and increases according to the cerium concentration, showing that the dopant is the origin of the absorption. For concentration below 0.15mol% experiments reveal that the cerium is present in SBN as Ce^{3+} and since the material is electron conductive the absorption of a photon by Ce^{3+} creates Ce^{4+}. In this case photorefraction properties depend on the ratio Ce^{3+} / Ce^{4+}.

2.3.2 Sample

The sample of SBN utilized in this work is SBN:61% doped with 0.002mol% of cerium. The SBN:75% would have permitted to have greater electro-optic coefficients r_{13} and r_{33} but the realization of such type of crystal having a good crystalline quality is much more difficult than for SBN:61%. The crystal, grown by Stepanov technique, was cut to obtain a sample of 5 x 23 x 5 mm as reported in Figure 2.3, and polished to optical grade, using standard procedures,.
It is also provided with two electrodes of graphite [27] perpendicular to the z axis, allowing the application of the external electric field along this direction. In this configuration the optical structures are confined only along the optical axis c, i.e. 1D waveguides are created, while along x and y they are limited by the crystal dimension.
The particular strontium/barium fraction and the percentage of the cerium characterizing the sample permits, in the experimental conditions employed here, a slow dynamic in the order of few seconds, allowing to follow in real time the mechanism of the waveguides formation.

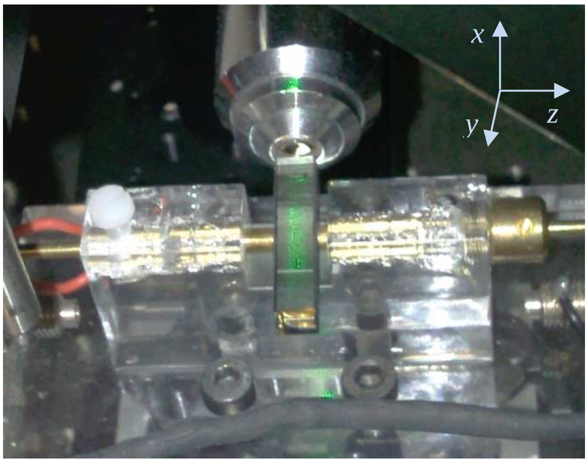

Figure 2.2: Photograph of SBN:61%. On the left and right the two electrodes are applied.

2.3.3 Waveguide Creation by lateral illumination technique

The lateral illumination technique exploits the photorefractive properties of SBN crystals to induce waveguiding structures having the same shape of a light pattern which is sent on one crystal face. The obtained structures are probed in real time by a secondary light beam which is launched in the waveguide from a face perpendicular to the first one. The waveguiding structures realized with this technique are fully dynamical: the refractive index change is locally increased proportionally to the light intensity, following it whenever this is moved and disappearing if the illumination is switched off. The lateral illumination technique therefore bases its operation in the fact that the light is guided by the light. The idea of the method is the following: an electric field applied to the sample reduces its refractive index everywhere by electro optic effect, but in the illuminated area this field is screened by a higher density of mobile charge carriers. The refractive index in this region results therefore increased with respect to the rest and a waveguide is obtained. An additional background illumination can be used in order to smooth the resulting index profile to avoid saturation effects.

This method has the important advantage to be reconfigurable, indeed each index variation disappears as soon as the illumination is switched off on a timescale of the order of one minute, so that the crystal can returns always to the initial situation. Because of the small relaxation time of the material, it is sufficient to turn off the external illumination to start the cancelling process in the crystal. By increasing the intensity of the external incoherent illumination I_D an homogenous redistribution of the charges can be accelerated, reporting the refractive index to the bulk value. This permits to make a very large number of experimental demonstrations. On the contrary this method has the disadvantage that the optical structure exits till the external illumination is on and the external electric field is present, so the crystal cannot be moved from the setup.

To find an analytic expression of the charge space field, we follow the treatment described in [32] and [27], solving Kukhtarev equations.

Since the realized structures are straight structures aligned perpendicular the ferroelectric c axis, the problem can be treated in one dimension, in particular along *z*, parallel to the *c* axis of the crystal. A stationary situation is considered, describing the electric field after the initial transitory situation. Besides that, the contributions associated to charge diffusion are neglected, because an illumination beam with width larger than the Debye length L_D is used, with $L_d = \frac{2\pi}{k_d}$ where $k_d = \sqrt{\frac{e^2 N_{eff}}{\varepsilon_0 \varepsilon k_B T}}$ and $N_{eff} = \frac{N_D^+(N_D - N_D^+)}{N_D}$. L_D is in the order of 1µm for the majority of the photorefractive crystals. The photo-galvanic effect is also neglected, because this effect is not relevant for SBN. This effect explains because an external electric field E_0 has to be applied to the crystal, indeed the external illumination makes the material much more conductive but the conduction electrons are emitted along a privileged direction. Under these hypothesis equation (2.9) simplifies to:

$$\boldsymbol{j} = q\mu n_e(\boldsymbol{E_{sc}} + \boldsymbol{E}_0). \tag{2.14}$$

On the other hand, from eq. (2.8) it turns out that at equilibrium the carriers concentration is given by:

$$n_e(z) = \frac{[sI(z) + \beta](N_D - N_D^+)}{\gamma_R N_D^+} \tag{2.15}$$

So that the material become more conducting where the illumination is strong. In these conditions, by substituting eq. (2-15) into eq. (2-14) it can be shown that the space charge electric field has the following expression:

$$E_{SC}(z) = E_0 \frac{I_D}{I_D + I(z)} \tag{2.16}$$

where E_0 is the electric field applied to the crystal through the electrodes, I(z) the intensity of the laser beam illuminating the crystal, i.e. the lateral localized illumination and I_D is the dark intensity. The latter has two contributions, one is the thermal excitation of mobile charges while the other one is due to the background illumination. It is important to notice in equation (2.16) that the electric field E_0 is decreased in the illumination zone according to the ratio $I(x)/I_D$.

Initially the crystal has an homogeneous n_0 refractive index, corresponding to its bulk value. Applying the external electric field E_0 along *c* axis, due to the Pockels effect, the index variation is equally decreased according to:

$$\Delta n_{I(z)=0} = -\frac{n^3}{2} r_{eff} E_0. \tag{2.17}$$

When the localized illumination is applied, due to the photorefractive effect, the electric field seen by the crystal is the one expressed in (2.10), so that the index modulation can be expressed as follows:

$$\Delta n_{I(z)\neq 0} = -\frac{n^3}{2} r_{eff} E_0 \frac{I_D}{I_D + I(z)} \tag{2.18}$$

Consequently the refractive index contrast profile becomes:

$$\Delta n = \Delta n_{I(x)\neq 0} - \Delta n_{I(x)=0} = \Delta n_0 \frac{I(x)}{I_D + I(x)} \tag{2.19}$$

where $\Delta n_0 = -\frac{n^3}{2} r_{eff} E_0$. The situation is depicted in figure 2,4c. It is easy to see that the refractive index in the illuminated region is higher compared to the one in the dark, so that illuminated areas can in principle be used as the core of the light induced waveguide. Equation (2.16) displays another important property of the obtained refractive index profile: saturation. If $I_D \ll I(z)$ eq. 2.19 can be approximated as $\Delta n(z) \approx \Delta n_0 \frac{I_D}{I(z)}$ and the refractive index contrast is determined by the illumination profile (remember that Δn_0 has a negative sign) with an amplitude proportional to I_D. On the other hand, if $I_D \gg I(z)$, i.e. outside the illuminated area, or for very weak illumination patterns, the refractive index profile does not follow anymore the illumination profile, $\Delta n(z) \approx \Delta n_0 = \text{constant}$. It is therefore important to set a correct value of the background illumination, in order to have a large refractive index contrast on one hand and to reproduce correctly the illumination pattern on the other.

Experimentally this is obtained adding in the setup an halogen lamp which illuminates uniformly the crystal. The creation of a stabile waveguide exploiting this method requires characteristic times of about 30seconds, thanks also to the high electro-optic coefficient r_{33}.

Concerning the cross section of the illumination profile, it can be shown that in practice, a true square profile is practically impossible to obtain, due to aberrations and to the finite optical resolution limit of our setup. A more realistic picture [27] is a waveguide following a super gaussian profile:

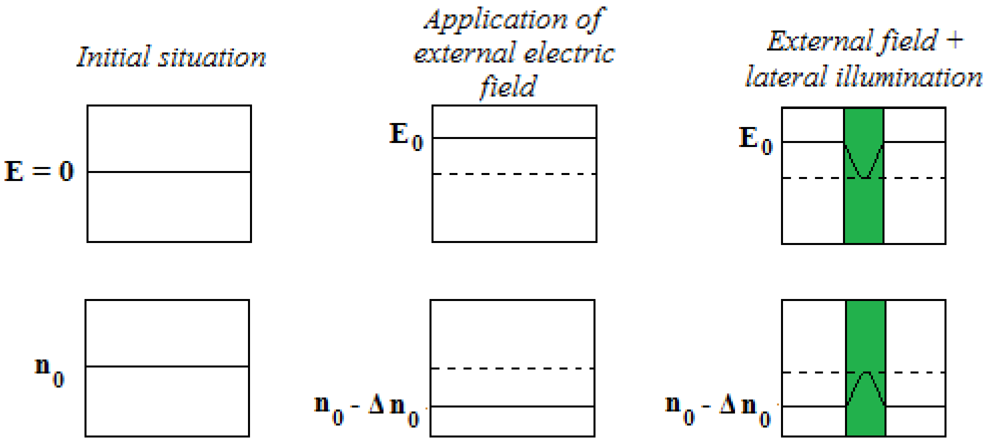

Figure 2.3: Description of the process permitting to create waveguide in SBN with the lateral illumination technique.

$$I(x) = I_0\left[e^{\left(-\frac{x-p}{l}\right)^6} + e^{\left(-\frac{x}{l}\right)^6} + e^{\left(-\frac{x+p}{l}\right)^6}\right] \tag{2.20}$$

where l is the half width of the super gaussian at $1/e^2$ and p is the structure periodicity

2.3.4 Experimental Setup

The creation of photo induced waveguides, whose physic principles are described in paragraph 2.3.2, is made utilizing the setup presented in Figure 2.4 and the so called lateral illumination technique.

The control beam used to obtain the illumination profile inducing the waveguides is obtained from a Nd:YAG laser characterized by a wavelength of 532nm, with a power of about 200mW. This one passes through a spatial filter, a spherical lens (SL), which enlarges it, and a polarizing beam splitter, is used to select the vertical polarization of the beam. After that, the beam with the right polarization hits a spatial light modulator (SLM) Holoeye^{TM} LC-R 1080, the key instrument of the setup This device permits to reproduce the waveguides on the SBN. It is formed by a nematic liquid crystals cell of 16.39 x 10.56 mm steered by a computer. Initially nematic crystals are all oriented in the same direction but, when an electric field is applied, they turn and the degree of rotation depends on the value of the applied electric field. The variation on crystal orientation induces a variation of the reflected beam polarization. This operation is software controlled, inserting in the control program a gray scale image having 256 different type of gray levels and the dimensions of 1920 x 1200 pixels, to be in accordance with SLM dimension. This condition is due to the fact that the maximum polarization change in the beam is induced for white regions of the image, while a black part of the image one not modify the beam's polarization. The intermediaries gray colors have a partial effect in the polarization variation. The reflected beam having the polarization rotated in accordance with the image used, goes back toward the beam splitter and the variation on the polarization is traduced in a variation of

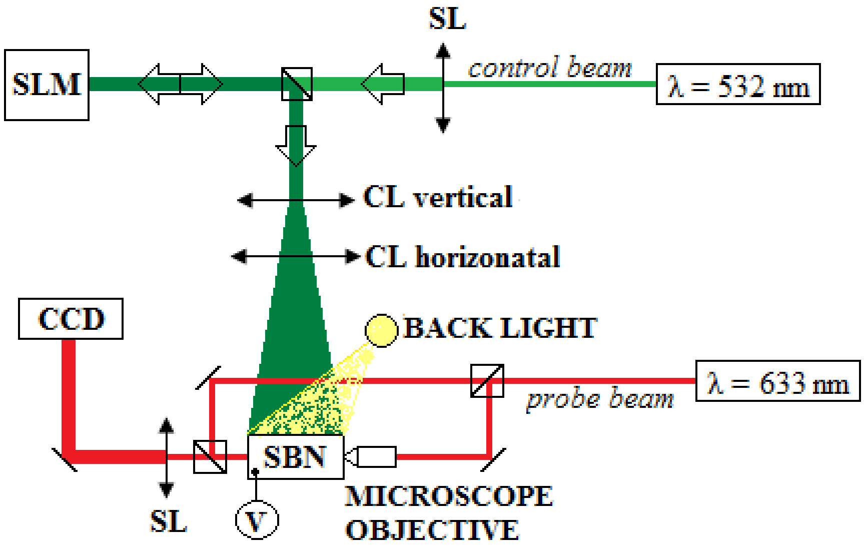

Figure 2.4: Description of the setup used to create photoinduced waveguides.

intensity, as it reflects toward the SBN the horizontal component, that is the part of the beam that has been modified.

The beam passes through two crossed cylindrical lens (CL), one vertical and the other horizontal. which are used to adapt the SLM image to the sample dimensions. Because of the presence of this system of lenses, to create a correct image in the SLM, the conversion due to the imaging between the SLM and the sample should be taken into account:

$$1 \text{ pixel}_{SLM} = 1.2\mu m_{SBN}$$

The control beam is finally sent to the crystal to create the waveguides. The SBN is also subjected to an electric field and a background light, necessary during the inscription process, as seen in the paragraph 2.3.2. The electric field is applied along the c axis of the crystal thanks to its graphite electrodes while the supplementary illumination supplied by a white halogen lamp whose intensity can be regulated.

The probe beam is a He-Ne laser at the wavelength of 633nm, and polarized along the $\hat{c}$ axis of the SBN. The beam is divided into two parts to create also a Mach-Zehnder interferometer, useful to measure the refractive index contrast in the waveguides (see Figure 2.5). One part of the probe beam propagates in free space while the other one is coupled into the crystal by a microscope objective, to investigate the created structure. Finally the two beams are recombined, expanded with a spherical lens and the resulting image is collected by a CCD camera. The total magnification of the collecting system is given by:

$$1 \text{ pixel}_{CCD} = 0.73\mu m_{SBN}$$

2.4 Photorefractive Direct writing Iron doped Lithium Niobate

2.4.1 Fe:LN

Lithium niobate single crystal ($LiNbO_3$, or LN) presents many properties that makes it a great candidate for many linear and non-linear optical applications such as waveguides, electro-optic modulators, second harmonic generators, holographic devices, sensors.

It is an artificial crystal, described the first time in 1928 by Zachariasen [34] and synthesized the first time in 1965 by Ballman, using Czochralski technique [35]. It is one of the four compounds of the pseudo-binary system $Li_2O-Nb_2O_5$, besides $Li_2Nb_{28}O_{71}$, Li_3NbO_4 and the lithium triniobate $LiNb_3O_8$, and it is colorless and insoluble in water and organic solvents. It is a pyro-electric, piezo-electric and ferroelectric material. At temperatures lower than the Curie point, which is about 1150°C, it has a spontaneous polarization, which disappears at higher temperatures in the paraelectric phase.

LN can is normally produced normally using a chemical composition characterized by a lithium deficiency, differing from the stoichiometric formula (50 mol% Li_2O): the composition corresponding to this point is defined as congruent and the relative molar percentage of Li_2O is 48.6 mol% [36]. This composition is preferred because the melt and the growing crystal have the same composition, so these crystals show the highest uniformity of their chemical and physical properties. On the contrary, in other cases, such as stoichiometric materials, the composition of the melt and the crystal are slightly varying during the growth and the crystal becomes non-uniform, particularly along the growth axis.

LN is a negative uniaxial crystal having the optical axis correspond to the ferroelectric c-axis. In such anisotropic crystal the optical response of the material is described by its dielectric tensor $\hat{\varepsilon}$, which, due to symmetry properties of LN, can be written, as a diagonal matrix:

$$\hat{\varepsilon} = \varepsilon_0 \begin{pmatrix} \varepsilon_{11} & 0 & 0 \\ 0 & \varepsilon_{11} & 0 \\ 0 & 0 & \varepsilon_{33} \end{pmatrix}. \tag{2.21}$$

At optical frequencies the permittivity of the material is usually described in terms of its refractive index. According to the polarization of the incident radiation, the crystal have two refractive index, one ordinary $n_o = \sqrt{\frac{\varepsilon_{11}}{\varepsilon_0}}$ and the other one extraordinary $n_e = \sqrt{\frac{\varepsilon_{33}}{\varepsilon_0}}$. The presence of two different coefficients determines the negative birefringent nature of the material, as indexes respect the relation $n_e < n_o$. Their values are strongly dependent on the temperature, composition, and beam wavelength: for a congruent sample at room temperature and for 633nm and 532nm beams (those used in this work) they are respectively:

	532 nm	633nm
n_e	2.23357	2.20217
n_0	2.32319	2.28641

The pure LN is transparent from about 0.35μm to 5μm and belongs to the crystallographic space symmetry group *R*3*c*, point group 3*m*, therefore its electro-optic tensor has the form:

$$r = \begin{pmatrix} 0 & -r_{22} & r_{13} \\ 0 & r_{22} & r_{13} \\ 0 & 0 & r_{33} \\ 0 & r_{42} & 0 \\ r_{42} & 0 & 0 \\ -r_{22} & 0 & 0 \end{pmatrix}. \tag{2.22}$$

These coefficients have a linear dependency with the temperature, as shown e.g. by P. Górsky et al. [37] in the range 20÷200◦C, and in particular at room temperature they have the values:

r_{22} = 3.4 pm/V
r_{42} = 28 pm/V
r_{13} = 8.6 pm/V
r_{33} = 30.8 pm/V.

The defect structure of LN is of main importance to understand, because it deals with many optical properties, in particular with the photorefractive effect. As a matter of fact, since the discovery of this effect, great effort has gone into the understanding of the role of defects in the physical properties of the material. In particular we focus the attention in extrinsic and not intrinsic defects, because the first ones are more important in description of the photorefractive effect.

Extrinsic defects consists in any other elements out of *Li*, *Nb* and *O* that can enter in the crystal during the growth or subsequent treatments. In the specific case of photorefraction the dopant used may have two purposes:
- to suppress the effect as in the case of *Mg*, *Zr*, *Zn* and *Hf* .
- to enhance it as for *Fe*, *Cu*, *Mn* and *Ni*.

For the aim of this work it is fundamental to utilize the second category of dopants and in particular sample doped with iron are used.

Iron doping provides in the visible range of the absorption spectrum a strong broad band responsible for the photoexcitation of the free electrons, which is a necessary condition for the realization of the photorefraction. It is well known that for $Fe{:}LiNbO_3$ the iron atoms are found in the valence states Fe^{2+} and Fe^{3+}, and that these states represents respectively donors and acceptors centers in photorefractivity.

By solving the equations (2.8 – 2.11), and as confirmed experimentally (see e.g. [45]), it can be shown that on iron doped $LiNbO_3$ crystal the space charge electric field follows a saturated exponential time evolution:

$$E = E_{sat}\left[1 - exp\left(-\frac{t}{T_0}\right)\right] \tag{2.23}$$

where E_{sat} is the field at saturation defined as $E_{sat} = \frac{K\alpha I}{\sigma}$ with K the Glass constant, α the absorption coefficient and σ the photoconductivity of the $LiNbO_3$; T_0 is the relaxation time defined as $T_0 = \frac{\varepsilon}{\sigma}$. These characteristics are determined by the specific sample in use. It can be shown that the photoconductivity (which determines the relaxation time) is proportional to the light intensity and to the *reduction ratio* $[Fe^{2+}]/[Fe^{3+}]$, while the saturation value of the space

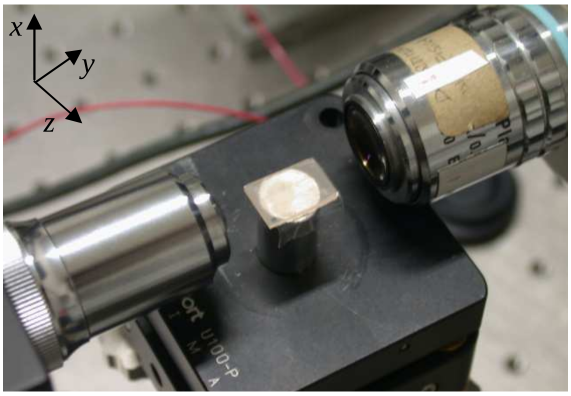

Figure 2.5: Example of Fe:LN sample having the titanium waveguide diffused in the superior surface, used to write waveguides and gratings.

charge field is proportional to [Fe^{3+}]. The doping characteristics of the sample therefore establish its photorefractive response.

2.4.2 Sample

The samples used in this thesis were grown by the Czochralski technique in our laboratories and obtained from the same boule. The samples are bulk doped with iron at nominal concentration of 0.1mol%, as this concentration is known to be the optimal one for maximizing the photorefractive properties [38] The samples were oriented, cut in slabs with the major surface perpendicular to the *x* direction and polished to optical grade, using standard procedures. All the resulting samples were oxidized using a thermal treatment in wet oxygen atmosphere, as verified by optical absorption. In these conditions and for this doping level, the saturation value of the photorefractive space charge field E_{sc} is expected to be about 10^8V/m, which lead to a maximum expected variation of the refractive index compared of about 10^{-4}.

.

In our experimental setup for direct beam writing, these samples are scanned with a focused laser beam with an intensity of about $5 \cdot 10^9$ W/m^2 in the focal spot (see paragraph 2.4.3)). Assuming a reduction degree between 0.001 and 0.01, a typical value, it turns out that the photoconductivity has an expected value of about 10^{-8} - 10^{-9} Ω^{-1} cm^{-1} and consequently the dielectric relaxation time T_0 is in expected to be in the millisecond range. Using these values it possible to calculate the variation of the electric space charge field in function of the time using (2.23), reported in Figure 2.6.

The photorefractive characteristic time of our sample can be compared with the time needed to the writing beam to scan a length equal to a spotsize, in order to estimate the optimal scanning speed. Considering a beam diameter of about 2μm and a photorefractive saturation time of 1ms, it turns out that an optimal speed to reach the saturation value of the space charge field is in the range of 1000μm/s. This value allows for scanning an area of 2 x 2 mm^2 with 300 lines in the reasonable time of 200s. In principle, working at faster speed in order not to have the space charge field saturated, should allow for the realization of graded index structures, as it is achieved with the lateral illumination technique.

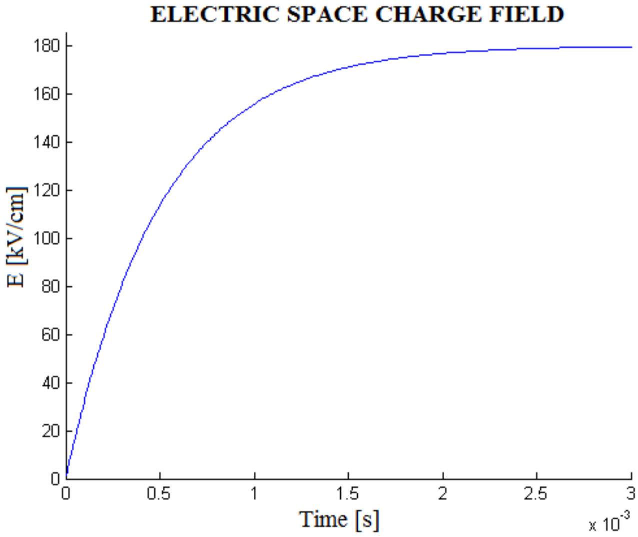

Figure 2.6: Electric space charge field in function of the time estimated for Fe:LN samples light up with a gaussian beam of intensity of $5 \cdot 10^9$ W/m^2.

As it will be explained below, the direct beam writing technique produces nearly vertical optical barriers extending from the sample surface in the bulk of the sample for some tenth of microns, so that the light confinement is only lateral along the crystallographic z direction. In some cases a vertical confinement may be desirable, so that we explored also the possibility to write lateral optical index structures on the top of a preexisting fixed slab waveguide. To this aim on some slabs, a local doping was performed to create a waveguide by titanium in-diffusion at one of the two major surfaces. Initially a thin film of Ti was deposited by magnetron sputtering for 180 seconds, using a power of 80W and an initial chamber pressure of 5 x 10^{-6} mbar, after that a thermal diffusion was made at a temperature of 1050°C for two hours in air atmosphere: these values permit to obtain a planar and a mono-mode guide at the surface for the wavelength of about 650 nm, later used to study the samples.

The diffused samples were characterized by Secondary Ion Mass Spectrometry (SIMS) in order to obtain the concentration profile of the iron and titanium. This characterization shows that the iron concentration is constant, as expected, while that one of titanium follows a semi-gaussian evolution, with the maximum at the surface and a width at half amplitude of about 1.5µm, as shown in Figure 2.7. From the concentration profile it is possible to know the corresponding index variation, using the equation: [50]

$$\Delta n = k\, C^{\gamma} \tag{2.24}$$

where k and γ are constant depending on the element diffused and C is the concentration expressed in atoms/cm^3. For the titanium diffused in Fe:LN it is known from the literature that, if the extraordinary polarization is utilized, $k = 1.2 \cdot 10^{23}$ cm^3 and $\gamma = 1$. The corresponding profile is reported in Figure 2.7, where it can be noticed as that the maximal contrast obtainable is 0.0113.

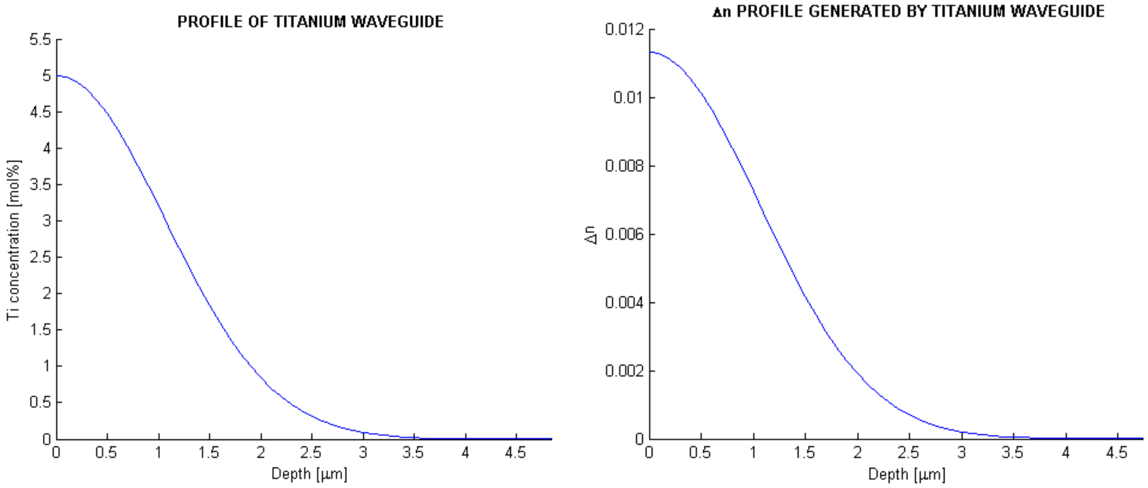

Figure 2.7: a) Concentration profile of the titanium diffused in sample of LN bulk doped with iron in function of its depth. b) Variation of the index refraction generated by the presence of titanium in function of sample depth

2.4.3 Waveguide creation

The optical structure creation in LN using the photoinduced direct writing exploits, as for the lateral illumination technique, the photorefractive effect.
In this case a focused laser beam is scanned along the sample surface to write the desired structures. Also this one is a reconfigurable method because every variation in the refractive index can be easily canceled by illuminating the sample with a sufficiently intense homogenous incoherent light. The great difference between the other method is in that this way, due to the long dark relaxation time of the material, the optical structures can be considered as permanent. This offers the great advantage that the sample can be moved from the setup making it available for following characterization or utilizations.
Of course, because of their reconfigurability, it is necessary to pay attention on the wavelength and on the intensity of the light used for the following characterizations, in order not to erase the produced structures.

An analytical solution for the Kukhtarev equations in this case is not easy, on one hand because the writing beam has a three dimensional structure, on the other because it is moving along a given direction. A rigorous treatment for the full problem could be done only numerically, but two cases [33,39] were reported in literature that could help understand some aspects of the technique. The first model developed by Zozulya and Anderson solves the problem for a static Gaussian beam focused at the surface of a Fe:LN sample, with the beam polarized along the z direction. The other interesting situation corresponds to the solution of a one dimensional problem similar to the one considered in paragraph 2.3.3. This latter case is meaningful if we consider that the resulting refractive index profile along a written line is probably not so different from this case.

The Zozulya-Anderson model considers a fixed single gaussian beam polarized along z axis of a photorefractive media, which enters in the face x = 0 and propagates along the axis x, and exits at x = L. The crystal is cut along crystallographic axis, and the beam diameter is much more small than the size of the sample, so that its size is considered to be infinite. The photo-galvanic current is generated along z.

Using these conditions, the equations are completely solved finding the distributions of the electric charge, potential and current. From these equations, the index variation can be obtained from using the electro optic effect. This is determined starting from the variable ν(r), the normalized non linear addition to the refractive index of the medium, defined as:

$$\nu(\boldsymbol{r}) = \frac{k}{2k_D} n^2 \tilde{E} \boldsymbol{e}_p \cdot (\hat{\boldsymbol{r}}_{el} \cdot \boldsymbol{\nabla}\varphi) \cdot \boldsymbol{e}_p \tag{2.25}$$

Where k is the wave number of the electromagnetic radiation in the medium k = 2πn/λ, n is the index refraction, $k_d = \sqrt{\frac{e^2 N_A}{\varepsilon_0 \varepsilon k_B T}}$, $\tilde{E} = \frac{k_B T k_d}{e}$, e_P is the unit vector in the direction of beam polarization, $\hat{r}_{el}$ is the electro-optic tensor and φ is the dimensionless potential of the electric field defined as $\nabla\varphi = -\frac{k_D \boldsymbol{E}}{\tilde{E}}$. Considering that in $LiNbO_3$ the most important component of the electro-optic tensor is r_{33} the equation (2.25) can be rewritten as follows:

$$\nu(\boldsymbol{r}) = \frac{k}{2} n^2 r_{33} \hat{E} G(\boldsymbol{r}) \tag{2.26}$$

where $G(\boldsymbol{r}) = \frac{1}{k_d}\frac{\partial\varphi(r)}{\partial z}$. Since ν(r) ∝ G(**r**) we shall refer to G as the normalized non linear refractive index. The distribution of the potential φ is completely known developing all equations of the Kukhtarev model so, finally, the normalized refraction index, apart from some proportionality constants, has the expression:

$$\nu(y,z) \approx -k\frac{z}{I_b} - \alpha\frac{k}{2}\frac{3z^2+y^2}{I_{NL}^2} + \frac{1}{2}kn^2 E_{ph} r_{33} \tag{2.27}$$

where $I_b = \frac{k_D d^2}{8n^2 r_{33}\tilde{E}}$, $\alpha = \frac{\sqrt{\pi \ln I_D^{-1}}}{4}$, $I_{NL}^2 = \frac{d^2 E_{ph} I_D}{8n^2 r_{33}}$ and d is the width at half amplitude of the gaussian beam. In Figure 2.8 G(**r**), and its projection along y and z are reported. As it can be seen along the z coordinate the index variation is initially increased compare to the bulk value, but overall a fixed gaussian beam polarized along *z*, propagating along *x* generates a negative variation.

In our case the situation is similar to the one just described with the difference that the gaussian beam scans the surface along y, so the refractive index profile along z is expected to be similar to the one reported in Figure 2.8, as it is verified in chapter 4 using far-field characterization of the samples.

The Bian's model [39] solves Kukhtarev equations supposing a cylindrical gaussian beam with distribution:

$$I(x,z) = I_0(0,z)e^{\frac{-2x^2}{w^2(z)}} \tag{2.28}$$

propagating along the z direction. The spatial extent of the gaussian beam along the direction perpendicular to the c-axis is assumed to be infinite and the polarization is considered along the c-axis. This model gives important information on the space charge electric field considering our

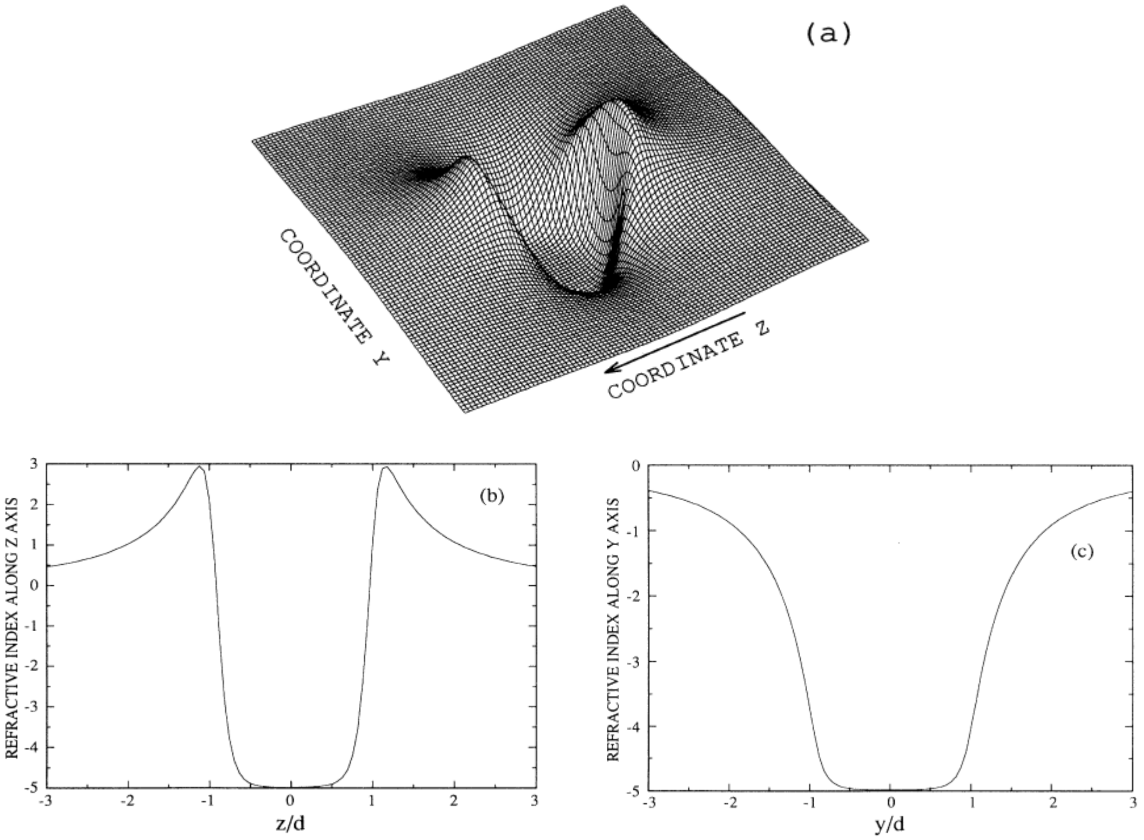

Figure 2.8: a) Numerical simulation of the non linear refractive index generated by a gaussian beam propagating along x. b) Projection of the index along z and c) along y.

technique invariant in the scanning direction, so reducing the problem to single dimension. In addition in the model the crystal is supposed to be short–circuited. In addition along the x direction the spatial extend w(z) of the gaussian laser beam is supposed to be much less than the width of the crystal. With these approximations the space charge field E_{SC} results to have the expression, which is identical to equation (2.16):

$$E_{SC} \approx -E_p \frac{I}{I+I_R+I_D} \tag{2.29}$$

where I is the illumination generated by the gaussian beam, $E_P = \frac{k\gamma N_A}{e\mu}$ is the photovoltaic field constant and $I_D = \frac{\beta}{s}$ is the so-called dark irradiance.

This equation is not rigorously valid for our case because samples are not short-circuited and $I_R = 0$ but it permits anyway to have important information on the space charge electric field creating in the LN during the illumination with a gaussian beam. When $I >> I_D$, which is the case of our illumination, the E_{SC} is proportional to the photovoltaic contribution of the field, corresponding, as will be explain in the paragraph 2.4.2, to the electric field at saturation.

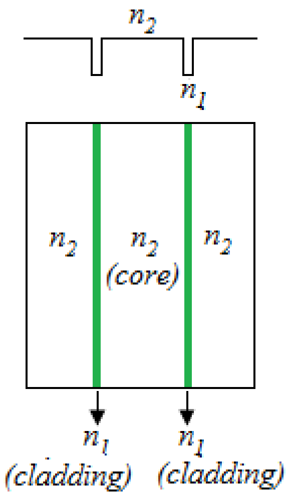

Figure 2.9: In the upper part of the image index refraction profile after writing of the optical barriers. In the lower one, picture of a waveguide.

The Zozulya-Anderson and the Bian's model show that the index variation is negative, independently of the exact form of the profile. Therefore this technique, differently from what discussed in the case of SBN and lateral illumination technique, can be used to generate optical barriers instead of a guiding core, as shown in Figure 2.9. This implies that the waveguide creation requires at least two scans along the sample to create the claddings zone around the core. Because of this fact this technique can be considered the specular of the one used to create waveguides in SBN.

2.4.4 Experimental setup

The experimental setup used to create waveguides, periodic and aperiodic Fibonacci gratings in sample Fe:LN is presented in Figure 2.10.

The structures are created in the sample using a continuous Ti:Sapphire laser characterized by a wavelength of 532 nm, a rectilinear vertical polarization and an initial power of 1Watt. The beam passes through a shutter and through a series of filters to attenuate it. Finally the beam is sent to a 100x microscope objective, as shown in Figure 2.10a. The power of the beam on the sample has been set to 17 mW, after a preliminary study which indicated this value as a good compromise between the writing velocity and the quality of the realized structures.

The objective can be translated along the optical axis, as shown in Figure 2.10b. Its translation is allowed by a piezo actuator, controlled by a computer. Exiting from the microscope objective , the beam has an estimated focus spot size of 1-2μm, a power density in the order of $5 \cdot 10^9$W/m^2 and the polarization parallel to the x axis.

The sample is placed above a computer–controlled translation stage, which can be moved along x and y axis with a resolution step of 0.5μm and velocities in the range 1μm/s – $3 \cdot 10^4$ μm/s. The sample can be also manually tilted in order to have its surface parallel to the translation directions. The beam is partially reflected at the sample surface, and this light goes back through the microscope objective and the periscope and it is collected deflecting it toward a photodiode, in turn connected to an oscilloscope. This latter possibility allow for the detection of the optimal

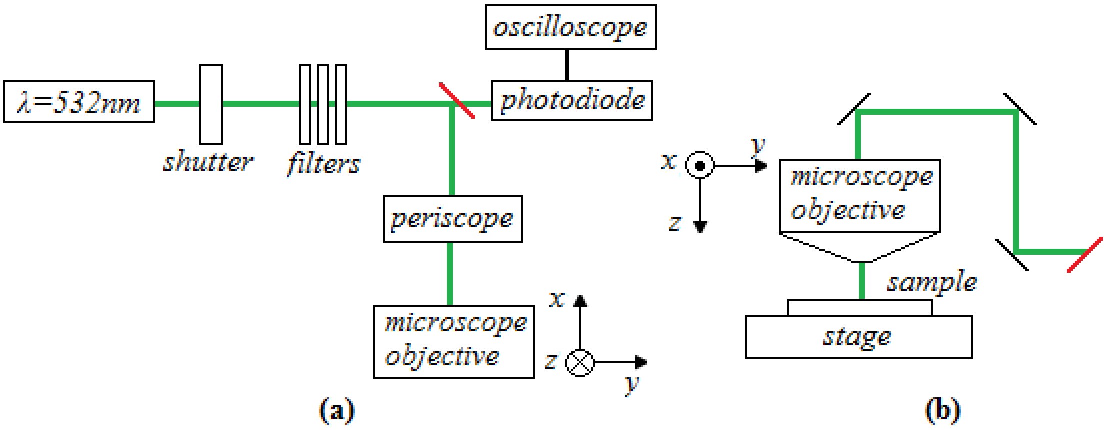

Figure 2.10: Description of the setup used to write the waveguides and the gratings. a) Bird's – eye view. b)Lateral view.

focusing at the sample surface, as when the beam is focused at the surface, the photodiode signal shows a maximum.

To create waveguides or gratings, the sample is placed on the stage with its *z* axis parallel to the beam polarization. The structures have to be created at the upper sample surface, so the beam has to be focused here. After that it is important to guarantee the horizontality of the crystal, so that, during the translation, the structures are created always at the same height. To make this, the beam is focused initially on a corner of the sample, and subsequently in the opposite one and if the oscilloscope indicates that the signal is maximal in both points for the same z-position of the microscope objective the sample is taken to be horizontal. If it is not the situation, the crystal has to be tilted and the microscope objective translated, till the horizontal condition is found. This operation damages optically the sample, therefore these two regions cannot be used to create the desired structures. Moreover, due to the gaussian nature of the beam, it is important to remember that structures are also written in depth, and not only at the surface.

As a consequence of how the sample is placed on the stage, the laser has to scan the surface moving parallel to *y* axis. In order to avoid the presence of systematic errors due to the rolling and pitching of the translation stages (which can lead to the presence of sub – harmonics in the written gratings) the lines are scanned moving always in the same direction. In addition to make thick optical barriers it is sufficient to separate lines with a distance of 1μm, because thanks to the dimension of about 1.5μm of the beam focus, this value allow to superimpose the lines and so to create larger barrier a region.

3 | OPTICAL TWO-STATE STIRAP IN SBN

The optical two-state STIRAP is studied using the setup presented in paragraph 2.3.4, by which waveguides are created and characterized. In this section the simulations of the phenomena and its experimental realization are presented.

3.1 Setup Optimization and Characterization

The first step to characterized the setup consists in the study of the accessible index variation when we illuminate the SBN with the control beam. As it was seen in paragraph 2.3.2, describing the waveguides formation, the maximal index contrast is the difference between the one of the dark and the illuminated zone and it depends on the external electric field E_0, the intensity of the control beam I(x) and the background illumination I_D.

In spite of the theoretical equation the information on the effective index contrast is obtained experimentally using the Mach-Zehnder interferometer placed in the setup as described in paragraph 2.3.4. Experimentally we count the number of fringe in the interferometric image, from the initial moment of the waveguide creation to the stationary situation, operation made possible thanks to the rather slow dynamics characterizing the photorefractive process in SBN. The number of fringes *m*, calculated using images as the one reported in Figure 3.1b, permits to know easily the index contrast Δn, using the equation:

$$\Delta\phi = \frac{2\pi}{\lambda}\Delta n\, d \tag{3.1}$$

where λ is the wavelength of the probe beam, d the crystal length and ΔΦ is the phase shift defined as ΔΦ = 2πm. It is also possible in this way to connect the gray level of the waveguide with its refraction index contrast, counting the variation fringes for different waveguides, each one characterized by a different color. This study is fundamental because, experimentally we have access to the gray level using the SLM, but for the simulation it is necessary to know the index contrast. With this study the calibration reported in Figure 3.2a is obtained, where it can be noticed that the effective refraction contrast is in the order of 10^{-4} and that images with a grey level superior than 75% or inferior than 50% cannot be used. In the first case because the SLM generates a constant changing in the refractive index, in the second one because the dynamic is too slow and an appreciable change in the index cannot be measured in a reasonable time.

From the information on Δn it is possible to know the phase mismatch between two waveguides using the equation:

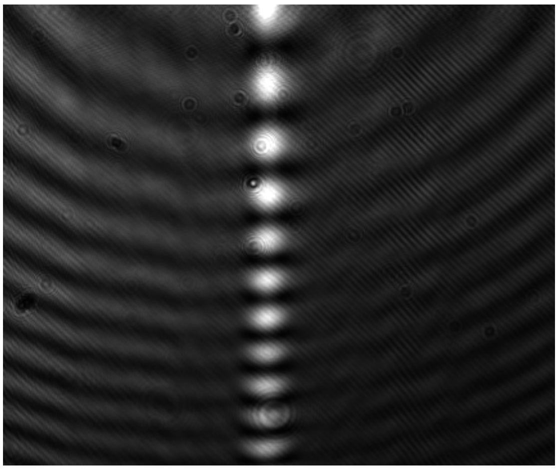

Figure 3.1: Interferometric image of a waveguide.

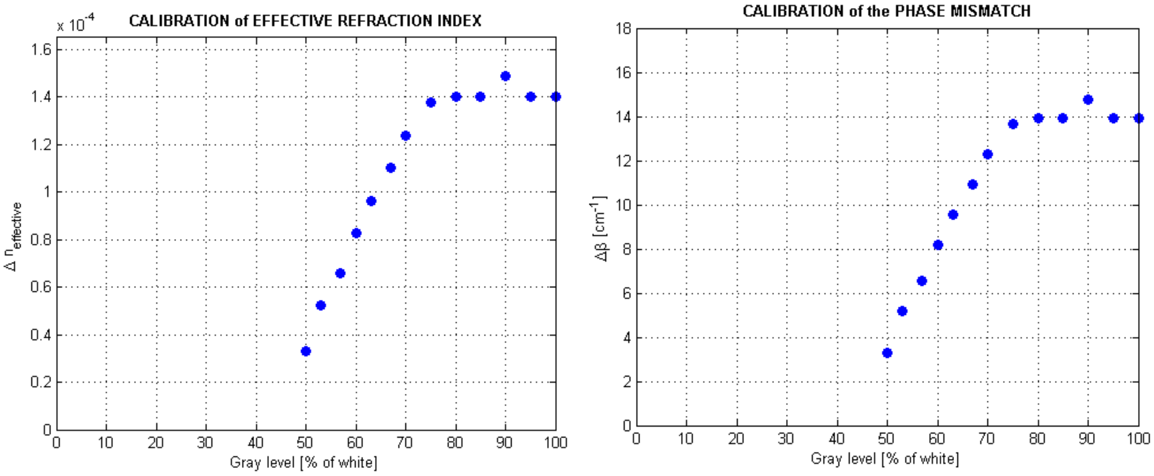

Figure 3.2: a) Calibration measures of the effective contrast of the refraction index as a function of the gray level apllied to the SLM image. b) Calibration measures of the phase mismatch as a function of the gray level.

$$\Delta\beta = k_0 \Delta n = \frac{2\pi}{\lambda} \Delta n \tag{3.2}$$

The corresponding calibration is reported in Figure 3.2b.

The external electric field E_0 applied to the crystal was set to 2.5kV/cm and the waveguide width is 7.2μm, because a precedent study has highlighted that these values are the optimal experimental conditions to obtain waveguide of good quality [8]. The power of the control laser was set to about 180mW as a result of preliminary studies. This allows to obtain the largest zone for which a changing in the gray level corresponds to a change in the effective index. With these parameters only the first propagation mode propagates in the waveguides.

To reproduce the gaussian variation of the phase mismatch in a gaussian variation of the index refraction it is important to know the dependence of the gray level in function of the Δβ between 50% and 75%. This information is extract from a fit made on Figure 3.2b obtaining the equation:

$$gray\ level = -0.0052\,\Delta\beta^3 + 0.16\,\Delta\beta^2 + 0.99\,\Delta\beta + 47 \tag{3.3}$$

3.2 Theoretical Modeling

The central part of the demonstration of the optical two-state STIRAP consists in the creation of images reporting the optimal waveguides configuration which has to be reproduce in the crystal. To make this, a set of programs in Matlab language reported in Annex A were developed, creating, from the initial shape of the two pulses Δβ and C, the desired image

The first step is to decide which pulse shape to take, because as seen in paragraph 0.01.1.2 there is not a privileged choice, although for simplicity a gaussian variation is normally considered. So a preliminary study on the pulses is made using *Program 1*. Considering that the light is initially coupled in only one waveguide, the coupled mode equation using the Hamiltonian (1.51) is numerically solved and the intensity of the end of the two waveguides is studied. The purpose of the two-state STIRAP is to achieve the 50% of the initial intensity exiting from each waveguides, for both the intuitive and the counterintuitive sequence. Pulses are modeled with the aim of reaching of this situation. During this first study it is important to take into account that that the maximal variation of Δβ and C are experimentally limited. For the first one, Figure 3.2b indicates that the maximal amplitude is about 10cm^{-1}, while for the second one the limitation derive from the minimal inter-guide distance that the SLM can reproduce in the crystal. As seen earlier this one is 1.2μm, so the amplitude of the coupling constant cannot be superior to the value corresponding of this minimal distance.
The study on the optimal theoretical configuration of pulses has also highlighted that the system exhibits the same behavior when the phase mismatch is positive or negative. Therefore so experimentally four configurations have to be tested: counterintuitive and intuitive sequence, each ones for negative and positive Δβ.

When the optimal theoretical configuration is found, *Program 2*, solving the equation of the propagation in a single waveguide and the coupling mode theory, described respectively in paragraph 161.2.1 and 1.2.2, translates the variation of pulse C in a variation of the inter-guide distance. To solve the model it is fundamental to utilize the real index refraction of the waveguide and not the effective one, so the Δn found with calibration measures is converted using *Program 3*. This one calculates the propagation in a single guide solving the transcendental equation for a theoretical index in the range 10^{-5} - $4{\cdot}10^{-4}$. The experimental value is predicted from the equation (1.31) and the result is shown in Figure 3.3: from this graph, with a fit, the two values are connected and the result equation is finally used in Program 2. It can be seen as the two indexes have a non-linear variation for small values around 10^{-5}, while for large values the mutual dependency is roughly linear. Overall the entire set of value is modeled with a polynomial of sixth order.
To demonstrate the optical two-state STIRAP two waveguides with different refractive index contrast are necessary, so the coupling constant $C_{1,2}$ and $C_{2,1}$ are not equals and, as seen in paragraph 1.2.4, their geometric average is used to solve the model. Fixing the inter-guide distance Program 2 permits also a study in the variation of the coupling constants as a function of Δβ, as shown in Figure 3.4. This graph is created using a gaussian variation of the phase mismatch having an amplitude of 1.0mm^{-1} and an inter-guide distance of 3μm: the geometric mean is about constant, and this demonstrate that the approximation used to solve the model is licit.

After having calculated the waveguide curvature, it possible to reproduce the phase mismatch variation in a corresponding gray level variation, using equation (3.3). These calculations are implemented in *Program 4*, and the final image with right dimensions, resolution and colors is produced to be experimentally tested. To create the image corresponding to a positive Δβ the two waveguides are placed in the figure so that the microscopy objective injects the light in the straight one. For the case of negative Δβ, the two waveguides are simply translated so that the microscopy objective couples the light entirely in the curved one, realizing the desiderate condition in a simpler way. Images are created with a black background while waveguides have a gray level changing between 50% and 75%, according to calibration measures. The theory does not prescript which waveguide has to have the fixed index and which the gaussian one, both configurations are expected to deliver the same result.

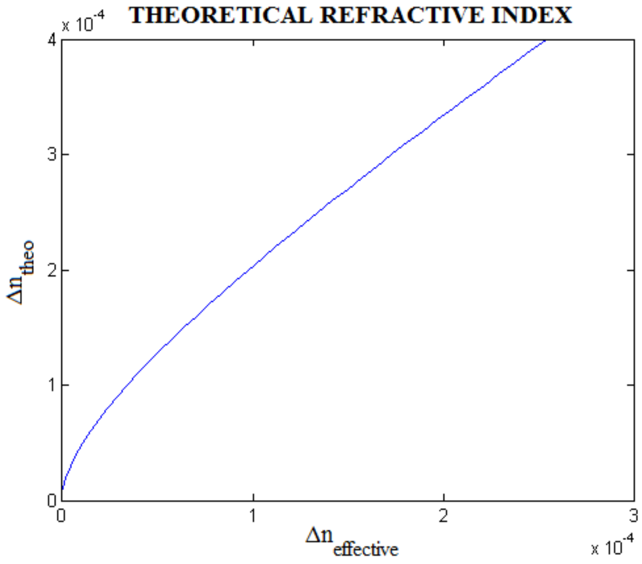

Figure 3.3: Prediction of the effective refraction index in function of the theoretical one in the range 10^{-5} - $4·10^{-4}$.

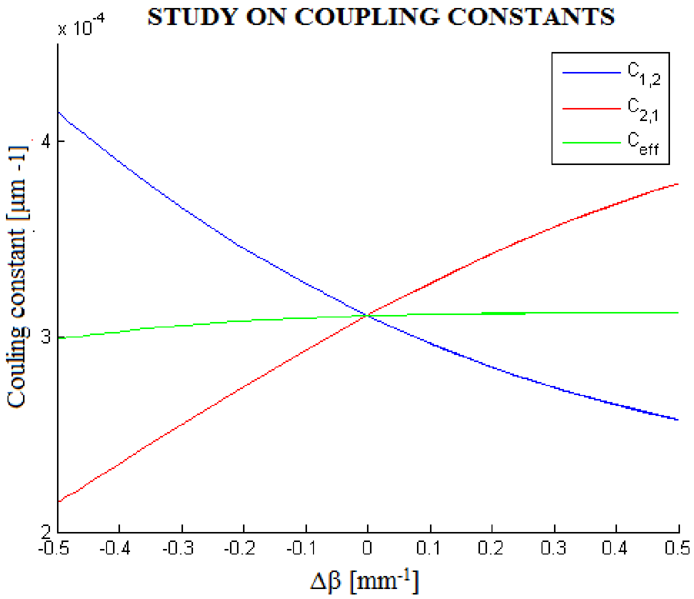

Figure 3.4: Variation of coupling constants $C_{1,2}$ and $C_{2,1}$ and its geometric mean C_{eff}, calculated using a waveguide with a fixed index of refraction and the other one with the gaussian contrast reported in Figure 3.5a. The inter-guide distance is fixed to 3µm.

3.3 Results and Discussion

The first set of measures utilizes gaussian pulses having respectively the form:

$$\Delta\beta(z) = \Delta\beta_0 \exp\left[-\left(\frac{z-z_1}{w}\right)^2\right] \tag{3.4}$$

$$C(z) = C_0 \exp\left[-\left(\frac{z-z_2}{w}\right)^2\right] \tag{3.5}$$

where $\Delta\beta_0$ and C_0 are the maximal amplitudes, z_i is the center of the gaussian and w is it's the half width at 1/e level.

After a preliminary test on possible pulses configurations, it was decided to center gaussian pulses respectively in z_1 = 7,6mm and z_2 = 15,2mm from the beginning of the crystal, equally spaced compared to the crystal border which are about 23mm, so that in this symmetric situation the change from the counterintuitive to the intuitive sequence consists only in a permuting of z_1 and z_2 in equations (3.4) and (3.5). The maximal value of the phase mismatch $\Delta\beta_0$ was set to 1.0mm^{-1} and C_0 = 0.42mm^{-1} . This choice is motivated by the fact that higher pulses allows to better respect the adiabatic condition. The gaussian width w is established as the value permitting to obtain in the simulation 50% of the initial intensity at the output of each waveguides. The resulting profiles of Δβ and C for the counterintuitive case are shown in Figure 3.5a while in Figure 3.5b the corresponding variation of the intensity along the propagation is reported. It can be recognized as these parameters allow to maintain the system in adiabatic condition because the intensity does not exhibit oscillations during the propagation. The intuitive sequence is reported in Figure 3.6. It can be seen that also in this case the system tends to the desired final configuration but initially the system is characterized by oscillations. In both cases the simulation do not reach exactly 50% of the initial population because of both the finite crystal length and the values describing pulses.
Figure 3.7 shows the counterintuitive case simulated using a negative phase mismatch and it can be noticed that the intensity profile is the same to the one for positive Δβ. The intuitive case exhibits the same behavior.

For each configurations the corresponding waveguide profile is reported in Figure 3.8. This one reproduces the gaussian variation of C considering that the other waveguide is straight and ideally placed at position zero on the ordinate axis. The typical distance are in the order of micrometers and in particular for this configuration the minimal distance between the two waveguides is about 2 μm while the maximum distance is about 20μm. Only two profiles are necessary, considering that the case with negative phase mismatch does not change the curvature.

Finally the images controlling the SLM are generated and an example is given in Figure 3.9, the one corresponding to the counterintuitive case. This one is created by fixing the gray level of the straight waveguide to 75% while the curbed guide is characterized by a gaussian longitudinal index variation, reproducing the variation of Δβ of Figure 3.5a. As explained in the precedent paragraph from the theoretical point of view it is indifferent where the gaussian variation is placed but unfortunately this correspondence is not confirmed experimentally. In initial experiments the index variation was placed in the straight waveguide and with this configuration a confirmation of the two-state STIRAP was obtained, but only for the positive gaussian variation of the phase mismatch, indication that experimentally some kind of asymmetry is introduced. On the contrary, if the indexes of refractions variations are placed as in Figure 3.8

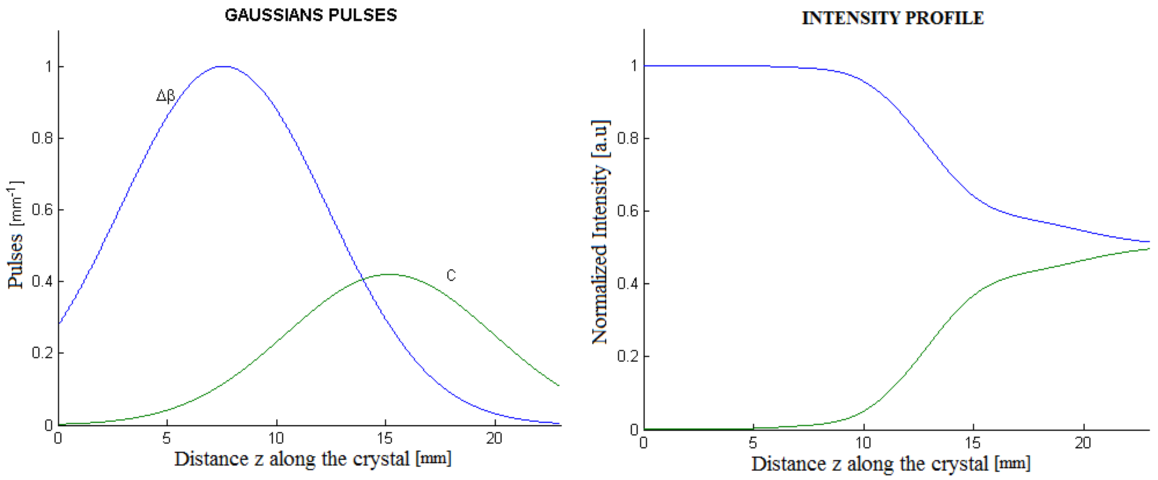

Figure 3.5 a) Counterintuitive spatial pulses sequence. b) Simulation of the light evolution intensity along the propagation in the crystal using the counterintuitive pulse sequence.

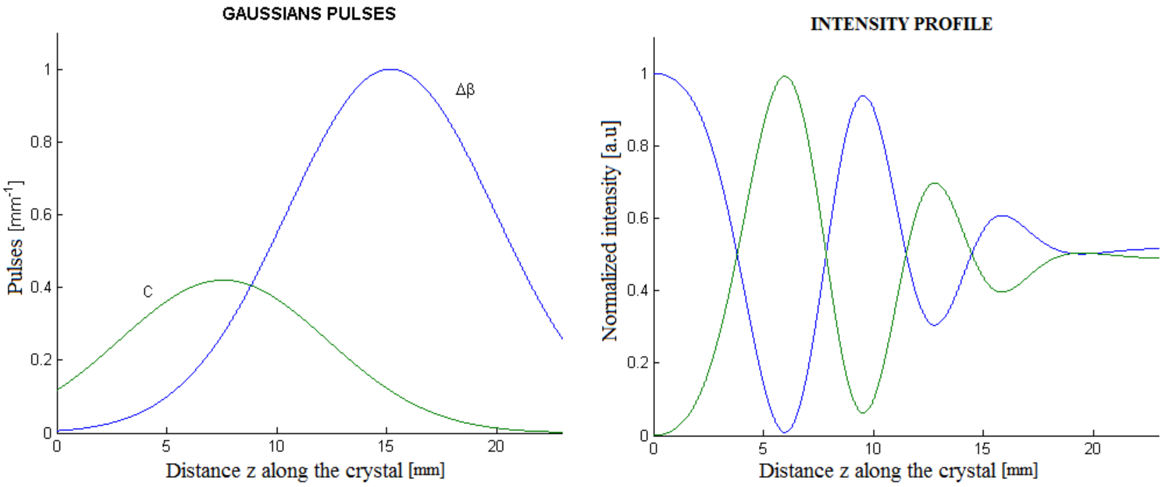

Figure 3.6: a) Intuitive spatial pulses sequence. b) Simulation of the light evolution intensity along the propagation in the crystal using the intuitive pulse sequence.

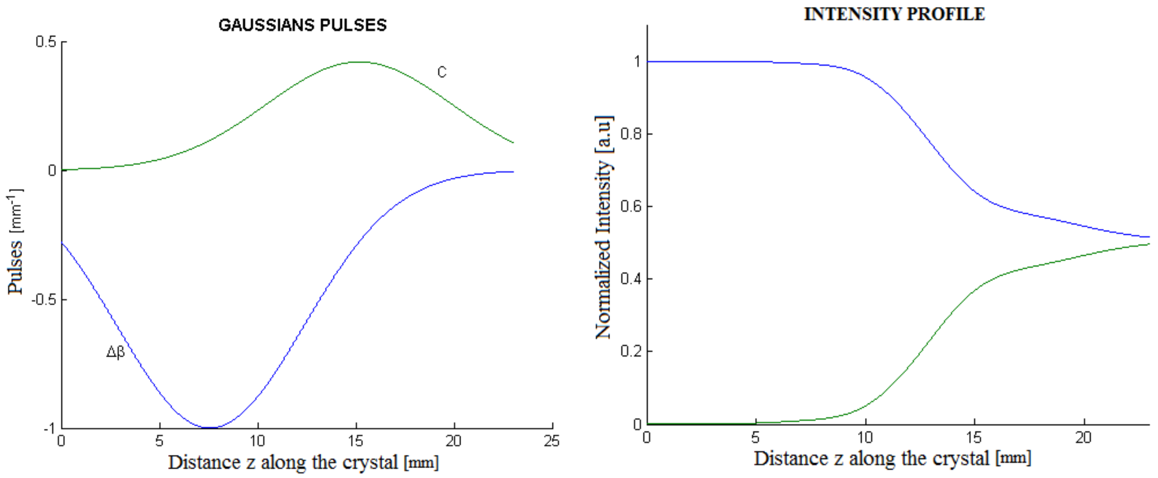

Figure 3.7: Counterintuitive pulses sequence using a negative Δβ b) Simulation of the light evolution intensity using the counterintuitive pulse sequence with a negative Δβ.

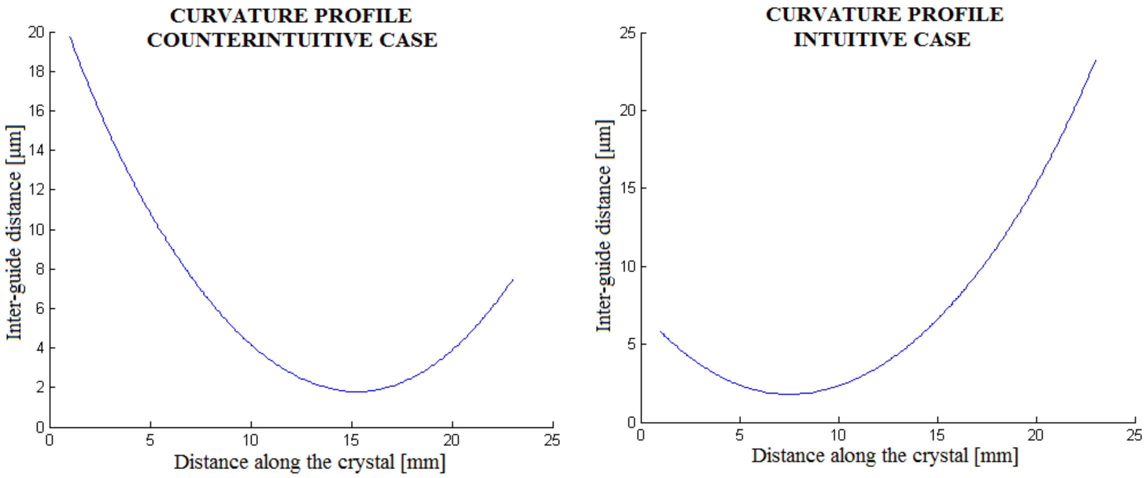

Figure 3.8: a) Inter-guide distance calculated for the counterintuitive pulses sequence. b) Inter-guide distance calculated for the intuitive pulses sequence.

Figure 3.9: Image used to reproduce with the SLM in the SBN the desired pulse configuration. The present structure corresponds to the one for the counterintuitive case is reported.

there is a light passage between the waveguides for all configurations, counterintuitive intuitive and with positive and negative Δβ.

Images are more sensible to small variation in Δβ instead of C because of the transformation from micrometers of the Figure 3.8 into pixels in Figure 3.9. Effectively, known that 1.2µm corresponds to 1pixel, variation of the inter-guide distance inferior to this step are not detected by the setup.

Experimentally the light propagation is studied at the end of the crystal taking videos with the CCD camera, and it is possible to see that, after an initial transient time of stabilization which is about 20 seconds, the light initially injected in one single waveguide is coupled into both guides. Video shows that for all the configuration are 50% of the initial light is achieved, as predicted by simulation, but the phenomena is not sufficiently stable, because light oscillation between waveguides are still present after the quasi stationary state. At the present we are able to highlight the phenomena for all four configurations. A consecutive important work will have to be made to modify the present experimental parameters in order to stabilize further the process.

In any case it is possible to make a preliminary analyze to have important information on the intensity, profile and position of the waveguides. From videos of each configuration, images, as the one shown in Figure 3.10 are extracted and the analysis is made by studying the corresponding profiles along the x axis for a fixed y. The latter, are superimposed with the corresponding gaussian profile (Figure 3.11). To connected the x axis expressed in pixel to a physical dimension, we remember from the setup description that 1 pixel_{CCD} is equal to $0.73\mu m_{SBN}$. The resulted profile are reported in Figure 3.11 where it can be seen that for all the configurations it is possible to achieve about the same intensity in two waveguides at the end of the crystal. The two gaussians in the counterintuitive case with Δβ>0 are separated by 18.2µm and with Δβ<0 by 16.8µm. Remembering that each waveguide has a width of 7.2µm the respective

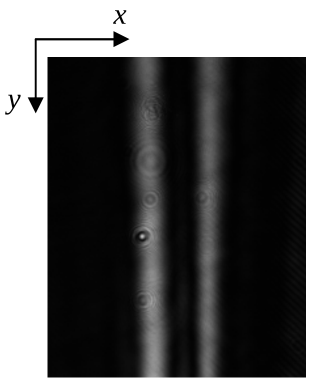

Figure 3.10: Image of two waveguides extract from the video studying the light evolution. This kind of image is used to obtain the profiles reported in the following figure.

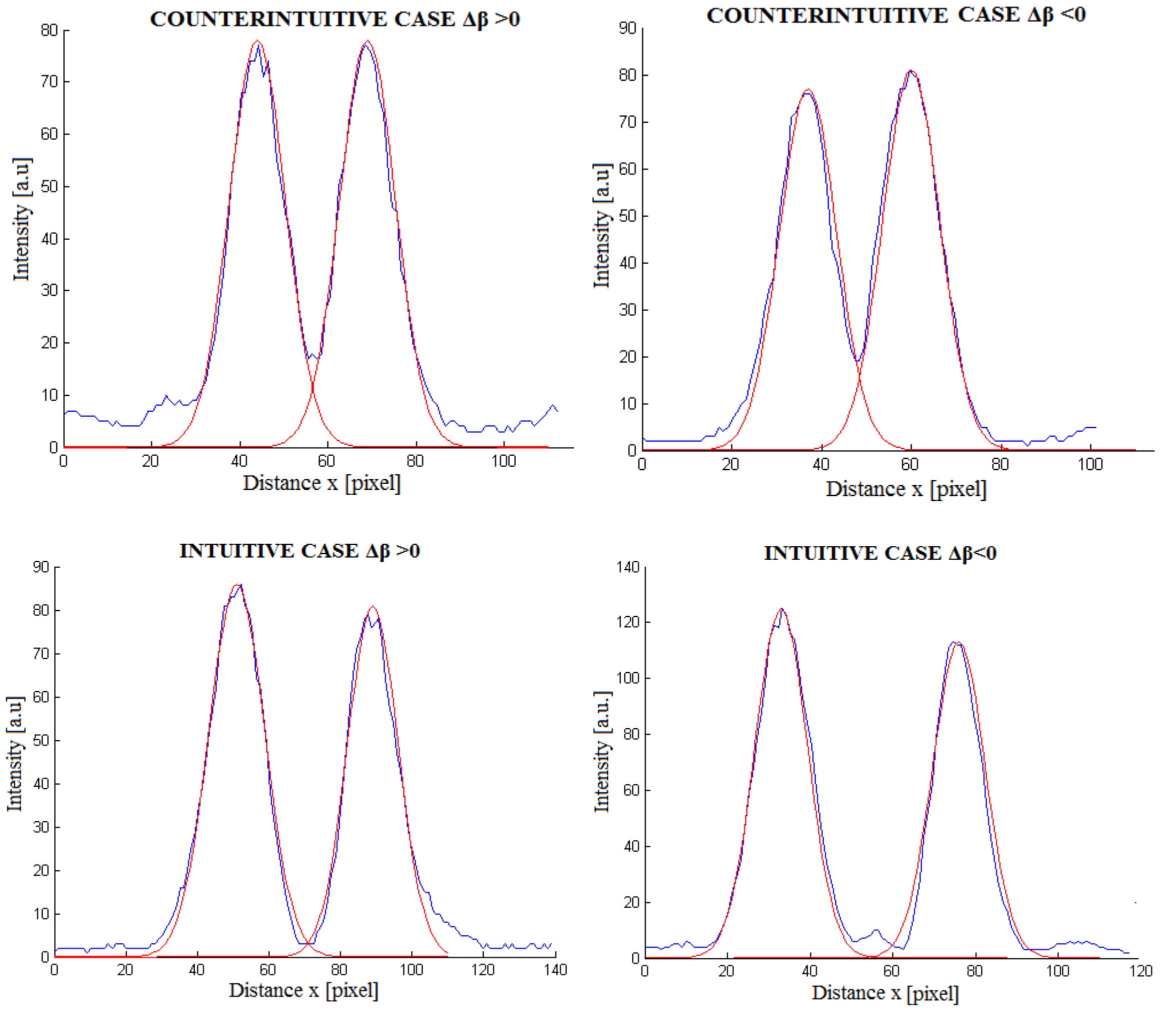

Figure 3.11: Output intensity profile along x of the two waveguides extracted from images such as the previous one. Each pick is superimposed with a gaussian for the analysis of intensity and position.

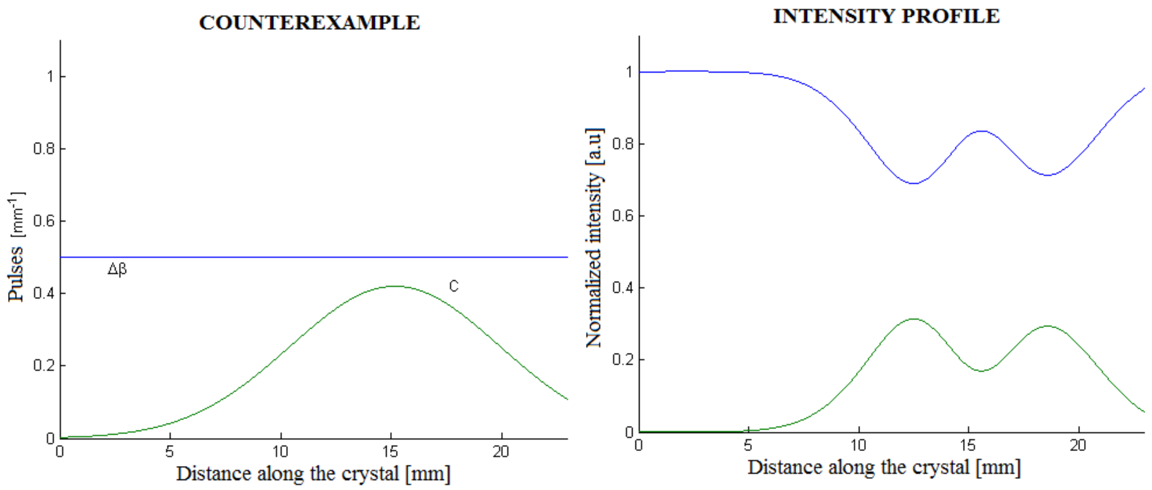

Figure 3.12: a) Pulses configuration used for test a counterexample of the two-state STIRAP. b) Intensity variation along the crystal for the counterexample configuration.

inter-guide distances are 11µm and 9.6µm: considering that two transformations between pixel and µm are made these value are consistent with those expected from the theoretical profile of Figure 3.8a. In the intuitive case for $\Delta\beta > 0$ the separation is 27.7µm while for $\Delta\beta < 0$ is 31.4µm, corresponding to an inter-guide separation of 20.5µm and 24.2µm, respectively.

To validate the model it is also necessary to find counterexamples of the two-state STIRAP just demonstrated. The aim is to confirm that the 50% splitting is achieved only if pulses respect all the theoretical model constraints described in paragraph 0.01.1.2. For this purpose a pulse sequence expected to prevent the passage of the light between the two waveguides was analyzed. The sequence reported in Figure 3.12a was selected, to demonstrate that it is necessary to have a gaussian variation of the longitudinal propagation constant. Δβ. For the counterexample Δβ was set constant to the value of 0.5mm^{-1}, while C is not changed with respect to the precedents tests. The corresponding intensity simulation along the propagation shown in Figure 3.12b. The light injected in one waveguide, after an initial oscillation, remains almost all confined in the same waveguide.
With this configuration the corresponding image is formed by two waveguides, one straight and the other one curbed, having the same curvature calculated earlier, but this time both with a fixed index. I particular the straight one has a gray level of 75% while the other one is calculated using equation (3.3) for $\Delta\beta$=0.5mm^{-1}. In this case the video shows that, after a initial transient time characterized by oscillations, the light remains confined in the waveguide where it is injected, confirming the theoretical expectations.

Another type of pulses variation was also tested, so that the quantum phenomena would be independent from the their analytical form. In particular super-gaussian of fourth order were used, reported in Figure 3.13a, and following the equation:

$$\Delta\beta(z) = \Delta\beta_0 \exp\left[-\left(\frac{z-z_1}{w}\right)^4\right] \tag{3.6}$$

$$C(z) = C_0 \exp\left[-\left(\frac{z-z_2}{w}\right)^4\right] \tag{3.7}$$

where $\Delta\beta_0$ and C_0 are the maximal amplitude, z_i is the center of the super-gaussian and w is its half width at 1/e level.
In this case, the intensity in the two waveguides evolves toward the 50% splitting for smaller amplitudes $\Delta\beta_0$ and C_0 for the gaussian profile. In particular $\Delta\beta_0$ is set equal to 0,6mm^{-1} and C_0 =

0,3mm^{-1}. Consequently *w* was fix to 6,2mm, that is z_1 and z_2 are the same as in the precedent configuration, equals to 7,6mm and 15,2mm, respectively. This configuration allows anyway to maintain the system in adiabatic condition, visible from the Figure 3.13b because of the non presence of oscillations.

The corresponding inter-guide distance is shown in Figure 3.14, where it can be seen as the maximal is about 120µm. The phase mismatch is reproduced always using equation (3.3) and the corresponding figure is experimentally tested. Unfortunately the curvature necessaries to reproduce C is too large so that the light can be here confine and, in spite of the simulation, experimentally this configuration cannot be used to test the two-state STIRAP.

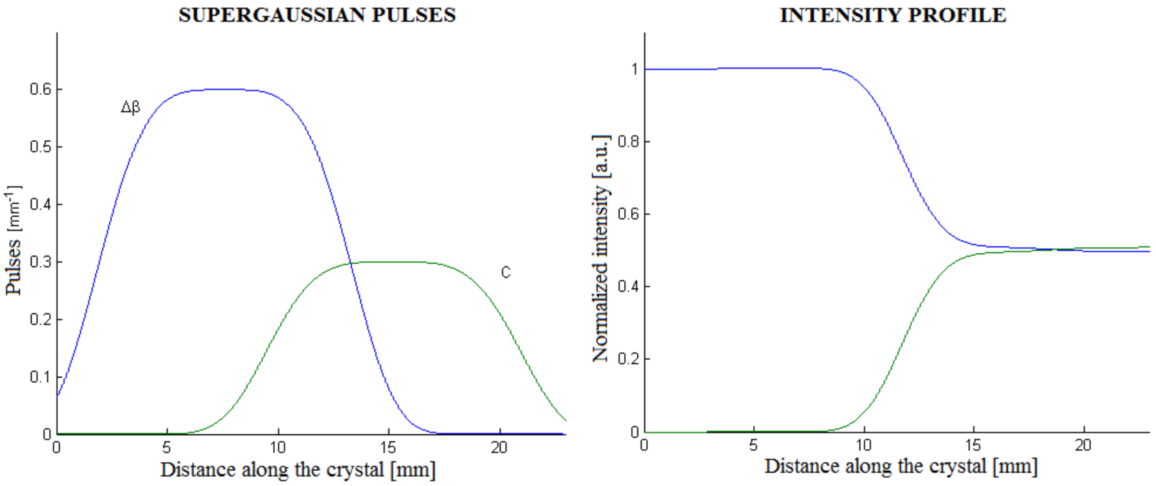

Figure 3.13: a) Counterintuitive supergaussian pulses sequence. b) Simulation of the light evolution intensity along the propagation in the crystal using the counterintuitive supergaussian pulse sequence.

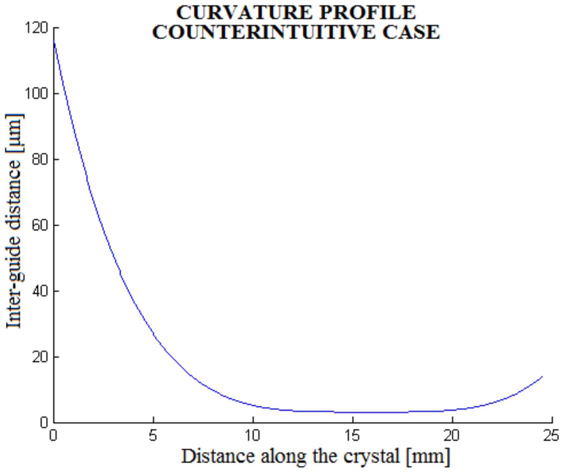

Figure 3.14: Inter-guide distance calculated for the counterintuitive supergaussian pulses sequence.

4 | DIRECT WRITING OF FIBONACCI WAVEGUIDES ARRAY IN Ti:Fe:LN

Using the setup described in paragraph 2.4.4, a series of waveguide was produced in our Fe:LN sample. The resulting system was studied both in near field to characterize the light – confinement properties of the written optical barriers and in far-field using an optical diffractometer. The first approach exploited the setup presented in paragraph 4.1, while the second one will be described in the following. This study is the basis to a further develop of the optical system able to reproduce optically the quasicrystals.

4.1 Waveguide characterization

The first step of our investigation consisted in determining what are the best process conditions are in order to obtain a waveguide and what the limits of the writing technique are. The first experimental waveguides set was realized in the bulk of a Fe:LN sample described in preceding paragraph (sample code:151.15.2), following the schema shown in Figure 4.1and in the Table 4.1. In this case the field is confined in only one dimension, so that the resulting waveguide have a configuration somehow similar to those created with the lateral illumination technique. A set of waveguides was therefore realized by changing in a systematic fashion the writing speed between 500 and 1000 µm/s, the barriers width between 30 and 5 µm and the waveguide width between 25 and 50 µm (see table 4.1).

The setup used for the characterization waveguides in near field is shown in Figure 4.2. The source is a fiber-coupled laser diode with a wavelength of 670 nm, a power of some hundreds of microwatts and controlled by changing the injected current. The beam exiting from the fiber is collimated by a convex-plane lens with a focal length of 3cm, and injected in the microscope objective1. The sample is collocated in the focus of the probe beam, so that the probe signal is injected inside the waveguide structures. A second microscope objective with 50x magnification placed at the output surface, collects the light exiting from the waveguide. A CCD system connected to a computer was connected to the output objective, to collect some image of the beam exiting from the surface

Two type of focusing objectives were used during the analysis, one with an enlargement of 4x and the other one with an enlargement of 60x. From the equations describing the transmission of a gaussian beam through a focusing components, it is possible to estimate the diameter of the laser exiting of these two lens. In particular the focused spot for the first one has a diameter of about 25µm, while for the other one of about 4µm.

To study this first set of waveguides, the microscope objective1 with the enlargement of 4x was used, because its waist was better suited to the waveguide dimensions.

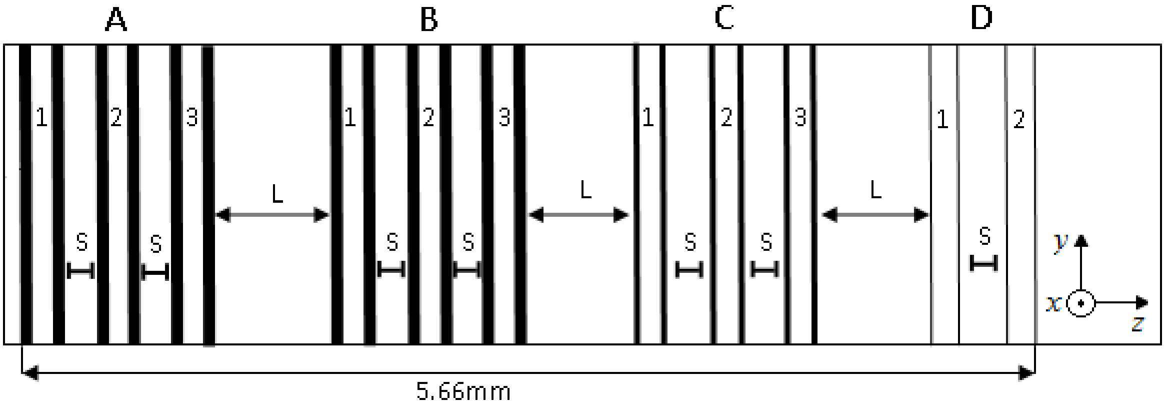

Figure 4.1: Description of the first waveguides set wrote in the sample 151.15.2. the reference system indicated the crystallographic axis of lithium niobate.

	A			B			C			D	
	1	2	3	1	2	3	1	2	3	1	2
Writing velocity [μm/s]	500			1000			500			500	
Barriers width [μm]	30			30			15			10	5
Waveguide width [μm]	50	35	25	50	35	25	50	35	25	50	
L [μm]	1000										
S [μm]	250										

Table 4.1

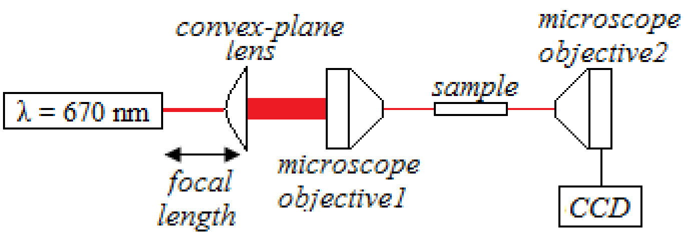

Figure 4.2: Description of the setup used to study waveguides.

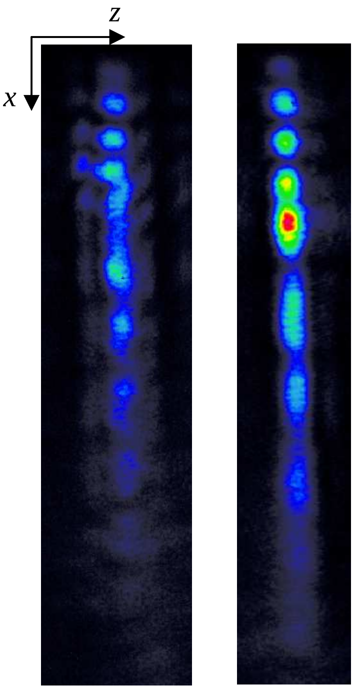

Figure 4.3: a) Image of A1 waveguide, which presents a multi-mode propagation of light. b) Image of A2 waveguide, characterized by a mono-mode propagation. The x axis is along sample surface, while y along the volume, where the extension of a guide is about 100μm.

The preliminary characterization is made with the CCD camera, which permits to take images of waveguides, as shown in Figure 4.3, where A1 and A2 guides are presented. This system allows to easily evidence a waveguide and to distinguish, perpendicularly to the beam propagation, i.e. along the z axis, its multi-mode (Figure 4.3a) or a mono-mode nature (Figure 4.3b). It is also possible to evaluate its extension in the volume of the sample, i.e. along x axis, which is about 100μm and to notice that the maximum of the guiding is near the surface. In addition in this direction, figures show the presence of fringes, owed to internal reflections at the surface.

The second characterization is made studying guides profiles along z axis, i.e. by comparing the measured near field images along the depth direction.

Initially the influence of optical barriers writing velocity is carried out and, as example, profiles of guides A2 and B2 are reported in Figure 4.4a. These ones were made with the same width (35 nm) and barriers dimension (30μm), but the first one was written with a velocities stage translation of 500μm/s, while the second one with 1000μm/s. These two values were chosen after a preliminary study on gratings, as they permit to obtain a suitable compromise between the time necessary to complete the writing of the entire sample and the magnitude of index refraction variation, for the power of 17 mW.

It can be noticed as A2 allows for a better confining of the light: therefore it is preferable to write the barriers with a velocity not larger than 500μm/s. This result, as seen in paragraph 2.4.2, has also a theoretical motivation, because a smaller velocity aloe to reach the maximal space charge electric field, creating a large refractive index contrast compared to the bulk value.

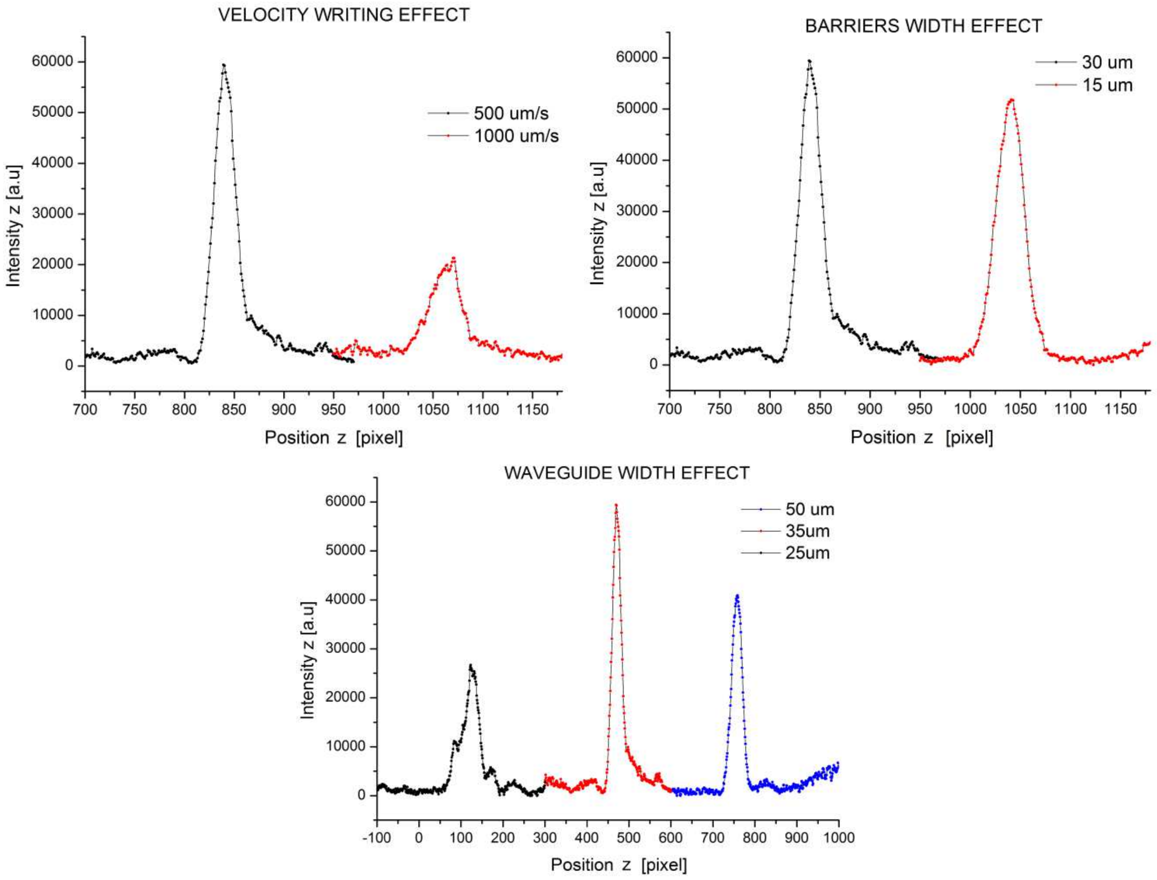

Figure 4.4: Profiles of intensity of confined light, projected along x direction. a) Profile of A2 (black) and B2 (red). b) Profile of A2 (black) and C2 (red). c) Profiles of A1 (black), A2 (red) and A3 (blue).

The influence of barriers width is also examined and, as example, the profiles of guides A2 and C2 are reported in Figure 4.4b. These one were made with the same writing velocity (500µm/s) and width (35nm) but the first one has two barriers of 30µm, while the second one of 15µm. In this case the difference of confined light intensity is about 1%, so it is not necessary to make wider barriers to obtain a suitable confining.

Finally guides width is taken into account and, as example, the profiles of group A are shown in Figure 4.4c. These guides were made with the same barriers dimension (30µm) and writing velocities (500µm/s), but with different widths. The figure shows that only guides with dimensions inferior to 35µm have mono-mode propagation of light.

The second experimental waveguide set was made again in the sample 151.15.2, after having canceled the preceding structures, but this time in the titanium guide, following the schema shown in Figure 4.5 and in the Table 4.1. In this case we obtained waveguides which are *hybrid*, because the confinement is achieved in two different ways: in one direction it is possible thanks to the photorefractive optical barriers while in the other one thanks to the presence of the titanium waveguide.

In this case a microscope objective1 with an enlargement of 60x was used, This is a necessary compromise because the hybrid waveguides have a guiding region with a very different size along the horizontal (~20 µm) and vertical (~2 µm), so that it is necessary to have a beam focus waist with a dimension comparable to the one of the titanium waveguide.

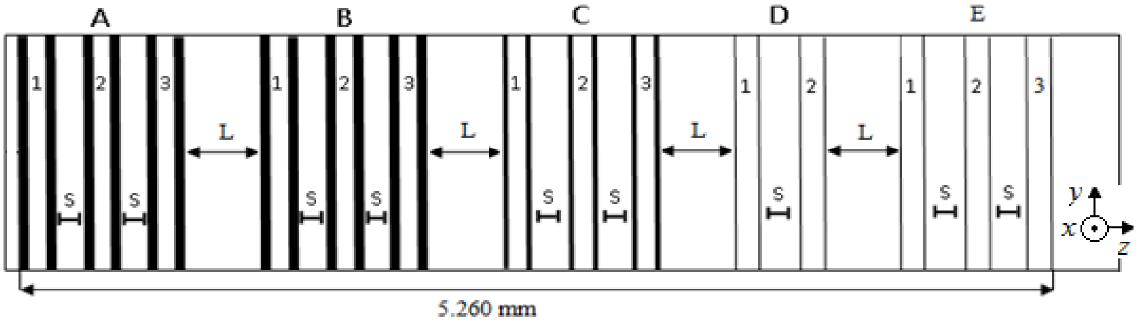

Figure 4.5: Description of the first waveguides set wrote in the sample 151.15.2.

	A			*B*			*C*			*D*		*E*		
	1	*2*	*3*	*1*	*2*	*3*	*1*	*2*	*3*	*1*	*2*	*1*	*2*	*3*
Writing velocity [μm/s]	500			1000			500			500		500		
Barriers width [μm]	30			30			15			10	5	1		
Waveguide width [μm]	50	35	25	50	35	25	50	35	25	50	50	50	35	25
L [μm]	500														
S [μm]	250														

Table 4.2

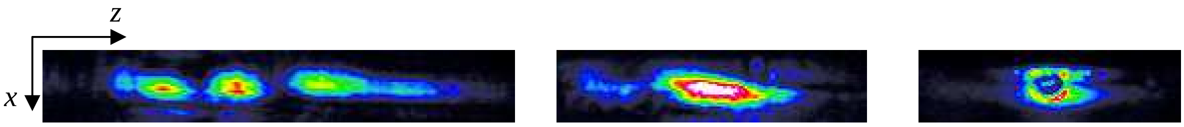

Figure 4.6: Images of group A, written in titanium waveguide. a) A1 guide, characterized by a multi-mode propagation of light. b) A2 guide, where the propagation is mono-mode. c) A3 guide, with a mono-mode propagation, in which a defect owed to the crystal is present.

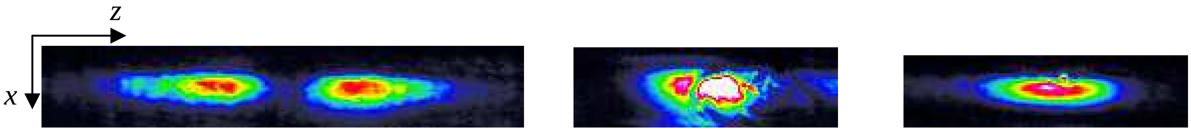

Figure 4.7: Images of group C, wrote in titanium waveguide. a) C1 guide, characterized by a multi-mode propagation of light. b) C2 guide, where the propagation is mono-mode, but a defect owed to the crystal is presented. c) C3 guide, with a mono-mode propagation.

Figure 4.8: Images of group D, wrote in titanium waveguide. a) D1 guide, created in a crystal defect. b) D2 guide, where the propagation is mono-mode, and where a defect owed to the crystal is present.

In fact, images had shown the presence of light leakages in titanium waveguide from the photorefractive optical barriers, caused by different values of index refraction variation along *x* and *y* axis. Indeed, being $\Delta n_{Ti} >> \Delta n_{barriers}$, a different numerical aperture of the beam along *z* and *x*, i.e. an elliptic beam, would be required to have the optimal coupling, while the real one is symmetric. To solve this problem it would be necessary to change the set up described in Figure 4.1, inserting a cylindrical lens after the microscope objective1 to make the beam elliptic, or to change the variation of index refraction modifying the diffusion parameters of the titanium.

The first characterization is made with the CCD camera, as shown in Figure 4.6, 4.7 and 4.8 where the group A, C and D are presented. Observing photos of A3, C2, D1 and D2, it can be noticed as this way to create waveguides is more sensible to crystal imperfection, and because of this reason D1 guide is excluded from the analysis. It was impossible to observe a guided mode in the group E, made with barriers of 1μm, so it is possible to conclude that waveguides created with a beam power of 17mW and a writing velocity of 500μm/s cannot confine the light, if the barriers are created with a single line.

The second characterization is made projected along *x* and *y* the profiles of confined light. In particular along *x*, as reported in Figure 4.9 which show the behavior of A1 as example, it can be noted how the titanium waveguide permits to confine entirely the light along this direction.

Profiles obtained along *z* are reported in Figure 4.10 and they are all normalized to one, in order to make clearer the comparison on the shape of the propagation modes. It can be seen that guides with a width of 50μm are always multi-modes, and to have a mono-mode propagation it is necessary to have a width inferior to 35μm, so that it is nearly irrelevant to create barriers of 30μm or 15μm, because the trend of modes is the same, if the writing velocity is 500μm/s. This consideration changes if the width of barriers is reduced up to 5μm, because they confines less the light and the propagation becomes mono-mode.

With this technique it is possible to reproduce what it was made with the lateral illumination technique but with some limitations, as for example the minimum distance than can be achieved between waveguides, which cannot be made smaller than 5 microns for the explored range of experimental conditions.

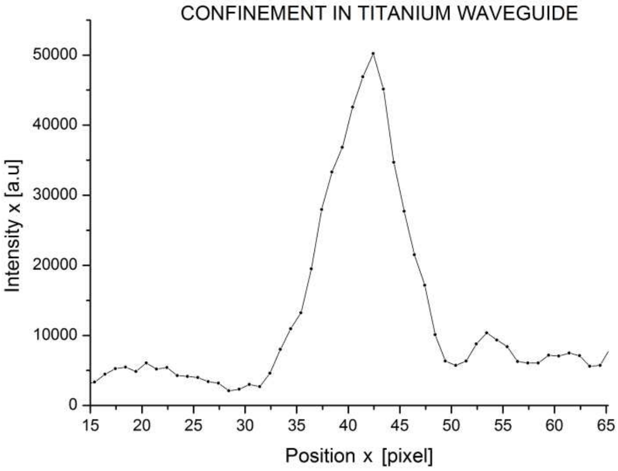

Figure 4.9: Intensity profiles of confined light, projected along *y* direction.

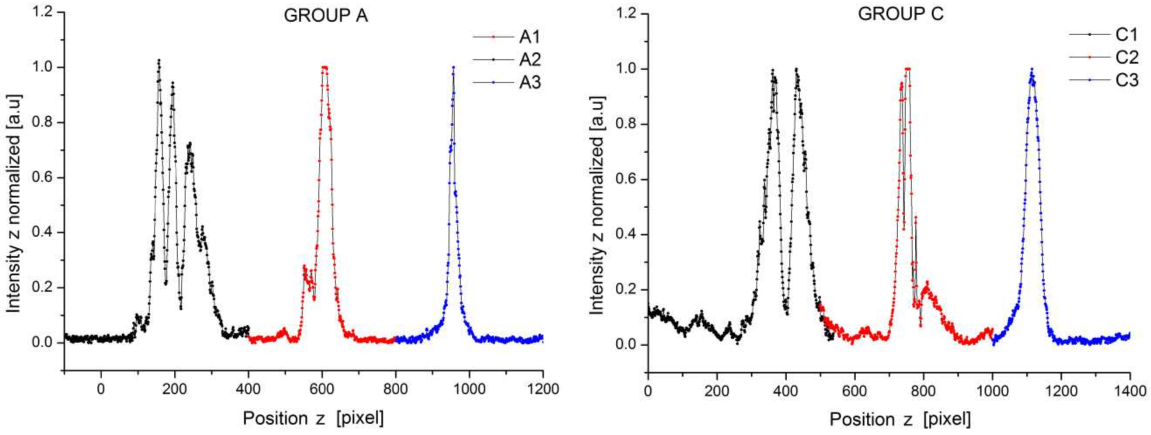

Figure 4.10: : Intensity profiles of confined light, projected along z direction. a) Profiles of group A: A2 (black) which shows a multi-mode propagation while A2 (red) and A3 (blue) a mono-mode. b) Profile of group C: C1 (black) characterized by multi-mode propagation, while C2 (red) and C3 (blue) by a mono-mode.

4.2 Gratings characterization

4.2.1 Description of the setup

The gratings characterization is made through the study of their diffractions pattern in the reciprocal space, obtained using the setup shown in Figure 4.11 [48].

The source laser is a He-Ne, having a wavelength of 632.8 nm and a power of 5mW. The beam is initially transmitted through a chopper, whose frequency is 360 Hz, a vertical polarizer and an attenuator. After that the laser passes through abeam expander, collimating it, and an iris, selecting only its central part. The aperture of the latter permits to define the illuminated area on the sample the spot size, so that the beam has the appropriate dimension to cover the grating surface. The sample is placed on a rotational stage, with its *y* axis parallel to the rotational axis. This stage, performing a ω scan, has a step resolution of 0.005deg; the sample position with respect to the rotation axis can be set and it is placed on a translation stage, so that the sample surface contains the goniometer axis. The detector is a Si PIN diode is mounted on a second goniometer having a minimum step of 0.005deg and performing the so-called θ scan. As the diffraction pattern has to be obtained in the far field, a spherical lens is mounted on the detector arm, with a 100 μm slit in its focal point. Using this configuration, the photodetector can scan along the true far – field region, i.e. associating to a given propagation direction the measured signal. The photodetector is connected to a lock-in which uses the chopper signal as reference. In this way a good dynamic of seven orders of magnitudes is obtained. The diffracted intensity is finally recorded and stored on a PC.

The focused spotsize after the lens has a diameter which is inversely proportional to the diameter of the probe beam 1/D, so it is important to verify that it can entirely enter in the slit, in order to avoid loss of intensity and/or resolution. This is verified by doing a θ-scan of the primary beam, for different iris apertures. The largest aperture possible is of 5mm, because this is the limit value

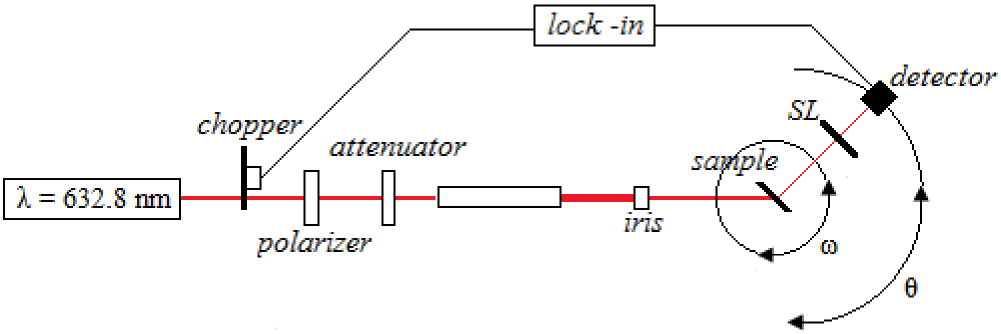

Figure 4.11: Description of the setup used for gratings characterization.

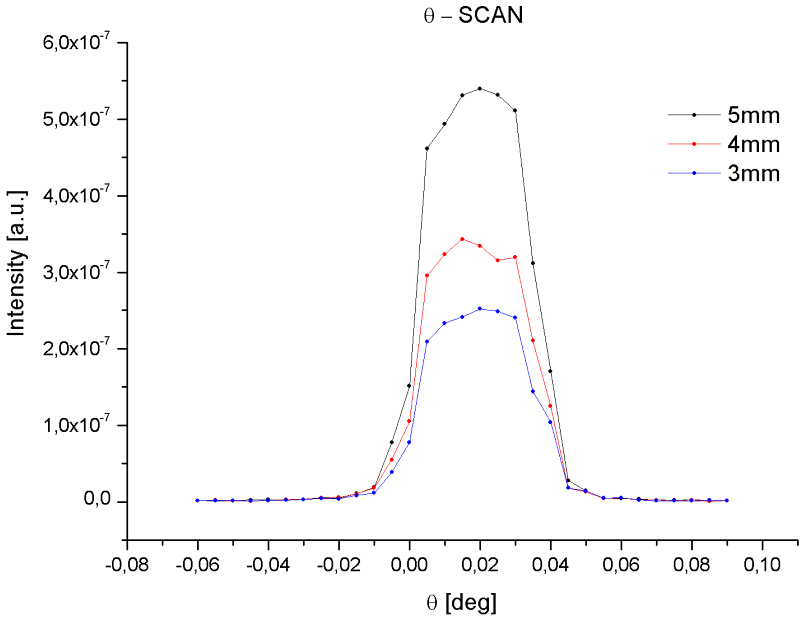

Figure 4.12:

to cover about entirely the grating surface and therefore apertures of 4mm and 3 mm were tested, as shown in Figure 4.12 If the iris aperture is 3mm, which creates the largest spot size after the lens, the maximum of the intensity is flat (Figure 4.12), meaning that the focused size is still able to pass the 100 μm slit. This implies that the angular resolution of the apparatus is determined by the split size and not by the lens. In the following the largest iris aperture of 5mm can be used, because guaranteeing the major intensity.

The setup just described allows to obtain the diffraction pattern I(**k**) in the reciprocal space considering the geometry shown in Figure 4.13. In this configuration ω and θ become respectively the incident angle of the primary beam with respect to the sample normal, and the angle between the primary beam and the diffracted one. Let $\mathbf{K}_0$ being the incident momentum, $\mathbf{K}_S$ the scattered one: for elastic scattering $\mathbf{k} = \mathbf{K}_S - \mathbf{K}_0$ is the exchanged momentum. In this configuration the projection along x and z of **k** becomes:

$$k_x = k[\sin\omega + \sin(\theta - \omega)] \qquad (4.2\text{ a})$$

$$k_z = k[\cos\omega + \cos(\theta - \omega)] \qquad (4.1\text{ b})$$

so it is clear that by performing a ω – θ scan according to a suitable pattern provides information in the reciprocal space.

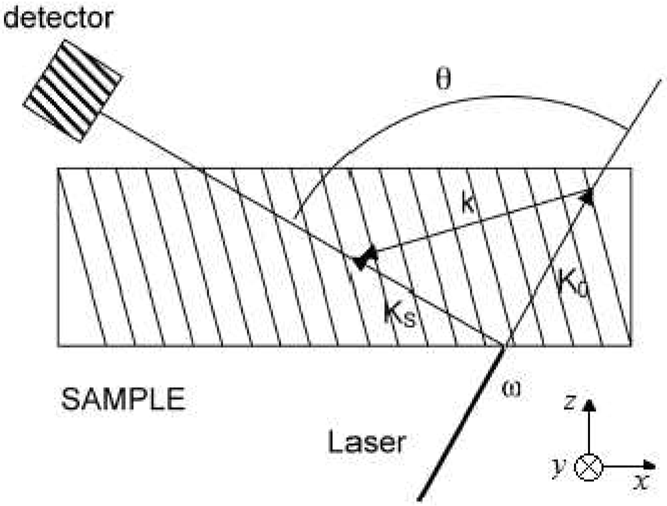

Figure 4.13: Description of the geometry used to convert the direct space in the reciprocal one [48].

4.2.2 Periodic and Fibonacci diffraction gratings

With the setup described in the previous section, three different gratings, written on the titanium waveguide of sample 151.14, were studied, two of them aperiodic and one periodic, as shown in Figure 4.14 and whose characteristics are reported in Table 4.3

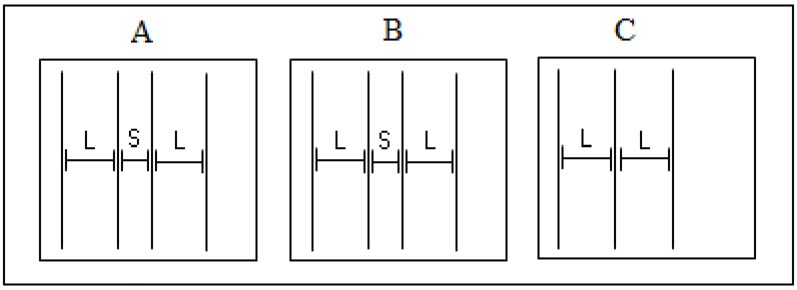

Figure 4.14: Description of the sample 151.14. A and B are aperiodic Fibonacci gratings while C is periodic.

	A	B	C
Long (L) [μm]	23	23	23
Short (S) [μm]	17	15	/
Writing velocity [μm/s]	500	500	500
Lines number	300	300	300

Table 4.3

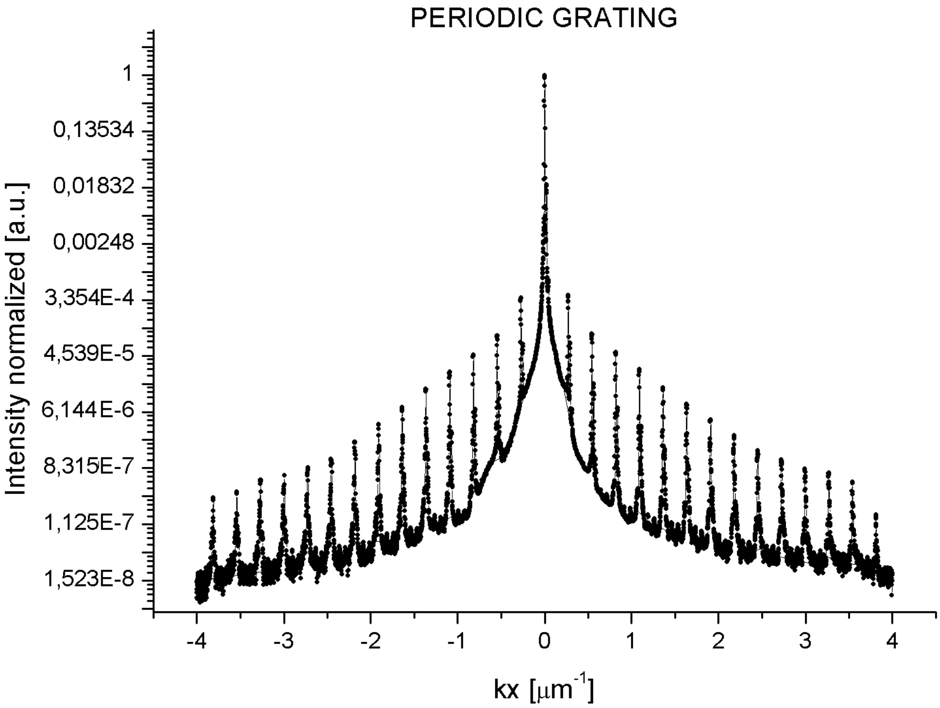

Figure 4.15: Diffraction pattern of periodic grating. The intensity is reported in logarithmic scale.

The periodic grating (C) permits to make a complementary study on the writing technique explained in paragraph 2.4.4, to analyze the characteristics of the single line creating the cladding of the waveguides, and also validate the results of the aperiodic gratings.

They are studied is far-field using the optical diffractometer described above and the corresponding diffraction pattern is presented in Figure 4.15, where and it can be seen that diffraction peaks are equally spaced, as expected.

In particular, the theoretical fundamental period Q of the pattern in the reciprocal space is defined as:

$$Q = \frac{2\pi}{L} \tag{4.2}$$

where L is the grating spacing, so the expected value for this particular grating is 0.273μm^{-1}. Consequently of this formula the position of each peak in this space is situated in $k_x = nQ$, with n an integer number.

To verify if the theoretical Q is in accordance with the experimental one, peaks position has been plotted in function of its order. The corresponding graph is shown in Figure 4.16 and a linear interpolation of the experimental data gives the parameters:

$$Q_{exp} = (0.27247 \pm 0.00005)\ \mu m^{-1}$$
$$\text{intercept} = (-0.0007 \pm 0.0004)\ \mu m^{-1}$$

in excellent agreement with the nominal value.

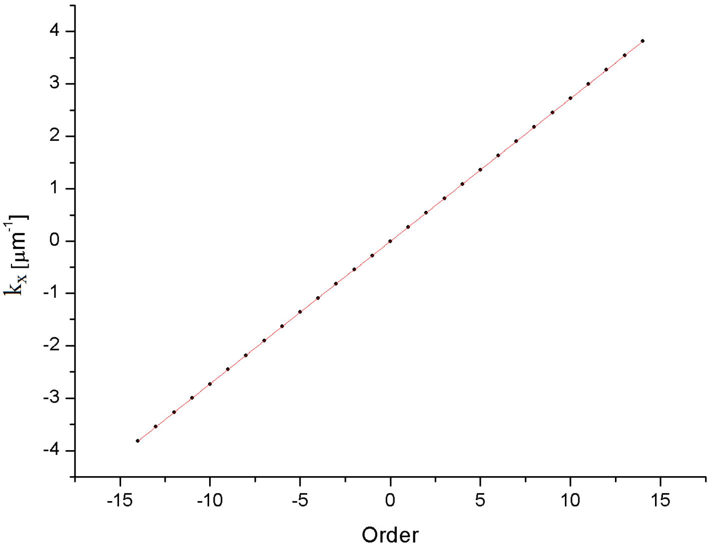

Figure 4.16: Peaks position in the reciprocal space in function of the order. The slop of the linear fit permits the estimation of the real grating period.

From the analysis of peaks intensity, information on the index profile created by the photoinduced direct writing are deduced.

From standard diffraction theory, in the thin grating approximation, the diffraction pattern can be expressed with a function of this kind:

$$I(q) = \sum_{n=-\infty}^{+\infty} |F(q)|^2 \delta(q - nQ) \tag{4.3}$$

where $|F(q)|^2$ is the square modulus of the structure factor and $\delta(q - nQ)$ is the Kronecker delta function. In other words, the reciprocal space intensity is given by a series of evenly spaced delta – like peaks located at positions nQ, whose intensity is modulated by the function:

$$F(q) = \int_{-\frac{L}{2}}^{\frac{L}{2}} \Delta n(x)\, e^{-iqx} dx. \tag{4.4}$$

where $\Delta n(x)$ is the real-space refractive index profile of a the repeated unit (in our case a written line). As it is well known, the presence of the squared modulus prevents one from obtaining direct information on $\Delta n(x)$ by directly calculating the inverse Fourier transform of $|F(q)|^2$, because all the details on the phase of *F(q)* are missing. We used therefore two approaches. In the first case we search for a simple function in direct space for Δn, so that the squared modulus of its structure factor gives an analytical dependence describing with reasonable approximation the reciprocal space intensity of each diffraction peak. The calculated structure factor is then adjusted to the experimental data in order to obtain an approximate estimate of the shape of $\Delta n(x)$. In the second approach, the actual shape of $\Delta n(x)$ is disregarded and the structure factor in reciprocal space is simply described using some phenomenological function. The idea is that as the real space shape of the line is the same for all the produced grating, we expect the structure factor to be the same for all. The periodic grating is then used to estimate this function and subsequently used to simulate the other more complex structures.

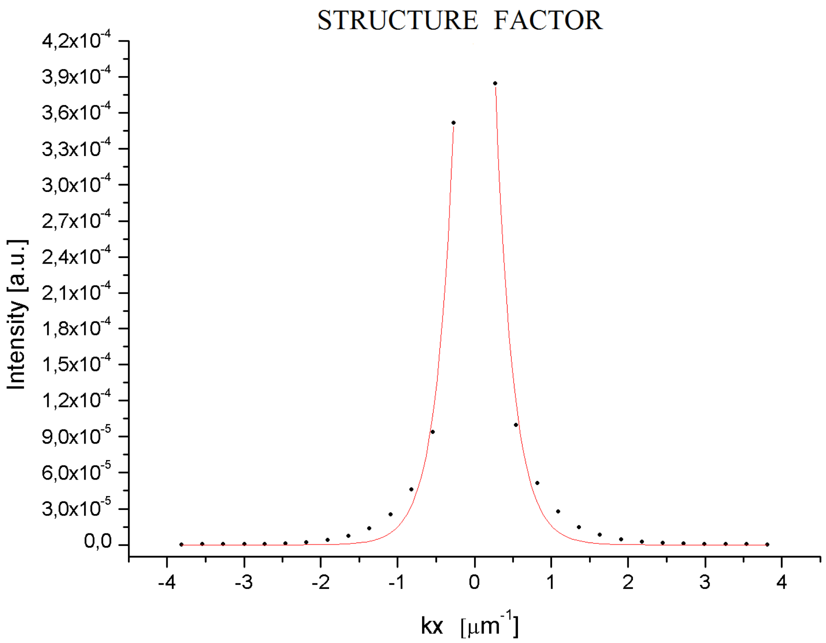

Figure 4.17: Peak intensity in function of its position in the reciprocal space. The fit of the exponential data.

Following the first approach, it can be seen that the q – behavior of the peak intensities more or less obeys an exponential dependence:

$$|F(q)|^2 \cong Ae^{-q/t} \tag{4.5}$$

The separate fit of the positive and negative k_x gives the following parameters:

	Negative k_x	Positive k_x
A [a.u.]	0.00114 ± 0.00009	0.0013 ± 0.0001
t [μm^{-1}]	-0.23 ± 0.01	0.23 ± 0.01

Table 4.4

An analytical function whose squared Fourier transform gives an exponential like (4.6) is a Lorentzian function, L(x):

$$L(x) = B\frac{\frac{\Gamma}{2\pi}}{x^2+\left(\frac{\Gamma}{2}\right)^2} \tag{4.6}$$

Where B = A^2 and $2\Gamma\pi = 1/t$, separately for positive and negative k_x. Using mean value of the Table 4.4,

A = (0.00122 ± 0.00007) a.u.
t = (0.230 ± 0.007) μm^{-1}

the Lorenztian L(x) is characterized by the parameters:

B = (0.0349285 ± 0.0000002) a.u.
Γ = (0.69 ± 0.01) μm

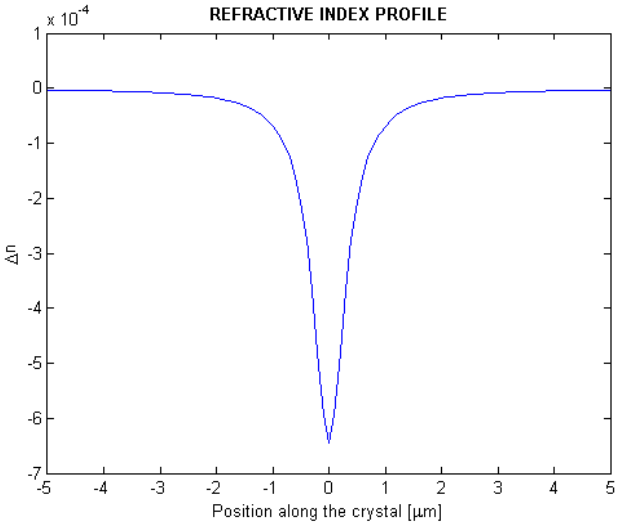

Figure 4.19: Index refraction profile obtained in bulk Fe:LN using the direct writing technique, for a laser power of 17mW and a velocity writing of 500µm/s.

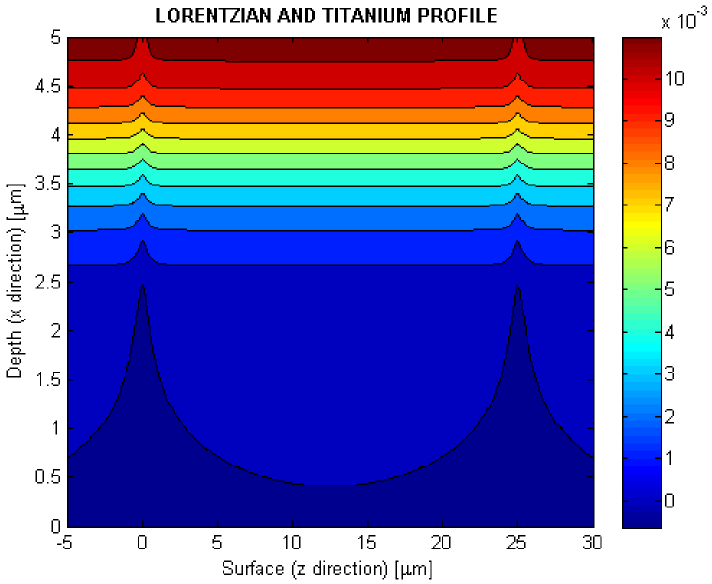

Figure 4.18: Simulation of the global variation of the refractive index due to the presence of the titanium diffused in the surface and the photoinduced direct writing technique.

According to this view, we may estimate that the refractive index profile of a single line written with an incident power of 17mW and a writing velocity of 500µm/s, has a Lorentzian shape, with the above listed parameters. A plot of the line is shown in Figure 4.18.

From this profile also information on width optical barriers created in the sample 151.15.2 can be extracted. The width at half height Γ equal to 0.69µm, is in agreement with the experimental observation that two lines written at a separation smaller than 1 µm merge together

On the contrary the amplitude B is not an indication of the maximum refractive index obtainable, because of the equation (4.5) where the peak intensity is only proportional to square module of the Fourier transformation. At this stage of setup characterization it is only known from the

literature, as seen in paragraph 2.4.1, that the variation is in the order of 10^{-4}. To have the real value two solutions are possible: to solve numerically the non linear problem for a focalized laser beam scanning the surface of the sample, or to add in the setup a Mach Zehnder interferometer to measure it directly, as made for photoinduced waveguides in SBN.
In Figure 4.19 the Lorentzian profile of Figure 4.18 due to the photoinduced direct writing process is superimposed to the refractive index profile of Figure 2.7b generated by the presence of the titanium. The waveguide E3 is simulated, characterized by a width of 25μ and single optical barriers.

For what concerns the second approach, it can be seen that the function:

$$|F(q)|^2 \cong A_1 e^{\frac{-(x-x_0)}{t_1}} + A_2 e^{\frac{-(x-x_0)}{t_2}} \qquad (4.7)$$

can be used to describe accurately the q – dependence of Figure 4.17 of the peak intensities in reciprocal space. This function will be exploited to simulate the experimental data obtained in aperiodic gratings, as explained in the following.

The aperiodic grating (A and B) are studied with the same setup of the periodic one, i.e.in far-field. The aim of their characterization is to understand if these gratings arranged in Fibonacci sequence exhibits the expected characteristics.

The two periods L and S are arranged following the substitution rule explained in paragraph 1.1.2 but it was decided to utse a total number of 300 periods.
The resulting diffraction pattern is reported in Figure 4.20 and Figure 4.21, where it can be seen as the peaks numbers is much larger than the periodic one: this is the peculiarity of these types of gratings which are dense, i.e. theoretically between two peaks it is always possible to find another one having an inferior intensity.

In order to analyse our results, we follow the Levine and Steinhardt formalism [49] according to which in the real space, 1D quasicrystals may be described by the general form:

$$x_n = n + \alpha + \frac{1}{\tau}\left[\frac{n}{\tau} + \beta\right] \qquad (4.8)$$

where n is an integer, τ the golden ratio and α, β a generic shift of the reference system and [y] is the integer part of y. Knowing that $\sqrt{5} = \tau\left(1 + \frac{1}{\tau^2}\right)$ equation (4.8) can be rewritten as

$$x_n = \left(n(1+\tau^{-2}) + \sqrt{5}\beta\right) - \frac{1}{\tau}\left\{\frac{n(1+\tau^{-2}) + \sqrt{5}\beta}{\sqrt{5}}\right\} + \alpha - \beta\tau \qquad (4.9)$$

Where {y} indicates the fractional part of y. The first term is invariant under transformation of integer multiples of $(1 + \tau^{-2})$ while the second one is always periodic with period $\tau(1 + \tau^{-2})$.
Equation (4.9) can be rewritten as:

$$x_n = (na + \phi) + F(na + \phi) \qquad (4.10)$$

where the first parenthesis indicates a quantity periodic of period *a* and F is a periodic function with period b such that b/a is an irrational number.

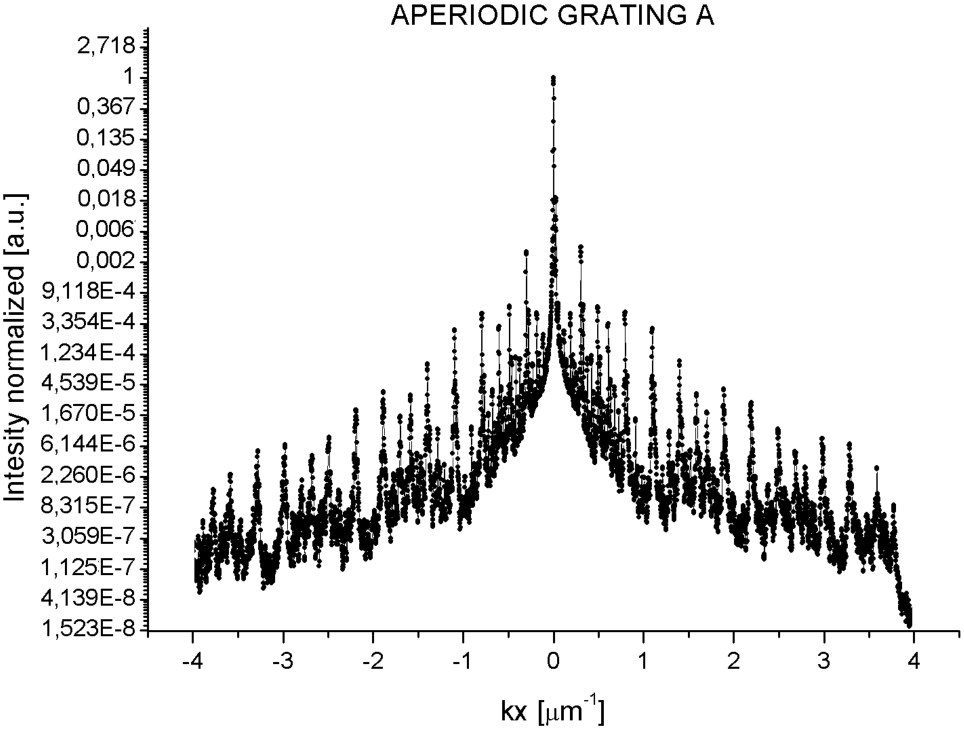

Figure 4.20: Diffraction pattern of the Fibonacci grating A. The intensity is reported in logarithmic scale.

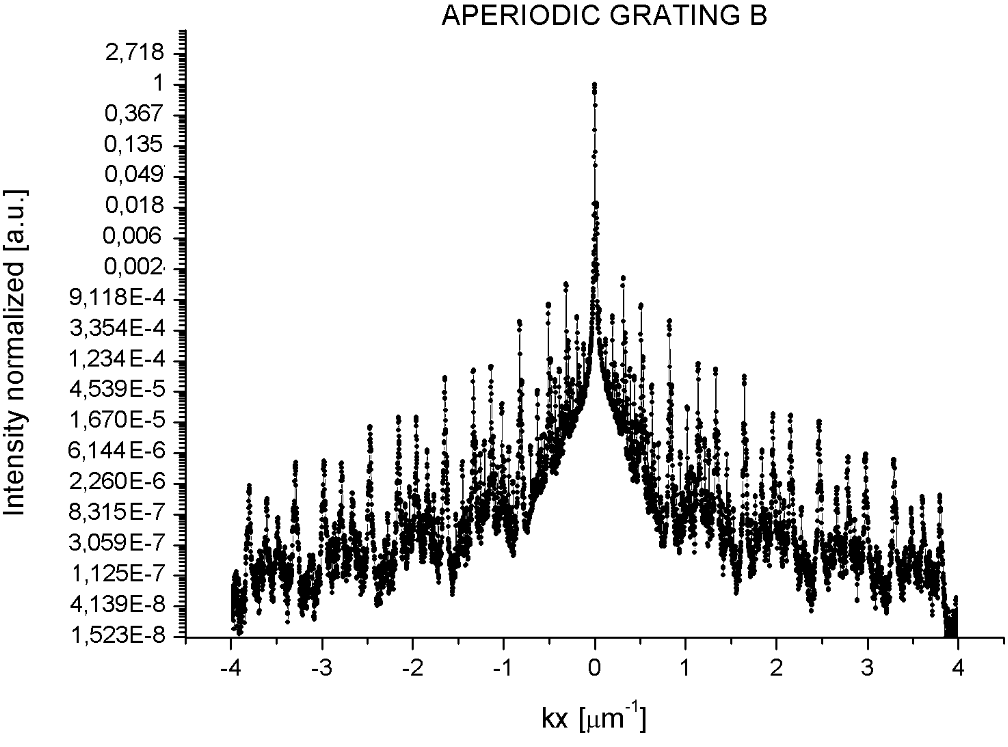

Figure 4.21: Diffraction pattern of the Fibonacci grating B. The intensity is reported in logarithmic scale.

Considering the equation (4.10) the position of our lines can be formally considered as the sum of a two periodic sequence having two incommensurate periods a and b. It can be shown that in the reciprocal space the peaks positions are defined by:

$$Q_{h,h'} = 2\pi\left(\frac{h}{a} + \frac{h'}{b}\right) = \frac{2\pi\tau^2}{1+\tau^2}\left(h + \frac{h'}{\tau}\right) \tag{4.11}$$

where h and h' are two integer numbers..

Adapting this theory to ours gratings, the equation (4.8) can be re-expressed as:

$$x_n = nL_2 + \Delta L\left[\frac{n}{\tau}\right] \tag{4.12}$$

where L_2 is long period and $\Delta L = L_1 - L_2$.
Following the same procedure used for the equation (4.8) the equation (4.12) can be rewritten as:

$$x_n = n(L_2 + \Delta L\tau^{-1}) - \Delta L\left\{\frac{n(L_2+\Delta L\tau^{-1})}{\tau(L_2+\Delta L\tau^{-1})}\right\} \tag{4.13}$$

The first term is invariant under translations of $(L_2 + \Delta L\tau^{-1})$ and the second term under translations of $\tau(L_2 + \Delta L\tau^{-1})$. In this case in the reciprocal space the peaks position are given by the formula:

$$Q_{h,h'} = \frac{2\pi\tau}{L_2\tau+\Delta L}\left(h + \frac{h'}{\tau}\right) \tag{4.14}$$

This formula cannot be directly used to generate peaks position because of their dense position in the reciprocal space. The comparison between the experimental value and the simulation is easier if the diffraction pattern is analyzed by directly calculating its reciprocal space intensity distribution from the basic definition:

$$I(q) = \left|\frac{1}{N}\sum_{n=1}^{N} F(q)e^{iqx_n}\right|^2 = \frac{1}{N}|F(q)|^2\left|\sum_{n=1}^{N} e^{iqx_n}\right|^2 \tag{4.15}$$

where x_n are the position of the grating lines according to the Fibonacci sequence and F(q) is the structure factor, in principle equal to the one of the periodic gratings. For the aperiodic grating, to calculate the the reciprocal space intensity distribution, it is necessary to separate the line shape contribution due to the structure factor from the contribution generated from the Fibonacci arrangement. The square module of the structure was obtained from the fit of the peak intensities of the periodic grating (equation 4.7 and Figure 4.17). The third term of the last member of equation (4.15) is numerically calculated considering $q = Q_{h,\,h'}$ and as example the result is reported in Figure 4.22 for the grating A where the reciprocal space is limited between 0 and 1. Comparing this graph with the one of Figure 4.23 reporting the experimental value it can be seen as the dense structure is well reproduced. Only two peaks are not in according with the real values because the simulation is very sensible of the S(k) and the function adopted, in this range, not reproduce with a good approximation experimental values. The simulation is in accord also with the rest of experimental values.

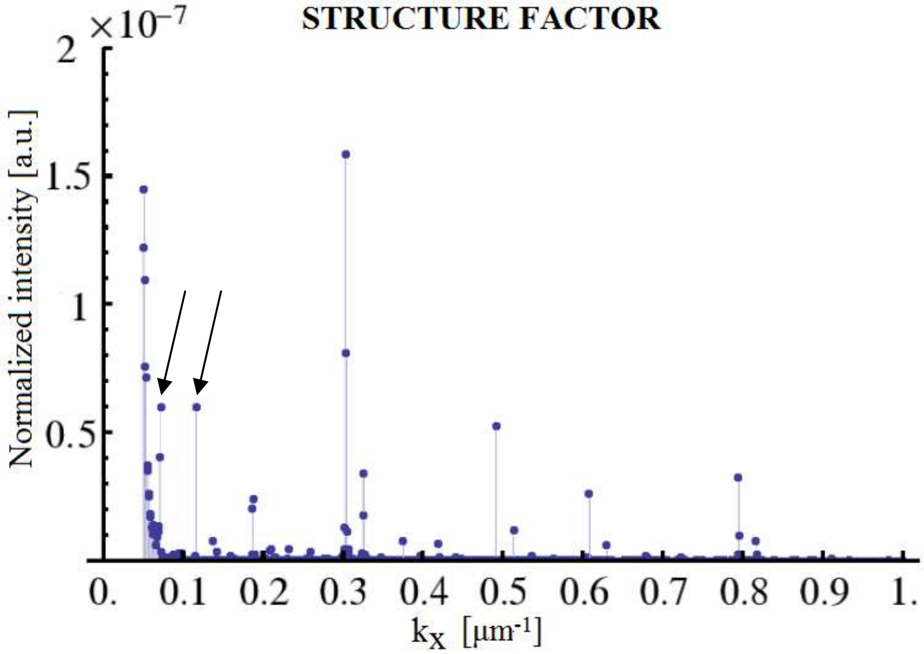

Figure 4.23: Simulation of the structure factor for the Fibonacci grating A.

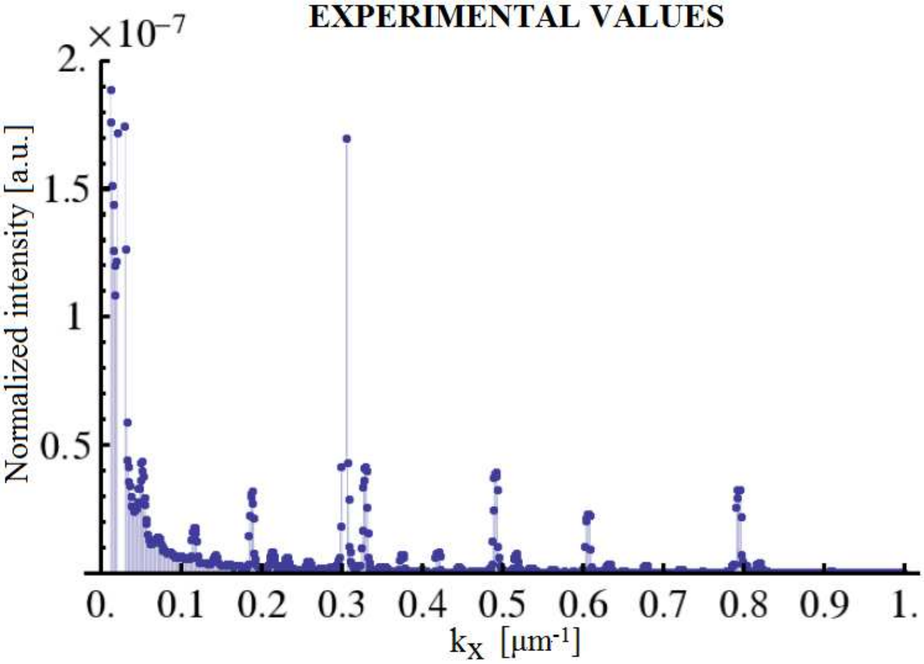

Figure 4.22: Experimenetal values of the Fibonacci grating A in the range between 0 and 1

.

CONCLUSIONS

This work was devoted to the experimental study of quantum – optical analogies by means of a new and powerful experimental approach which exploits the photorefractive effect in two different materials to produce arbitrary and reconfigurable optical structures which can be used to mimic some quantum – like phenomena.

The analogy between these two branches of physics is based on the observation that the Schrödinger equation, describing the temporal evolution in the quantum world, has the same structure of the equations resulting from the coupled mode theory. In particular they are equivalent if a correspondence between temporal and *z* coordinate is established and in this picture every quantum level become the analogue of a single optical waveguide.
Two different setups were exploited. The first one, developed by the Laboratoire Matériaux Optiques, Photoniques et Systèmes (LMOPS) at the Lorraine University, Supélelc campus in Metz (France) based on the lateral illumination technique on Ce-doped SBN samples, the other one, realized *ex novo* at the Padova University exploiting an original "direct laser writing" approach on iron – doped lithium niobate. These two systems proved to be complementary as the first allows for the production of arbitrary dynamical structures, while the second is an excellent way to produce at low cost semi – permanent optical structures and enabled us to successfully prove the optical analogue of two effects. The advantage of this approach is that the proposed methods are extremely versatile and have low cost, so are particularly suited for rapid prototyping of he complex optical structures needed in this work.

The first quantum effect reproduced is the two-state STImulated Raman Adiabatic Passage (STIRAP) which allows achieving a coherent superposition of two quantum states with equal probability in a two – level system, i.e. if initially the population is entirely confined in the ground state at the end of the process an equal distribution of the atoms in the two states is achieved. Form the quantum point of view this effect is produced modulating conveniently the laser Rabi frequency coupling the two energy levels and the detuning between the laser and the Bohr frequency. Optically this is traduced modulating in the same way the coupling constant between the two waveguides and the refractive index along the propagation direction. It is worth highlighting that this effect from the quantum point of view has been only theoretically predicted but not tested experimentally because it is difficult to find a quantum system with the desired characteristics.
Experimentally these structures were reproduced using the lateral illumination technique in a SBN crystal. The configuration giving the better results exploits a gaussian variation of pulses centered in z_1 = 7,6mm and z_2 = 15,2mm along the crystal length, having a width of half width of 6.2mm and the maximal value of the phase mismatch equal to 1.0mm^{-1} and for C to 0.42mm^{-1} .

This was reproduced creating in SBN two waveguides, one straight and having a constant refractive index and the other one curved so that the inter-guide distance is modulated with a Gaussian profile and with an additional Gaussian – like modulation of the refractive index. The experimental configuration was created starting from the pulses shape and resolving the coupled mode theory using Matlab language. A numerical resolution of the related equations was implemented, in order to allow for a precise design of the needed structures. With this configuration, the optical analogy of the two – state STIRAP was successfully observed, to our knowledge for the first time. It is worth pointing out that this effect has also some interesting practical application because a structure similar to the one here observed can be exploited as an achromatic directional coupler, of great interest for all optical signal processing. Future work will be needed to increase the stability of the observed structures which, due to their dynamical nature, may not allow for the observation of the phenomenon for a long time.

The second part of the work is devoted to the development of a new method to realize semi-permanent arbitrary three – dimensional optical structures, using the photorefractive properties of Fe – doped lithium niobate. The developed method involves the writing of optical structures using a low – power focused laser beam scanned on the sample with the aid of a computer – controlled translation stage. In this approach optical barriers can be written either in the bulk or on the top of a Ti - diffused waveguide on a Fe: LN sample. This method may seem similar to the other well-known direct writing approaches such as femtosecond laser writing, however it bears the following important differences: (i) the laser source can be a low- cost CW green laser with moderate power of the order of 10 mW. (ii) The realized structures can be easily erased by illumination with a inhomogeneous light. (iii) The obtained refractive index variations are negative instead than positive. The realized setup was tested, defining the optimal process parameters, which enabled to obtain stable refractive index modulations were obtained. In particular the possibility of confining light into waveguides obtained by creating two optical barriers at close distance was demonstrated, to our knowledge for the first time.

Also this method can be used to test some quantum processes, similar to the ones highlighted above, or to test the optical analogue of some solid state systems difficult to obtain experimentally. In this thesis, to demonstrate the usefulness of this approach, we studied the diffraction characteristics of an optical quasi – crystal, which will be used in the continuation of this work to study the propagation of light in an array of aperiodically coupled waveguides. Quasi crystals can be considered as an intermediate phase between an ordered and a disordered structure which does not exhibits translational invariance but anyway possessing a long range order and displaying some peculiar aspects in diffraction experiments. To this purposes we exploited the advantages of our setup to record a series of quasi – periodic lattices by writing a sequence of lines arranged according to a Fibonacci sequence. The reciprocal lattice of the produced structures was studied by optical diffraction. By comparison with a periodic grating recorded in the same conditions, we were able to obtain information on the refractive index profile of a single line and we highlighted how the presence of quasi – periodic order modifies the diffraction characteristics of the sample. An analysis performed using quasi – crystal theory, shows that the diffraction pattern is in good agreement with theoretical predictions.

ANNEX A

In this section programs written using Matlab language are reported. They are used to create all simulations and images reported in the chapter 3, and they were the base to the experimental study of the optical two-state STIRAP.

PROGRAM 1

```
Clear all

%% Guides parameters
step=0.001;                 %step of calculation
length=23;                  %mm
nrguide=2;                  %number of the guides
nrzpoints=0:step:length; %number of the points along the crystal

%% Pulses parameters
kconstant=0.37; %coupling constant max (mm-1)
delta_beta=1.0; %delta_beta max (mm-1)

%gaussian variation of the coupling constant and the phase mismatch
kconstant1(1,:)=kconstant*exp(-((nrzpoints-13.8)/(5)).^2);
delta_beta1(1,:)=delta_beta*exp(-((nrzpoints-9)/(5)).^2);

%% Initial conditions
%definition of the matrix of electric field
Es=zeros(nrguide,size(nrzpoints,2));
%the electric field is coupled entirely in one of the two guides
Es(1,1)=1;

%% Resolution of coupling equation using Euler's method
for j=2:size(nrzpoints,2)
    Es(1,j)=Es(1,j-1)-i*step*(kconstant1(j)*(Es(2,j-1))+ delta_beta1(j)*
Es(1,j-1));
    Es(2,j)=Es(2,j-1)-i*step*(kconstant1(j)*(Es(1,j-1)));

    Intensityout=abs(Es).^2; %calculation of the intensity

end
figure;
plot(nrzpoints,Intensityout);
xlabel('Distance along the crystal [mm]');
ylabel('Normalized Intensity [a.u]');
title('INTENSITY PROFILE','FontWeight','bold','FontSize',9);
axis([0 23 0 1.1]);
box off;
figure;
plot(nrzpoints,delta_beta1,nrzpoints,kconstant1);
title ('GAUSSIANS PULSES','FontWeight','bold','FontSize',9);
```

```
xlabel('Distance along the crystal [mm]');
ylabel('Pulses [mm^{-1}]');

%the writing is controlled by the mouse in the graphic
gtext('\Delta\beta');
gtext ('C');
axis([0 23 0 1.1]);
box off;
```

PROGRAM 2

```
clear all

lambda=633e-3;       %wavelength (μm)
length_crystal=23;   %mm
Z0=376.730;          %characteristic impedance of empty

%% Pulses Parameters
%the crystal is subdivided in steps of 0.05 mm
nrzpoints=1:0.05:length_crystal;
C=0.3;    %coupling constant max(mm-1)
B=1.0;    %delta_beta max (mm-1)
%gaussian variation of the coupling constant and the phase mismatch
kconstant=C*exp(-((nrzpoints-7.6)/(7)).^2);
delta_beta=B*exp(-((nrzpoints-15.2)/(7)).^2);

%% Waveguides Parameters
d=7.2;         %waveguide width μm (6 pixel)
s=1:0.05:30;   %waveguide separation (μm)
ne=2.2953;     %bulk refraction index

%guide with fixe refraction index
frangie_a=4.7;    %it corresponds to a gray level of 75%
%experimental refraction index
dn_a_efficace=lambda*frangie_a/(length_crystal*10^3):
%theoretic refraction index extract from Program 3
dn_a=-1.2e19*dn_a_efficace^6+9.9e15*dn_a_efficace^5-3.3e12*
      dn_a_efficace^4+5.5e8*dn_a_efficace^3-5e4*dn_a_efficace^2
      +3.8*dn_a_efficace+1.3e-5;

%guide with varying refraction index
%experimental refraction index
dn_b_efficace(1,:)=(lambda*10^(-3)*delta_beta)/(2*pi)+dn_a_efficace;
%theoretic refraction index extract from Program 3
dn_b(1,:)=-1.2e19*dn_b_efficace.^6+9.9e15*dn_b_efficace.^5-
3.3e12*dn_b_efficace.^4+5.5e8*dn_b_efficace.^3-
5e4*dn_b_efficace.^2+3.8*dn_b_efficace+1.3e-5;

%% Transcendental equation of guide with fixe refraction index
k0=2*pi/lambda;
%limit value of sin_theta for the first mode
lim_a=lambda/(2*d*(ne+dn_a))-1e-12;
%complementary of the critical angle
theta_c_a=acos(ne/(ne+dn_a));
sin_theta_a=0.000001:0.000001:lim_a;
for g=1:length(sin_theta_a)
  %left side of trscendental equation,m=0
  left_a(g)=tan(pi*d*(ne+dn_a)*sin_theta_a(g)/lambda);
```

```
  %right side of trscendental equation
  right_a(g)=sqrt((sin(theta_c_a))^2/(sin_theta_a(g)*sin_theta_a(g))-1);
    result_a(g)=right_a(g)-left_a(g);
end
%it find the minimum value and it stokes in i_a the corresponding index
of array
[minimum_a,i_a]=min(abs(result_a));
%it is the value where the two curves cross each other
sin_theta_m_a=sin_theta_a(i_a);
theta_m_a=asin(sin_theta_m_a);           %mode angle for waveguide a
%Longitudinal constant of propagation for waveguide a
beta_m_a=k0*(ne+dn_a)*cos(theta_m_a);

%% Calculation of mode's constants
h_a=sqrt(k0^2*(ne+dn_a)^2-beta_m_a^2);
%Tranverse propagation constant for waveguide a
gamma_m_a=ne*k0*sqrt((cos(theta_m_a))^2/(cos(theta_c_a))^2-1);
%Extinction coefficient for waveguide a
b_a=(cos(2*(ne+dn_a)*pi*sin_theta_m_a/lambda*d/2))/(exp(-
gamma_m_a*d/2));  %proportionality factor

%% Transcendental equation of guide with varying refraction index
for k=1:length(dn_b)
    theta_c_b(k)=acos(ne/(ne+dn_b(k)));
    sin_theta_c_b(k)=sin(theta_c_b(k));
    lim_b(k)=lambda/(2*d*(ne+dn_b(k)))-1e-12;
    if lim_b<sin_theta_c_b
        sin_theta_b=0.000001:0.000001:lim_b(k);
        for g=1:length(sin_theta_b)
            left_b(g)=tan(pi*d*(ne+dn_b(k))*sin_theta_b(g)/lambda);
right_b(g)=sqrt((sin(theta_c_b(k)))^2/(sin_theta_b(g)*sin_theta_b(g))-
1);
            result_b(g)=right_b(g)-left_b(g);
        end
    else
      sin_theta_b=0.000001:0.000001:sin_theta_c_b(k);
        for g=1:length(sin_theta_b)
            left_b(g)=tan(pi*d*(ne+dn_b(k))*sin_theta_b(g)/lambda);

right_b(g)=sqrt((sin(theta_c_b(k)))^2/(sin_theta_b(g)*sin_theta_b(g))-
1);
            result_b(g)=right_b(g)-left_b(g);
        end
    end
    [minimum_b,i_b]=min(abs(result_b));
    sin_theta_m_b(k)=sin_theta_b(i_b);
    theta_m_b(k)=asin(sin_theta_m_b(k));
    beta_m_b(k)=k0*(ne+dn_b(k))*cos(theta_m_b(k));

%% Calculation of mode's constants
%Transverse propagation constant for waveguide b
h_b(k)=sqrt(k0^2*(ne+dn_b(k))^2-beta_m_b(k)^2);
%Extinction coefficient for waveguide b
gamma_m_b(k)=(ne)*k0*sqrt((cos(theta_m_b(k)))^2/(cos(theta_c_b(k)))^2-
1);
%proportionality factor
b_b(k)=(cos(2*(ne+dn_b(k))*pi*sin_theta_m_b(k)/lambda*d/2))/(exp(-
gamma_m_b(k)*d/2));
```

```
%% Calculation of the mode um_a and um_b
      for t=1:length(s)
      l_suppl=20; %µm,
      ymin=-l_suppl-d/2;       %inferior extreme of the array
      ymax=d/2+s(t)+d+l_suppl; %superior extreme of the array
      pas=0.01;
%the zero of the coordinate is centered in the inferior guide
      ya=ymin:pas:ymax;
%the zero of the coordinate is centered in the superior guide
      yb=fliplr(ya);

%filling of an array with the refractive index na in the inferior guide
and with bulk index outside
      na=zeros(length(ya),1);
      indice_debut_guide=round(l_suppl/pas);
      indice_fin_guide=indice_debut_guide+round(d/pas);
      na(indice_debut_guide+1:indice_fin_guide+1)=ne+dn_a;
      na(1:indice_debut_guide)=ne;
      na(indice_fin_guide+2:end)=ne;

      um_a=zeros(length(ya),1);
      um_a(indice_debut_guide+1:indice_fin_guide+1)=cos(h_a*ya(indice_de
but_guide+1:indice_fin_guide+1));
      um_a(1:indice_debut_guide)=b_a*exp(gamma_m_a*ya(1:indice_debut_gui
de));
      um_a(indice_fin_guide+2:end)=b_a*exp(-
      gamma_m_a*ya(indice_fin_guide+2:end));

      um_I_a=um_a.^2;

%filling of an array with the refractive index nb in the superior guide
and with bulk index outside
      nb=zeros(length(yb),1);
      indice_debut_guide=round((l_suppl+d+s(t))/pas);
      indice_fin_guide=indice_debut_guide+round(d/pas);
      nb(indice_debut_guide+1:indice_fin_guide+1)=ne+dn_b(k);
      nb(1:indice_debut_guide)=ne;
      nb(indice_fin_guide+2:end)=ne;

      um_b=zeros(length(yb),1);
      um_b(indice_debut_guide+1:indice_fin_guide+1)=cos(h_b(k)*yb(indice
_debut_guide+1:indice_fin_guide+1));
      um_b(1:indice_debut_guide)=b_b(k)*exp(-
      gamma_m_b(k)*yb(1:indice_debut_guide));
      um_b(indice_fin_guide+2:end)=b_b(k)*exp(gamma_m_b(k)*yb(indice_fin
_guide+2:end));

      um_I_b=um_b.^2;

%Normalization
%the integral is calculated using the trapezoidal method
      norm_um_b=-beta_m_b(k)/(2*k0*Z0)*trapz(yb,um_I_b(:));
      norm_um_a=beta_m_a/(2*k0*Z0)*trapz(ya,um_I_a(:));

      UM_a=1/sqrt(norm_um_a)*um_a;
      UM_b=1/sqrt(norm_um_b)*um_b;

      UM_ab=UM_a.*UM_b;
      integrando_a=(na.^2-ne^2).*UM_ab;
```

```
      kappa_ab=trapz(ya,integrando_a);   %µm^-1
        kappa1(t)=k0/(4*Z0)*kappa_ab;      %coupling constant a-b

        integrando_b=(nb.^2-ne^2).*UM_ab;
        kappa_ba=-trapz(yb,integrando_b);  %µm^-1
        kappa2(t)=k0/(4*Z0)*kappa_ba;      %coupling constant b-a

   %effective coupling constant
        kappa_eff(t)=sqrt(kappa1(t).*kappa2(t)); %µm^-1
%the difference between the gaussian coupling constant and the
calculated coupling constant is computed
        difference(t)=kconstant(k)-10^3*kappa_eff(t);
end
%finding of the minimum value of the array 'difference' and stoking in z
the corresponding index
    [minimo,z]=min(abs(difference));
%distance board to board of the two waveguides that reproduces the best
value of gaussian coupling constant
    Sp(k)=s(z);   %µm
end

figure;
plot(Sp);
title('Profile of the guide curvature','FontWeight','bold',
'FontSize',9);
xlabel('Distance along the crystal [mm]');
ylabel('Distance board to board of the two waveguides [µm]');
```

PROGRAM 3

```
clear all

%% Guides parameters
ne=2.2953;            %bulk refraction index
d=7.2;                %waveguide width µm (6 pixel)
lamb=633e-3;          %wavelength (µm)
dn=1e-5:1e-5:4e-4;    %variation of the refraction index

%% Transcendental equation
 k0=2*pi/lamb;
% limit value for sin_theta for the first mode
for k=1:length(dn)
    lim(k)=lamb/(2*d*(ne+dn(k)))-1e-12;
end
for k=1:length(dn)
    theta_c(k)=acos(ne/(ne+dn(k))); %complementary of the critical angle
    sin_theta=0.000001:0.000001:lim(k);
    left=tan(pi*d*(ne+dn(k))/lamb*sin_theta); %left side of the equation
    right=sqrt(sin(theta_c(k))^2./(sin_theta.*sin_theta)-1);%right side
    result=right-left;
    [minimum,i]=min(abs(result))

%% %% Calculation of mode's constants
    sin_theta_m(k)=sin_theta(i);
    theta_m(k)=asin(sin_theta_m(k));            %mode angle
    beta_m(k)=k0*(ne+dn(k))*cos(theta_m(k));    %longitudinal constant
```

```
    delta_n_eff(k)=(beta_m(k)-k0*ne)/k0;

end

figure;
plot(delta_n_eff,dn);
ylabel('\Deltan_{theo}');
xlabel('\Deltan_{effective}');
title('THEORETICAL INDEX REFRACTION','FontWeight','bold');
```

PROGRAM 4

```
figure;
%to set the dimensions of the image. with the resolution of 1200dpi the
finals dimendions are (6.394*1200, 3.9985*1200)pixel = (4800,7680)pixel
%it is decided to utilised an initial image with dimensions 4 times that
the originals (=1200,1920)pixel
set(gcf,'PaperUnits','inches','Paperposition', [0 0 6.394 3.9985]);

%to convert µm to pixel, to move the courved guide to take into account
the  thickness of the two guides,to reflect the image because the light
is injected from right
conversion=zeros;
for i=1:length(Sp)
    conversion(length(delta_beta)+1-i)=Sp(i)/(1.2)+6;
end

gray=zeros(length(delta_beta),1);
delta_beta_conversion=zeros(length(delta_beta),1);

%plot of the courved guide from right to left with gaussian refraction
index
for i=1:length(delta_beta)
%to set the other guide the zero of the variation of the refraction
index and to transform from mm^-1 to cm^-1
    delta_beta_conversion(length(delta_beta)+1-i)=12.839-
(delta_beta(i)*10);
    gray(length(delta_beta)+1-i)=(-
0.0052*(delta_beta_conversion(length(delta_beta)+1-
i))^3+0.16*(delta_beta_conversion(length(delta_beta)+1-
i))^2+0.99*delta_beta_conversion(length(delta_beta)+1-i)+47)/100;
    hold on;
plot(i,conversion(i),'s','MarkerEdgeColor',[gray(length(delta_beta)+1-
i),gray(length(delta_beta)+1-i),gray(length(delta_beta)+1-i)],
'MarkerFaceColor',[gray(length(delta_beta)+1-
i),gray(length(delta_beta)+1-i),gray(length(delta_beta)+1-
i)],'MarkerSize',1.2);
end

%to set the background of the image with the color noir
set(gcf,'color',[0 0 0]);
%horizontally in the left the 6% of the image is noir, vertically the
straight guide is centre in the middle of the image
axis([-(length(delta_beta)*0.06) length(delta_beta) -600 600]);
%to eliminate the image's white bord
set(gca, 'Units', 'normalized', 'Position', [0 0 1 1] );
axis off;
%to save the image with the right colors previously decided
```

```
set(gcf, 'InvertHardCopy', 'off');
%to save the image with a resolution of 1200dpi
print -dpng prova1.png -r1200;
I=imread('prova1.png');
%to create the final image with the right dimensions (1200pixel x
1920pixel)
A = imresize(I,[1200 1920],'bicubic');
imwrite (A,'int_grigi_guida_curva1.png'); %to save the curved guide

figure;
set(gcf,'PaperUnits','inches','Paperposition', [0 0 6.394 3.9985]);

%plot of the straight guide with fixe refraction index
y=0;
for i=1:length(delta_beta)
    hold on;
    plot(i,y,'s','MarkerEdgeColor',[0.75 0.75 0.75],
'MarkerFaceColor',[0.75 0.75 0.75],'MarkerSize',1.2);
end

set(gcf,'color',[0 0 0]);
axis([-(length(delta_beta)*0.06) length(delta_beta) -600 600]);
set(gca, 'Units', 'normalized', 'Position', [0 0 1 1] );
axis off;
set(gcf, 'InvertHardCopy', 'off');
print -dpng prova2.png -r1200;
J=imread('prova2.png');
B = imresize(J,[1200 1920],'bicubic');
imwrite(B,'int_grigi_guida_curva2.png');

C=imadd(A,B);       %superposition of the two images
imwrite(C,'int(15,2-1,0)(7,6-0,3)7_grigi_guida_curva_negativo.png');
```

BIBLIOGRAPHY

[1] S. Longhi. *Quantum-optical analogies using photonic structures*. Laser & Photon. Rev. 3, No. 3,243-261(2009).

[2] V. S. Malinovsky and D. J. Tannor. *Simple and robust extension of the stimulated raman adiabatic passage technique to n-level systems.* Phys. Rev. A, 56, 4929-4937, 1997.

[3] S. E. Harris, J. E. Field, and A. Imamoglu. *Nonlinear optical processes using electromagnetically induced transparency*. Phys. Rev. Lett., 64, 1107-1110, 1990.

[4] S. E. Harris. *Electromagnetically induced transparency*. Physics Today, 50, 36-42, 1997.

[5] K. J. Boller, A. Imamoglu, and S. E. Harris. *Observation of electromagnetically induced transparency.* Phys. Rev. Lett., 66, 2593-2596, 1991.

[6] J. E. Field, K. H. Hahn, and S. E. Harris. *Observation of electromagnetically induced transparency in collisionasly broadened lead vapor.* Phys. Rev. Lett., 67, 3062-3065, 1991.

[7] N.V.Vitanov, M. Fleischhauer, B.W Shore, K. Bergamann. *Coherent manipulation of atoms and molecules by sequential laser pulse.* Advances in atomin, molecular, and optical physics, Vol. 46.

[8] C. Ciret. *Structures des guides d’onde photo-induits et analogies quantiques*. PhD thesis, Université de Lorraine.

[9] C. Ciret, V. Coda, A.A. Rangelov, D.N. Neshev, and G. Montemezzani. *Planar achromatic multiple Beam splitter by adiabatic light transfer.* Optics Letters, Vol. 38, No.18 (2012).

[10] C. Ciret, V. Coda, A.A. Rangelov, D.N. Neshev, and G. Montemezzani. *Broadband adiabaticlight transfer in optically inducedwavwguides arrays.* Physical Review A 87, 013806 (2013).

[11] C. Ciret, M. Alonzo, V. Coda, A.A. Rangelov, and G. Montemezzani. *Analogue to electromagnetically induced transparency and Autler-Towns effect demonstrated with photo induced coupled waveguides.* Physical Review A 88, 013840 (2013).

[12] N.V.Vitanov, B.W Shore. *Stimulated Raman adiabatic passage in a two-state system.* Physical Review A 73, 053402 (2006).

[13] A. Yariv. *Coupled mode theory for guided-wave optics.* IEE J. Quant. Electron., QE-9, 919 933, 1973.

[14] M. D. Ewbank, R. R. Neurgaonkar, W. K. Cory, and J. Feinberg. *Photorefractive properties of strontium-barium niobate.* J. Appl. Phys., 63, 374-380, 1987.

[15] T. R. Volk, N. R. Ivanov, D. V. Isakov, L. I. Ivleva, and P. A. Lykov. *Electro-optical properties of strontium-barium niobate crystals and their relation to the domain structure of the crystals.* Phys. Solid State, 47, 305-311, 2005.

[16] O. Kwon, O. Eknoyan, H. F. Taylor, and R. R. Neurgaonkar. *Low-voltage electro-optic modulator in SBN:60.* Electron. Lett., 35, 219-220, 1999.

[17] H. Y. Zhang, X. H. He, Y. H. Shih, and L. Yan. *Picosecond phase conjugation and two wave coupling in strontium barium niobate.* J. Mod. Opt., 41, 669-674, 1994.

[18] J. B. Thaxter. Electrical control of holographic storage in strontium-barium niobate. Appl. Phys. Lett., 15, 210-212, 1969.

[19] M. Segev, B. Crosignani, A. Yariv, and B. Fischer. *Spatial solitons in photorefractive media.* Phys. Rev. Lett., 68, 923-926, 1992.

[20] M. Wesner, C, Herden, D. Kip, E. Kratzig , and P. Moretti. *Photorefractive steady state soliton up to telecommunication wavelengths in planar SBN waveguides.* Opt. Commun., 188, 69-76, 2001

[21] A. S. Kewitsch, M. Segev, A. Yariv, G. J. Salamo, T. W. Towe, E. J. Sharp and R. R. Neurgaonkar. *Tunable quasi-phase matching using dynamic ferroelectric domain gratings induced by photorefractive space-charge fields.* Appl. Phys., Lett., 64, 3068-3070, 1994.

[22] H. S. Lee, J. P. Wild, and R. S. Feigelson. *Bridgman growth of strontium barium niobate single crystals.* J. Crystal Growth, 187, 89-101, 1998.

[23] L.I. Ivleva, N. V. Bogodaev, N. M. Polozkov, ans V. V. Osiko. *Growth of SBN signle crystals by stepanov technique for photorefractive applications.* Opt., Mater., 4, 168-173, 1995.

[24] L.I. Ivleva, T. R. Volk, D. V. Isakov, V. V. Gladkii, N. M. Polozkov, and P. A. Lykov. *Growth and ferroelectric properties of Nd-doped strontium baruim niobate crystals.* J. Crystal Growth, 237-239, Part 1, 700-702, 2002.

[25] M. Ulex, R. Pankrath, and K. Betzler *Growth of strontium barium niobate: the liquidus solidus phase diagram.* J. Crystal Growth, 271, 128-133, 2004.

[26] K. Megumi, H. Kozuka, M. Kobayashi, and Y. Furuhata. *High sensitive holographic storage in Ce-doped SBN.* Appl. Phys., Lett., 30, 631-633, 1977.

[27] M. Gorram. *Generation et etude de guides d'onde dynamiques et reconfigurables induit par illumination lateral.* PhD thesis, Université de Metz, 2009.

[28] A. Ashkin, G. D. Boyd, J. M. Dziedzic, R. G. Smith, A. A. Ballman, J. J. Levinstein, and K. Nassau. *Optically-induced refractive index inhomogeneities in* $LiNbO_3$ *and* $LiTaO_3$. Appl. Phys. Lett., 13,223-225, 1968.

[29] F. s. Chen. *Optically induced change of refractive indices in* $LiNbO_3$ *and* $LiTaO_3$. J. Appl. Phys., 40, 3389-3396, 1969.

[30] N. V. Kukhtarev, V. B. Markov, S. G. Odulov, M. S. Soskin, and L. Vinetskii. *Holographic storage in electrooptic crystals. i. steady state.* Ferroelectrics, 22, 949-960, 1978.

[31] N. V. Kukhtarev, V. B. Markov, S. G. Odulov, M. S. Soskin, and L. Vinetskii. *Holographic storage in electrooptic crystals. ii. Beam coupling and light amplification.* Ferroelectrics, 22, 961-964, 1978.

[32] R. Ryf, M. Wiki, G. Montemezzani, P. Gunter, and A. A. Zozulya. *Launching one transverse-dimensional photorefractive solitons in $KNbO_3$ crystals.* Opt. Commun., 159, 339-348, 1999.

[33] A. A. Zozulya and D. Z. Anderson. *Propagation of an optical beam in a photorefractive medium in the presence of a photogalvanic nonlinearity or an externally applied electric field.* Physical Rewiew A, volume 51, number 2, 1995.

[34] W. H. Zacharisen, Skr. Norske Vid.-Ada., Oslo, Mat. Naturv. No.4 (1928)

[35] A. A. Ballman. *Growth of piezoelectric and ferroelectric materials by the Czochralsky technique.* J. Am. Ceram. Soc. 48 (1965) 112.

[36] A. Räuber. Chemistry and Physics of Lithium Niobate, 1978.

[37] P.Górsky, R. Ledzion, K. Bondarczuk and W. Kucharczyk. Opto-Electronics Review 16(1), p. 46, 2008.

[38] M. Falk, J. Japs, T.Woike, K. Buse. *Charge transport in highly iron-doped oxidized lithium niobate single crystals.* Appl. Phys. B 87, 119-122 (2007).

[39] S. Bian. *Estimation of photovoltaic field in $LiNbO_3$ crystal by Z-scan.* Optics Comm. 141 (1997) 292-297.

[40] L. Levi, M. Rechtsman, B.Freedman, T. Schwartz. O. Manela, M. Segev. *Disorder Enhanced Transport in Photonic Quasicrystals.* Science 332, 1541 (2011).

[41] G. Corrielli, G. Della Valle, A. Crespi, R. Osellame, and S. Longhi. *Observation of surface states with algebric localization.* PRL 111,220403 (2013).

[42] Shechtmann, D., Blech, L. Gratias, D & Cahn, J, W. *Metallic phase with long-range orientational order and no translational symmetry.* Phys. Rev. Lett. 53, 1951-1953 (1984).

[43] Levine, D & Steinhardt, P. J. *Quasicrystals: a new class of ordered structures.* Phys. Rev Lett. 53, 2477-2480 (1984).

[44] Kohomoto, M.,Sutherland, B. & Iguchi, K. *Localization of optics: Quasiperiodic media.* Phys. Rev. Lett. 58, 2436-2438 (1987).

[45] R. Grousson, M. Henry, S. Mallick, and S. L. Xu. *Measurement of bulk photovoltaic and photorefractive characteristics of iron doped $LiNbO_3$.* J. Appl. Phys., 54(6), June 1983.

[46] K. Buse. *Lightinduced charge transport processes in photorefractive crystals II: Materials*. Appl. Phys. B 64, 391–407 (1997).

[47] A. Yariv. *Optical electronics in Modern Communications*. Oxford University Press, 1997

[48] N. Argiolas, M. Bazzan, C. Sada, P. Mazzoldi, F. M. Pigozzo, A. D. Capobianco, and E. Autizi. *Refractive index modulation in periodically poled lithium niobate crystals.* Ferroelectrics, 352:125-133, 2007.

[49] D. Levine, and P.J. Steinhardt. *Quasicrystals. I. Definition and structure*. PRB 34, 596 (1986);

[50] S. Fouchet, A. Carenco, c. Daguet, R. Guglielmi, and L. Riviere. *Wavelength Dispersion of Ti Induced Refractive Index Change in Limo3 as a Function of Diffusion Parameters.* Journal of lightwave technology, vol. Lt-5, no. 5, may 1987